

Colloidal Quantum Dots for Integrated Light Sources

Colloïdale kwantumstippen voor geïntegreerde lichtbronnen

Suzanne Bisschop

Promotoren: prof. dr. ir. Z. Hens, prof. dr. ir. D. Van Thourhout, dr. ir. E. Brainis
Proefschrift ingediend tot het behalen van de graad van
Doctor in de Ingenieurswetenschappen: Fotonica

Vakgroep Informatietechnologie
Voorzitter: prof. dr. ir. D. De Zutter
Faculteit Ingenieurswetenschappen en Architectuur

Vakgroep Anorganische en Fysische Chemie
Voorzitter: prof. dr. I. Van Driessche
Faculteit wetenschappen



Academiejaar 2017 - 2018



Universiteit Gent
Faculteit Ingenieurswetenschappen en Architectuur
Vakgroep Informatietechnologie
Faculteit Wetenschappen
Vakgroep Anorganische en Fysische Chemie

Promotoren:

prof. dr. ir. Zeger Hens
prof. dr. ir. Dries Van Thourhout
dr. ir. Edouard Brainis

Jury:

prof. dr. ir. Daniël De Zutter (chairman)	Ghent University
prof. dr. ir. Bart Kuyken	Ghent University
prof. dr. ir. Iwan Moreels	Ghent University
prof. dr. ir. Kristiaan Neyts	Ghent University
prof. dr. Krassimir Panajotov	Vrije Universiteit Brussel

Universiteit Gent
Faculteit Ingenieurswetenschappen en Architectuur
Vakgroep Informatietechnologie
Technologiepark-Zwijnaarde 15, B-9052 Gent, België
Tel.: +32-9-2643316
Fax.: +32-9-2643593

Proefschrift tot het behalen van de graad van
Doctor in de Ingenieurswetenschappen: Fotonica
Academiejaar 2017-2018

Contents

List of Acronyms	v
Nederlandse samenvatting	ix
English summary	xv
1 Introduction	1
1.1 Research background	1
1.2 Colloidal quantum dots	3
1.2.1 Wet chemical synthesis	5
1.2.2 Optoelectronic properties	6
1.2.2.1 Light absorption and emission	6
1.2.2.2 Dependence of the optical band gap	8
1.2.2.3 Maxwell Garnett effective medium approxi- mation	9
1.2.2.4 Intrinsic absorption coefficient	11
1.2.3 Transition rates: quantum picture	13
1.2.3.1 Rate of absorption and oscillator strength	14
1.2.3.2 Spontaneous emission rates and Purcell factor	14
1.2.3.3 Single-photon source	16
1.3 Integrated photonics	17
1.3.1 QD deposition techniques	17
1.3.2 Patterning of QD (mono)layers	20
1.3.3 QDs in integrated photonic devices	21
1.4 Transient absorption spectroscopy	24
1.4.1 TAS technique and setup	25
1.4.2 Ultra-fast properties	27
1.5 Thesis layout	29

1.6	Publications	30
2	Broadband enhancement of single-photon emission and polarization dependent coupling in SiN waveguides	39
2.1	Introduction	39
2.2	Classical dipole in inhomogeneous dielectric media	42
2.3	Light emission from randomly polarized dipoles	43
2.4	Results and discussion	44
2.4.1	Strip waveguides	44
2.4.2	Slot waveguides	49
2.5	Conclusion	52
3	Fabrication and characterization of SiN_x/Au cavities with colloidal QDs	59
3.1	Introduction	59
3.2	Cavity structure and fabrication	61
3.3	Simulations	66
3.3.1	Permittivity of a QD layer	66
3.3.2	Optical modes in the nanopatch cavity	68
3.3.3	Effect of random QD orientation and position	72
3.4	Measurements and results	74
3.5	Conclusion	78
4	The impact of core/shell geometry on the optical gain characteristics of CdSe/CdS QDs	83
4.1	Introduction	84
4.2	Background	86
4.2.1	Material gain	86
4.2.2	Influence of core/shell morphology	87
4.3	Experimental results	91
4.3.1	Spectroscopic characteristics	91
4.3.2	Quantitative analysis of optical gain	97
4.3.3	Model validation	101
4.4	Discussion	105
4.5	Conclusion	109

5	Colloidal QDs for integrated amplifiers and lasers	115
5.1	Introduction	115
5.2	Colloidal QDs as gain material	116
5.2.1	Spectroscopic characterisation	118
5.2.2	VSL-measurement: modal gain	120
5.3	DFB grating design and fabrication	124
5.4	Measurements and discussion	127
5.5	Conclusion	130
6	Conclusions and perspectives	135
6.1	Single-photon sources with colloidal QDs	135
6.2	Optical gain with colloidal QDs	137
A	Appendix	143
A.1	Derivation of Eq. (1.22): QED in vacuum	143
A.2	Derivation of Eqs. (3.6a) and (3.6b)	145
A.2.1	Rotation by an angle $\theta = \pi/2$ around the z -axis	146
A.2.2	Mirror symmetry through the plane (y, z)	147
A.2.3	Discussion	148
A.2.4	\mathbf{d}_{ab} for a π transition	149
A.2.5	\mathbf{d}_{ab} for a σ transition	149
A.3	TEM images of CdSe/CdS QD samples	151

List of Acronyms

A

A	Absorbance
ACN	Acetonitrile
AOM	Acousto-optic modulator
ASE	Amplified spontaneous emission
Au	Gold

B

BBO	Beta barium borate
-----	--------------------

C

Cd(OAc) ₂	Cadmium oleate
CMOS	Complementary metal oxide semiconductor
CW	Continuous-wave

D

DFB	Distributed feedback
DOS	Density of states

E

e-beam	Electron-beam
EBPVD	Electron beam physical vapor deposition
EM	Electro magnetic

F

FDTD	Finite-difference time-domain
FWHM	Full width at half maximum

H

HIS	Hot injection synthesis
H	High resolution
I	
IR	Infra red
K	
KK	Kramers-Kronig
L	
LB	Langmuir-Blodgett
O	
OPA	Optical parametric amplifier
P	
PECVD	Plasma-enhanced chemical vapour deposition
PIC	Photonic integrated circuit
PL	Photo-luminescence
PLDOS	Partial local density of states
Q	
QD	Quantum dot
QED	Quantum electrodynamics
QY	Quantum yield
R	
RIE	Reactive ion etching
S	
SE	Spontaneous emission
SEM	Scanning electron microscope
Si	Silicon
SiN	Silicon nitride
SiO	Silicon oxide
SOI	Silicon-on-insulator
SP	Single photon

T

TAS	Transient absorption spectroscopy
TE	Transverse electric
TEM	Transmission electron microscopy
TM	Transverse magnetic

T

MG	Maxwell Garnett
----	-----------------

N

NC	Nanocrystal
ND	Neutral density

V

VSL	Variable stripe length
-----	------------------------

W

WF	Write field
----	-------------

X

X	Exciton
XX	Biexciton

Nederlandse samenvatting

–Summary in Dutch–

Fotonica, ook genaamd de wetenschap van het licht, is een zeer breed onderzoeksgebied dat de generatie, manipulatie en detectie van licht omvat. Het bestrijkt een breede waaier van technische applicaties in datacommunicatie, detectie, beeldvorming en quantum gegevensverwerking. Het wordt beschouwd als een doorslaggevend onderzoeksgebied voor de ontwikkeling van de apparaten van de toekomst. Net zoals in de micro- en nano-elektronica vormt het schalen van fotonische apparaten de volgende stap in de evolutie en vele voorbeelden demonstreren de enorme impact die het zal hebben op het duurzaam en comfortabel maken van onze toekomstige manier van leven. Momenteel worden er grote inspanningen geleverd om verschillende fotonische functionaliteiten te combineren, zoals het genereren, routeren, detecteren en manipuleren van licht op eenzelfde fotonisch geïntegreerd circuit. Het onderzoek in deze thesis bevindt zich op het kruispunt van geïntegreerde fotonica en nanotechnologie, die materie op nanoschaal manipuleert. Op deze schaal zijn de klassieke natuurkundige wetten niet meer geldig en worden de regels gedicteerd door de quantummechanica, wat resulteert in nieuwe geavanceerde materialen. Colloïdale kwantumstippen (QDs) zijn momenteel het onderwerp van intens onderzoek vanwege hun manipuleerbare eigenschappen, zoals grootte- en vorm-afstelbare energieniveaus, levensduur van luminescentie, hoge quantumopbrengsten en chemische verwerkbaarheid. Ze zijn verkrijgbaar in een groot aantal materialen (CdSe, CdS, CdTe, ZnS, ZnSe, PbS, PbSe, ...), waardoor hun gebruik als luminescent materiaal over het hele zichtbare en nabij-infrarood spectrum (400 – 2000 nm) mogelijk is. Door deze QDs op te integreren in hoog technologische fotonische structuren, kan een breed scala aan actieve componenten worden ontwikkeld, waaronder bronnen en detectoren.

In dit onderzoek richten we ons op geïntegreerde lichtbronnen binnen het spectrum van het zichtbaar licht. In tegenstelling tot zuiver silicium dat absorbeert in het zichtbare spectrum, is siliciumnitride transparant voor zowel golflengtes in het zichtbare als het infrarode bereik, waardoor het toepassingsbereik wordt uitgebreid. Voor gegevensverwerking en telecomtoepassingen is nabij-infrarood licht belangrijk, terwijl voor biologische, spectroscopische en quantumoptische toepassingen het zichtbare spectrum belangrijk is. Net als silicium is siliciumnitride ook verenigbaar met de reeds ontwikkelde CMOS-fabricatietechnologieën, waardoor het een veelbelovend platform is voor de geïntegreerde fotonica. Na de ontwikkeling van een hybride integratieplatform in eerder werk, willen we nu verder de mogelijkheden maar ook de beperkingen van QDs voor geïntegreerde lichtbronnen verder verkennen.

‘Single’-fotonbronnen met colloïdale QDs

‘Single’-foton (SP) bronnen zijn belangrijk voor een tal van optische quantuminformatie toepassingen zoals quantum gegevensverwerking, quantumcryptografie en toevalsgeneratoren. In deze toepassingen wordt de foton-golffunctie verwerkt door er bewerkingen op uit te voeren zoals polarisatirotaties, faseverschuivingen en pad splitsing/recombinatie om informatie te de- of encoderen. We bestuderen de mogelijkheid om getriggerde solid-state SP-stralers rechtstreeks op een fotonische chip te integreren. Een grote uitdaging bestaat erin om hun emissie efficiënt in een enkele geleide mode te koppelen. Dit wordt door velen gezien als een struikelblok dat hun gebruik bij praktische implementaties uitsluit. Met behulp van 3D FDTD simulaties onderzochten we de SP-emissie van dipool-achtige stralers ingebed in verschillende siliciumnitride fotonische nanodraad golfgeleider-ontwerpen. Hoge koppelingsfactoren variërend tussen 40% en 67% werden gevonden in de vier onderzochte golfgeleidergeometrieën. Verder toonden we aan dat onder bepaalde geometrische omstandigheden het uitgezonden foton gekoppeld kan worden aan een enkele gepolariseerde geleide mode. In dat geval wordt een effectieve gepolariseerde (tot 96%) SP-bron gebouwd, zelfs wanneer de SP-straler zelf niet gepolariseerd is. Omdat het transparantiebereik van siliciumnitride zich uitstrekt van het zichtbare tot en met het infrarode spectrum, is het beoogde platform compatibel met verschillende soorten SP-stralers zoals colloïdale QDs, nanodeeltjes met een F-centrum en nano-

deeltjes gedopeerd met een enkel ion.

De koppeling van SP-stralers met diëlektrische caviteiten of plasmonische caviteiten/antennes is reeds gedeomnstreerd met behulp van verschillende soorten systemen, met als doel de bron helderder en meer directief te maken. De meeste van deze benaderingen zijn echter gebaseerd op de willekeurige positionering van stralers, wat de kans op het maken van goede bronnen sterk vermindert. Dit is een van de uitdagingen die vaak over het hoofd wordt gezien voor het ontwikkelen van een echt schaalbare SP-bron. Wij ontwikkelden een eenvoudige fabricagemethode, gebaseerd op elektronenstraal lithografie die een nauwkeurige positionering van zowel de straler als de caviteit mogelijk maakt. De nanocaviteiten bestaan uit een monolaag van QDs ingebed in een siliciumnitride-matrix ingeklemd tussen 2 goud lagen. Het gebruik van metalen in fotonische componenten is meestal nadelig vanwege de grote optische verliezen die hiermee gepaard gaan. Het gebruik van metalen biedt echter ook de mogelijkheid om licht te beperken in sub-golflengte dimensies dankzij het plasmonische effect. Aangezien de Purcell-factor F schaalt met Q/V , worden grote verbeteringen verwacht voor caviteiten met hoge Q-factoren en kleine mode-volumes. Onze metalen nanopatches – die overwegend diëlektrisch zijn – combineren de voordelen van een gematigde Q-factor (waardoor ze geschikt zijn voor werking bij kamertemperatuur) met een klein mode-volume, terwijl ze niet de grote optische verliezen vertonen die algemeen wel worden gevonden in plasmonische caviteiten. We ontwierpen een fabricage process waarmee grote reeksen van deze metalen nanocaviteiten kunnen worden gemaakt. Meer specifiek hebben we aangetoond dat een uniforme monolaag van colloïdale QDs nauwkeurig kan worden gepositioneerd in het midden van een siliciumnitride caviteit met sub-golflengte afmetingen, welke verder kan worden vermindert tot een enkele QD in toekomstige experimenten. Ten slotte hebben we ook het niet-exponentiële gedrag van de vervalcurves bestudeerd en verduidelijkt, die worden gevonden wanneer een straler niet in het centrum wordt geplaatst en in het geval van een laag van meerdere stralers. Beide bestudeerde SP-ontwerpen bieden een zeer flexibele route naar toekomstige on-chip quantum optische experimenten door de engineering van de straler te scheiden van de engineering van het fotonische circuit zelf.

Optische winst met colloïdale QDs

Colloïdale QDs zijn zeer geschikt als het actieve materiaal voor optische versterkers en lasers. Wanneer QDs gepompt worden met een zeer korte en hoge energetische (korte golflengte) puls van een laser, worden excitonen gecreëerd. Nadat deze excitonen zijn afgekoeld tot de band rand staten, induceren ze een reductie in het absorptiespectrum, omdat elektronische transitie worden geblokkeerd door de aanwezigheid van ladingdragers in deze niveaus. Deze verandering in absorptie kan aanleiding geven tot optische versterking en kan worden bestudeerd met een in de tijd verlate korte puls. Deze spectroscopische techniek wordt transient absorptie spectroscopy (TAS) genoemd en wordt gebruikt om de winsteigenschappen van QDs in een colloïdale dispersie te meten. Na de eerste demonstraties van optische winst in colloïdale QDs, zijn verschillende inspanningen geleverd om de algehele laserprestaties van deze materialen te verbeteren. Hoewel deze optimalisatie zich voornamelijk richtte op strategieën die de winstdrempel verlagen, mag de rol van de versterkingscoëfficiënt om laserwerking te bereiken niet over het hoofd worden gezien. Hier behandelen we zowel de relatie tussen de structuur van CdSe/CdS kern/schil QDs, hun optische winst – die we kwantificeren als de materiaalwinst – en hun drempel die nodig is om netto gestimuleerde emissie te bereiken. Gebaseerd op een vereenvoudigd model, voorspellen we dat het verminderen van de dikte van de CdS-schil gegroeid rond een gegeven CdSe-kern de maximale materiaalversterking zal vergroten, terwijl het vergroten van de schildikte de versterkingsdrempel verlaagt. Onze metingen bevestigen dat dunne-schil QDs de hoogste versterkingscoëfficiënten vertonen, in goede overeenstemming met het model, maar de significante drempelverlaging die wordt verwacht voor QDs met dikke schillen is afwezig. We relateren deze toenemende versterkingsdrempels voor dikkere schil QDs aan een overgang van een exciton-exciton afstoting (roodverschuiving) naar een aantrekking (blauwverschuiving) met toenemende schildikte. Dit maakt QDs met een grote kern/dunne schil tot de algemene kampioen kern/schil-configuratie in termen van zowel materiaalwinst, versterkingsdrempel als winstlevensduur. Deze inzichten zijn zeer waardevol om toekomstig werk bij het verbeteren van colloïdale QDs voor optische winst-toepassingen te verbeteren en om geoptimaliseerde QD-lasers te ontwikkelen.

Het is duidelijk dat materiaalwinst een zeer bruikbaar kenmerk is van colloïdale

QDs, omdat het toestaat om verschillende QD-morfologieën en materialen op dezelfde voet te bestuderen en te vergelijken. Door de materiaalwinst te vermenigvuldigen met de werkelijke volumefractie en mode-overlap, levert dit bovendien de winst van eender willekeurig QD-staal op. Omdat het gemakkelijk verkregen kan worden door een normalisatie van de niet-lineaire absorptie die kan gemeten worden met behulp van TAS, is het een nuttige ontwerp eigenschap, die ons voorziet van input voor een lagere limiet op het aanvaardbare verlies in een ontworpen fotonische component, alvorens de moeite te doen om de eigenlijke component te fabriceren. Dit werd geïllustreerd door het bestuderen van de mode-winst in eenvoudige $\text{SiN}_x/\text{QD}/\text{SiN}_x$ strip-golfgeleider versterkers.

Door de winst-eigenschappen van verschillende CdSe/CdS QD-stalen kwalitatief te bestuderen, hebben we een ‘beste’ sample kunnen kiezen om te gebruiken als versterkingsmateriaal in een geïntegreerde QD-laser. Gedistribueerde feedback (DFB)-lasers hebben een hoge reproduceerbaarheid in termen van golflengte en zijn theoretisch altijd single mode-lasers. Dit, samen met de eenvoudige fabricatieprocedure, maakt een DFB ontwerp een aantrekkelijke keuze voor een geïntegreerde single-mode laser met relatief lage lasing-drempels. De lasers vertoonden laserwerking wanneer er gepompt werd met ns-gepulste laser pulsen, wat eigenlijk al een quasi-continue golf is in vergelijking met de veel kortere levensduur van de bi-excitonen. Hoewel het uiteindelijke doel van het bereiken van een continue-golf-gepompte geïntegreerde laser nog niet bereikt werd, werd het potentieel van colloïdale QDs om het siliciumnitride-platform te verbeteren aangetoond, duidelijk wijzend op de groeicapaciteit van op QD gebaseerde winstmaterialen om de nodige lage lasing-drempels te bereiken in de nabije toekomst.

English summary

Photonics, also called the science of light, is a very broad research field which covers the generation, manipulation and detection of light. It covers a broad range of technical applications in the fields of data-communication, sensing, imaging and quantum computing and is considered to be a crucial research field for the development of next generation devices. Mirroring the success of micro- and nano-electronics, the down scaling of photonic devices constitutes the next step in this evolution and many examples demonstrate the huge impact it will have on making our future way of living sustainable and comfortable. Major efforts are now put into combining several photonic functionalities such as generating, routing, detecting and manipulating light on a single photonic integrated circuit (PIC). The research in this thesis is at the crossroads of integrated photonics and nanotechnology, which manipulates matter on the nano-scale. At this size regime the classical laws of physics break down and rules are dictated by quantum mechanics, resulting in interesting and new advanced materials. Colloidal quantum dots (QDs) are currently the subject of intense research because of their controllable properties, such as size- and shape-tunable energy levels and luminescence lifetimes, high quantum yields, and chemical processability. They are available in a large number of materials (CdSe, CdS, CdTe, ZnS, ZnSe, PbS, PbSe, ...), enabling their usage as luminescent materials over the whole visible and near-infra red (IR) wavelength range (400 – 2000 nm). Embedding these QDs into state-of-the-art photonic structures allows the development of a broad range of active devices including sources and detectors.

In this research we focus on integrated light sources in the visible light range. In contrast with pure silicon which is absorbing in the visible, silicon nitride (SiN) is transparent for both visible and infrared wavelengths, broadening the range of applications. While the near infrared range is rel-

evant for data processing and telecom application, the visible range is of great importance for biological, spectroscopical and quantum optical applications. Just like silicon, silicon nitride is also compatible with the well-established CMOS-processing technologies, making it a promising platform for integrated photonics. Following the development of a hybrid integration platform established in previous work, we aim at further exploring the potential and inevitable limitations of QDs for on-chip integrated light sources.

Single-photon sources with colloidal QDs

Single-photon (SP) sources are important for a number of optical quantum information processing applications such as quantum computing, quantum cryptography, and random number generation. In these applications, the photon wave function is processed by performing operations such as polarization rotations, phase shifts and path splitting/recombination in order to encode or decode information. We study the possibility to integrate triggered solid-state SP emitters directly on a photonic chip. A major challenge consists in efficiently extracting their emission into a single guided mode. This is seen by many as a stumbling block precluding their usage in practical implementations. Using 3D finite-difference time-domain simulations, we investigated the SP emission from dipole-like nanometer-sized inclusions embedded into different silicon nitride photonic nanowire waveguide designs. High coupling factors ranging between 40% and 67% were found in the four waveguide geometries under investigation. Furthermore, we showed that under certain geometrical conditions, the emitted photon can be coupled to a single polarized guided mode. In that case, an effective polarized (up to 96%) SP source is built even if the SP emitter itself is unpolarized. Because the silicon nitride transparency ranges from the visible to the infrared, the envisaged platform is compatible with several types of SP emitting inclusions such as colloidal quantum dots, nanoparticles containing a single color centre, and single-ion doped nanoparticles.

The coupling of single-photon emitters to dielectric cavities or plasmonic cavities/antennas has been demonstrated using a variety of physical systems with the aim of making the source brighter and more directive. However most of these approaches are based on the random deposition of emitters, which strongly reduces the yield of fabricating good sources. This is one

of the challenges that is often overlooked for having a truly scalable single-photon source. We have developed a straightforward fabrication method, based on electron-beam lithography that allows a precise control on the positioning of both emitter and cavity. The nanopatch cavities consist of a monolayer of QDs embedded in a silicon nitride matrix sandwiched between two gold (Au) layers. Using metals in photonic devices is usually detrimental because of the large optical losses associated with them. However, the use of metals offers the possibility to confine light in subwavelength dimensions because of the plasmonic effect. As the Purcell factor F scales with Q/V , large enhancements are expected for cavities with high Q-factors and small mode volumes. Our metallic nanopatches – which are predominantly dielectric – combine the benefits of a moderate Q-factors (making them suitable for room-temperature operation) with a small mode volume, while not having the large optical losses generally found in plasmonic cavities. A fabrication process was designed that allows for the fabrication of large arrays of these metallic nanopatch cavities. More specifically we demonstrated that a uniform monolayer of colloidal QDs can be precisely positioned in the center of a sub-wavelength SiN_x/Au cavity, which can be further patterned down to a single QD in future experiments. Finally we have also studied and clarified the non-exponential behaviour of the decay traces when an emitter is placed off center or in the case of a film of multiple emitters. Both of the above approach offers a very flexible route to future on-chip quantum optics experiments by separating the engineering of the emitter from the engineering of the photonic circuit itself.

Optical gain with colloidal QDs

Colloidal QDs are highly attractive as the active material for optical amplifiers and lasers. When QDs are pumped with a very short and high energy (short wavelength) laser pulse, excitons are created. After these excitons have cooled to the band edge states, they induce a bleach of the absorption spectrum as electronic transitions get blocked by the presence of carriers in these levels. This change in absorption can give rise to optical gain, which can be probed with a time-delayed short pulse. This spectroscopic technique, called transient absorption spectroscopy (TAS), allows to characterize gain properties of QDs in a colloidal dispersion. After the first demonstrations of optical gain in colloidal QDs, several efforts have been made to improve the overall lasing performance of these materials. Al-

though this optimization mainly focused on strategies that reduce the gain threshold, the role of the gain coefficient to reach lasing action should not be overlooked. Here, we address both the relation between the structure of CdSe/CdS core/shell QDs, their optical gain – which we quantify as the material gain – and their threshold needed to attain net stimulated emission. Based on a simplified model, we predict that reducing the thickness of the CdS shell grown around a given CdSe core will increase the maximal material gain, while increasing the shell thickness will lower the gain threshold. Our measurements confirm that thin-shell QDs exhibit the highest gain coefficients, in good agreement with the model, but the significant threshold reduction expected for thick-shell QDs is absent. We relate this increasing gain thresholds for thicker-shell QDs to a transition from an exciton-exciton repulsion (redshift) to attraction (blueshift) with increasing shell thickness. This makes large-core/thin-shell QDs the overall champion core/shell configuration in terms of both material gain, gain threshold and gain lifetime. These insights are most valuable to guide future work to improve colloidal QDs for optical gain applications and develop optimized QD-lasers.

It is clear that material gain is a most useful characteristic of colloidal QDs, as it allows to study and compare different QD morphologies and materials on the same footing. In addition, multiplying this number with the actual volume fraction and modal overlap, yields the gain of any QD sample. As it can be conveniently obtained from a normalization of the non-linear absorbance, measured using TAS, it is a helpful design property that provides us with input for a lower limit of the acceptable loss when developing nanophotonic components, before going through the effort of actually fabricating them. This was exemplified by studying the modal gain in simple $\text{SiN}_x/\text{QD}/\text{SiN}_x$ stripwaveguide amplifiers.

By qualitatively studying the gain properties of several CdSe/CdS QD samples we decided upon a ‘best’ sample to be used as gain material in an integrated QD-laser. Distributed feedback (DFB)-lasers have a high reproducibility in terms of wavelength and theoretically are all single mode-lasers. This, together with its straightforward fabrication process, makes a DFB-design an attractive choice as an integrated single mode laser with relatively low lasing thresholds. The fabricated QD-DFB-lasers showed lasing under ns-pumping, which is actually quasi-continuous wave (CW) compared to the

much shorter biexciton lifetime. Even though the final goal of developing a CW-pumped integrated QD-laser was not yet reached, the potential for colloidal QDs to enhance the SiN-platform was demonstrated, clearly pointing towards the potential of QD based gain media to reach the necessary low threshold densities in the near future.

1

Introduction

In this chapter the research background is introduced, followed by the relevant basic principles of colloidal quantum dots, light-matter interaction, integrated photonics and ultra-fast spectroscopy. Finally, an outline of the thesis and an overview of scientific publications is presented.

1.1 Research background

Photonics, also called the science of light, is a very broad research field which covers the generation, manipulation and detection of light. From the very beginning of modern science in the 17th century, the invention of optical microscopes and telescopes boosted research to the benefit of society. Similar revolutions were initiated by the development of optical spectroscopy in the 19th century and later fibre optic communication in the late 20th century. The word ‘photonics’, derived from photon the elementary particle constituting light, first appeared in the late 1960s to describe a research field whose goal was to use light to perform functions that traditionally fell within the typical domain of electronics, such as telecommunication, information processing, etc. Nowadays it has a broad range of technical applications in the fields of data-communication, sensing, imaging and quantum computing

and is considered to be a crucial research field for the development of next generation devices.

Mirroring the success of micro- and nano-electronics, the down scaling of photonic devices constitutes the next step in this evolution and many examples demonstrate the huge impact it will have on making our future way of living sustainable and comfortable. Major efforts are now put into combining several photonic functionalities such as generating, routing, detecting and manipulating light on a single PIC. Silicon photonics is a promising platform for integrated photonics applications as it allows to reuse the already mature CMOS (Complementary Metal-Oxide-Semiconductor) platform developed for the electronics industry. Together with silicon's high refractive index ($n = 3.48$ at 1550 nm) compared to its native oxide silica ($n = 1.45$) and air ($n = 1$), allows for the confinement of light in very compact waveguides. These waveguides can have bends with very small radii, down to a few micrometer, without significant loss such that very dense photonic circuits can be created.

Despite the great promises of Silicon photonics, there is still continued interest and real efforts in pursuing other materials for realising a photonic platform. Nowadays, silicon nitride photonics is emerging as a new platform for guiding light and building micro-photonic devices such as interferometers, resonators and spectrometers on a chip.^{1;2} As the more standard and mature Silicon platform, it is fully compatible with standard CMOS technology and takes advantage of the most advanced lithographic techniques developed for the electronics industry. In contrast with pure silicon which is absorbing in the visible, silicon nitride is transparent for both visible and infrared wavelengths, broadening the range of applications.³ While the near infrared range is relevant for data processing and telecom application, the visible range is of great importance for biological, spectroscopical and quantum optical applications of micro-photonics. Silicon nitride integrated photonic devices offer a fairly high index ($n = 2$) contrast with air and silicon oxide (SiO) and although the contrast is smaller than in the case of silicon (Si), it is not really a limiting factor. Not only, does such a contrast still allow a high density of integration, but it also reduces scattering losses and makes the devices more tolerant to fabrication imperfections. In recent experimental work very low-loss waveguiding (0.51 dB/cm)³ and high-Q factor (10^6) cavities⁴ have been demonstrated using the silicon nitride platform.

However, silicon nitride being a transparent material, it cannot be used

to generate or detect light. To build a complete system-on-chip solution (including sources, detectors, switches ...), the silicon nitride technology must be combined with an active material, able to absorb and emit photons. A promising solution consists of developing a *hybrid* technology, in which the silicon nitride platform is combined with optical nanomaterials such as colloidal QDs. Embedding these QDs into silicon nitride devices allows the development of a broad range of active devices including sources and detectors. QDs are currently the subject of intense research because of their controllable properties, such as a size- and shape-tunable energy levels and luminescence lifetimes, high quantum yields, and chemical processability. Because of their unique light absorption and emission properties, much effort has been devoted to their integration with conductive (organic and inorganic) layers to build QD-LEDs⁵ and QD-detectors.⁶ Their integration within dielectric host materials to make optically pumped solid-state QD-lasers has also been attempted by many groups but has led to controversial results⁷ due to the difficulty to (i) realise sufficient population inversion in state-of-the art QDs and (ii) fully embed them inside the material. Recently, silicon nitride microcavities with embedded quantum dots have been successfully demonstrated by our group^{8;9} and by competitors,^{10–12} paving the way for more sophisticated QD-SiN photonics devices. Combining high-quality and highly customisable luminescent materials such as colloidal QDs, with high-quality waveguiding and resonating micro/nanostructures made of silicon nitride presents a real asset and offers many perspectives in the fields of biophotonics (*e.g.* lab-on-chip applications), sensing (*e.g.* detecting molecules in air), signal processing (*e.g.* all optical routing, interfacing optics and electronics), and quantum optics (*e.g.* single-photon emission for quantum cryptography protocols, quantum information processing).

1.2 Colloidal quantum dots

Colloidal quantum dots (QDs) are nanometer-sized semiconductor structures made of a few thousands of atoms. Due to their small size, the electrons and holes are strongly spatially confined, which significantly modifies their electronic and optical properties compared to bulk crystals with identical chemical composition and crystalline structure. Due to quantum confinement, the usual valence and conduction bands break up into discrete energy-levels, with an increasing bandgap (E_g) for decreasing dot size (see Fig. 1.1). For this reason, colloidal QDs are sometimes referred to as ‘artificial atoms’. Their surface is typically passivated by ligands, which keep them stable in a colloidal dispersion (see Figs. 1.2a and 1.2b). These ligands are often long chain organic molecules such as fatty acids, but also shorter

inorganic ligands are possible.

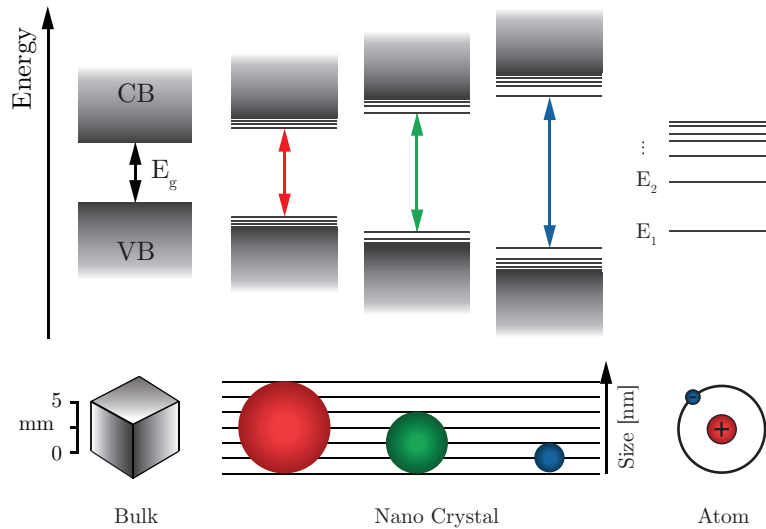


Figure 1.1: Schematic illustration of the density of states in an atom, colloidal quantum dots of different sizes and bulk semiconductor, illustrating the crossover between the different regimes.

Colloidal QDs are, as opposed to their epitaxially grown counterparts, obtained through cheap wet-chemical synthesis methods and can be engineered to a very high extent, offering a pathway to precisely tune the opto-electronic properties of the material. The ability to engineer the QDs together with the large number of available materials (CdSe, CdS, CdTe, ZnS, ZnSe, PbS, PbSe, ...) enables their usage as luminescent materials over the whole visible and near-IR wavelength range (400 – 2000 nm). This tuning by size has been further extended toward tuning by shape and tuning by heterostructure formation, *e.g.*, QDs composed of two materials in a core/shell configuration (see Fig. 1.2c). These tuning strategies provide additional degrees of freedom to control non-radiative multi-exciton decay rates, limit ionization and improve the overall chemical stability of the particles. The solution based approach allows to fabricate devices using straightforward wet-processing techniques, such as drop casting, spincoating, Langmuir-Blodgett deposition, etc. Hence these particles can be easily deposited or integrated in any host material or existing technology platforms, *e.g.* silicon photonics (see Section 1.3.1).

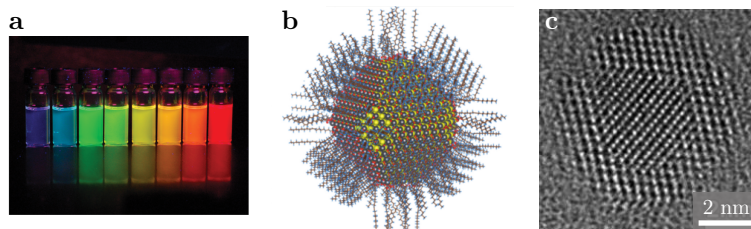


Figure 1.2: (a) Vials with colloid dispersions of CdSe/CdS QDs of different sizes under UV excitation. (b) Depiction of a QD with inorganic core and organic ligand shell. (c) HR-TEM image of a core/shell PbTe/CdTe particle showing the stacking of individual atoms building up the QD.

1.2.1 Wet chemical synthesis

Over the last 25 years, the synthesis of colloidal nanocrystals (NCs) by means of wet chemical synthesis where metal-organic precursors are injected into a hot ($50^{\circ}\text{C} - 360^{\circ}\text{C}$) coordinating solvent, has seen a tremendous development. Initially developed to form spheric, cadmium chalcogenide NCs,¹³ the so-called hot injection synthesis (HIS) technique has been quickly extended to a range of metal, metal oxide and semiconductor NCs.¹⁴⁻¹⁶ The method relies on the formation of a supersaturated reaction mixture by rapid generation of solution-phase monomers out of the precursors. The supersaturation initiates a homogeneous nucleation and growth process, consuming the monomers to form the actual nanocrystal colloids which are capped with organic ligands. The synthesis method gives access to sizeable amounts of monodisperse NCs with an exceptional control over size and shape. This fabrication method offers a wide degree of freedom when designing nanocrystals as the size, shape, composition and surface functionalization can be engineered and optimised for a specific application. Moreover, the development of new and improved synthesis methods is still a very active research field as continuous efforts are being put into improving the quality, reach even smaller size dispersions and expand the range of materials that can be produced with the HIS. For example, various core/shell structures have been produced, where the surface passivation by the additional shell increases the photoluminescence quantum yield.^{17;18}

1.2.2 Optoelectronic properties

As mentioned above, the electronic levels in a quantum dot strongly depends on the size and shape of the particle due to the quantum confinement effect, allowing to precisely tune the opto-electronic properties (*e.g.* the bandgap) of a material. In this section we briefly give an overview of the most relevant linear optical properties relevant for future chapters.

1.2.2.1 Light absorption and emission

When an electron-hole pair is created, the electron and hole quickly cool to the band edges where they form an exciton. These neutral quasiparticles are formed by the mutual attraction between the electron and hole, having an opposite charge. The total energy of this state is different than the sum of the individual particle energies which is mainly due to the Coulomb interaction energy. Free carriers can be created through various processes. One example is *absorption*, where a high energy photon ($E_{ph} > E_g$) is absorbed (see Fig. 1.3), but also the direct injection of electrons and holes through electrical contacts is possible.

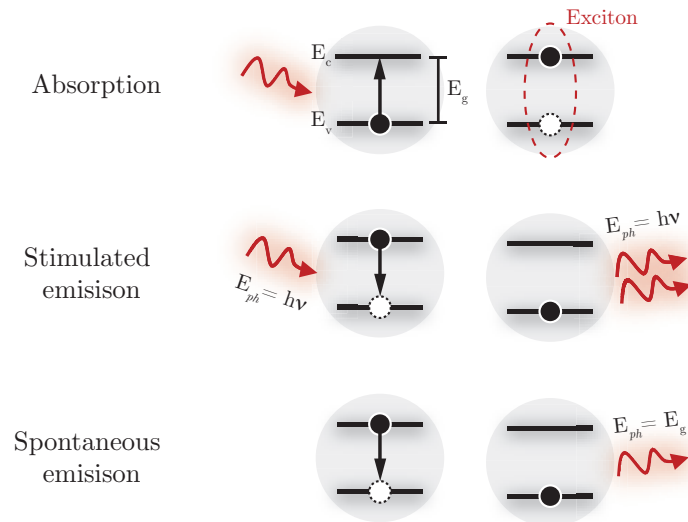


Figure 1.3: Schematic representation of the fundamental light-matter interactions: absorption, stimulated emission and spontaneous emission.

Once an exciton is created – i.e. the QD is excited – the exciton can recombine dissipating its energy in the process. This energy dissipation can either happen radiatively, creating a photon with a photon energy matching the energy difference, or non-radiatively. The emission process where an electron ‘spontaneously’ – i.e. without any outside influence – decays from a higher energy level to a lower one is called *spontaneous emission* (see Fig. 1.3). When the exciton was created through the absorption of a photon, the emission is called photoluminescence, while in the case of electrical injection it is called electroluminescence. The radiative decay time of the fundamental excitonic transition is of the order of 30 ns for visible quantum dots¹⁹ and of 1 μ s for IR emitting quantum dots.²⁰ Similarly, *stimulated emission* is the process by which an electron is ‘stimulated’ to jump from a higher energy level to a lower one by the presence of electromagnetic radiation – i.e. a photon – at the frequency of the transition (see Fig. 1.3).

For QDs in the single-exciton regime, the main non-radiative decay process is carrier trapping in defect states that arise either at the surface (through *e.g.* dangling bonds) or in the bulk of the QD through lattice defects. Considering the large surface-to-volume ratio in QDs, the number of surface defects can be significant, especially for small particle sizes. Therefore, an important step in improving the quantum yield (QY) of QDs, is by using core/shell QDs. Typically an additional layer, the shell, of a high bandgap material is grown around the QD offering improved surface passivation as the outer shell layer protects the core states from the surface dangling bonds.

For multi-exciton states, non-radiative Auger recombination is the main exciton loss mechanism. Auger recombination is a non-radiative process where the electron-hole recombination energy is transferred to a third particle (an electron or hole) which is then promoted to a higher energy state. Next its excess energy is dissipated through collisions with lattice vibrations (phonons). As such, the energy of the exciton is lost as heat instead of photon emission, hence the term ‘non-radiative’. Since it is a three-particle process, the rate of Auger recombination scales with the cube of the carrier density. In addition, as carriers are confined close together in the small volume of a QD, Auger recombination is a very efficient process in QDs, leading to bi-exciton (a double exciton) lifetimes τ_{XX} on the order of a few tens of picoseconds, much faster than the typical single exciton radiative lifetimes τ_X (tens of nanoseconds to microseconds). This makes Auger recombination a limiting process in applications that require high carrier densities and long inversion lifetimes such as lasers.

1.2.2.2 Dependence of the optical band gap

When the size of a semiconductor nanocrystal or quantum dot (QD) becomes on the order of the Bohr exciton radius, which is the most probable distance between an electron-hole pair in a bulk semiconductor, the electrons and holes are tightly confined by the dimensions of the QD. This system can be described using the quantum mechanical particle-in-a-box model, where a particle – an exciton – is confined in a spherical potential well – the QD – with radius R . Solving the Schrödinger equation using infinite potential well boundary conditions the eigenenergies E_n can be found:

$$E_n = \frac{n^2 \hbar \pi^2}{8m_r R^2} \quad (1.1)$$

with m_r the reduced electron mass in the semiconductor material. It can be seen that the eigenenergies will increase when the size of the box becomes smaller; more energy is needed to confine the particle in this smaller volume. The exciton being confined by the dimensions of the QD particle, hence lead to a transition from continuous to discrete energy levels, which strongly depend on the size of the QD particle. When also taking into account the screened Coulombic interaction between the electron and hole, which can be described using first order perturbation theory, the famous ‘Brus’ formula for the (optical) band gap can be found:²¹

$$E_g = E_{g,\text{bulk}} + \frac{\hbar \pi^2}{8m_r R^2} - \frac{1.786e^2}{\epsilon R} \quad (1.2)$$

with ϵ the dielectric constant of the semiconductor material. It is an approximate formula that describes the lowest excited electronic state energy ($n = 1$) or in other words the energy required to create an exciton in a quantum dot. The fundamental excitation energy depends both on the semiconductor material ($E_{g,\text{bulk}}$) and on the dimensionality of the QD (R). Therefore one has to choose the appropriate bulk material having a material band gap in the desired wavelength range (*e.g.* CdSe with 1.74 eV is suitable for visible light), and next fine tune to the desired wavelength by changing the size of the particles. Figure 1.4 shows absorption and emission spectra of CdSe QDs of different sizes, where size reduction leads to an energy increase of the material band gap over its bulk value or equivalently a blueshift in the optical absorption and emission spectra. Since the band gap of the QDs is very sensitive to their size, small variations on the size give rise to variations in the emission energy leading to so-called inhomogeneous broadening. Therefore a good control of the particles size (*i.e.* the chemical synthesis) is crucial to obtain narrow emission and absorption features.

When observing the absorption and emission spectra of these QDs, one can see that the band edge exciton emission is slightly red-shifted compared to the exciton absorption peak. This shift is commonly referred to as the Stokes shift and can be caused by several mechanisms. For example when the emission of a photon is accompanied by the emission/absorption of a phonon the emitted photon has less/more energy than the absorbed photon, this energy difference due to the exciton-phonon coupling results in a spectral shift. But also re-absorption can be significant, especially in high concentration solutions or compact films. In this case shorter wavelengths can get easily reabsorbed by the larger particles in an ensemble with inhomogeneous size, red-shifting the emission spectrum.

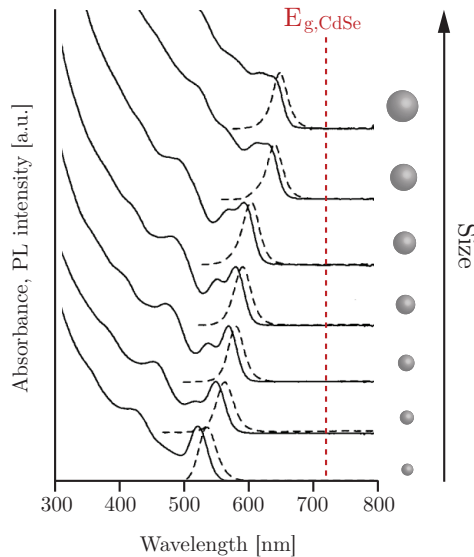


Figure 1.4: Absorption and emission spectra of CdSe QDs. As the CdSe QD becomes bigger, the excitonic feature will red-shift. The bandgap energy in bulk CdSe ($E_{g,CdSe} = 1.74$ eV) is indicated in red. Adapted from reference²².

1.2.2.3 Maxwell Garnett effective medium approximation

To describe the optical properties of a composite medium such as a colloidal dispersion of nanocrystals in an organic solvent, effective medium theories can be used. These kind of theories describe the macroscopic properties

of composite materials by developing a new *effective* parameter which is a weighted average based on the properties and the relative fractions of its components. In the Maxwell-Garnett (MG) approximation, the dielectric constants of the inclusions $\tilde{\varepsilon} = \varepsilon_{\text{R}} + i\varepsilon_{\text{I}}$ and surrounding transparent solvent $\varepsilon_{\text{s}} = n_{\text{s}}^2$ are replaced by an effective one $\tilde{\varepsilon}_{\text{eff}}$, which depends on the volume fraction f of the inclusions (the volume occupied by QDs per unit of sample volume):²³

$$\tilde{\varepsilon}_{\text{eff}} = \frac{1 + 2\beta f}{1 - \beta f} \varepsilon_{\text{s}} \quad (1.3)$$

with $\beta = \frac{\tilde{\varepsilon} - \varepsilon_{\text{s}}}{\tilde{\varepsilon} + 2\varepsilon_{\text{s}}}$. The MG approach is based on the assumption that point dipoles in a homogeneous host medium do not interact (*e.g.* through near- or far-field electrostatic interactions), and is therefore expected to be only valid for low volume fractions ($f \ll 1$). In this case the real and imaginary part can be simplified to

$$\varepsilon_{\text{eff,R}} = \varepsilon_{\text{s}} \quad (1.4a)$$

$$\varepsilon_{\text{eff,I}} = \frac{9\varepsilon_{\text{s}}^2}{|\tilde{\varepsilon} + 2\varepsilon_{\text{s}}|^2} f \varepsilon_{\text{I}} \quad (1.4b)$$

Hence, $\varepsilon_{\text{eff,R}}$ is reduced to the real dielectric function of the solvent. $\varepsilon_{\text{eff,I}}$ on the other hand finds an elegant interpretation within the concept of the *local field factor* f_{LF} , which is defined as

$$f_{\text{LF}} = \frac{3\varepsilon_{\text{s}}}{\tilde{\varepsilon} + 2\varepsilon_{\text{s}}} \quad (1.5)$$

This local field correction factor expresses the difference between the local field $\mathbf{E}_{\text{local}}$ inside the QD, relative to the macroscopic external field \mathbf{E} .

$$\mathbf{E}_{\text{local}} = f_{\text{LF}} \mathbf{E} \quad (1.6)$$

Indeed, in the case of a QD dispersion, the organic solvent (*e.g.* for toluene $\varepsilon_{\text{s}} = 2.25$) has a considerable smaller permittivity than $|\tilde{\varepsilon}|$, resulting in a local field factor which is typically smaller than one and therefore confirms the idea of screening, where the electric field is driven outside of the QD, reducing the local field inside the QD compared to the external field. Equation (1.4b) becomes

$$\varepsilon_{\text{eff,I}} = |f_{\text{LF}}|^2 f \varepsilon_{\text{I}} \quad (1.7)$$

revealing that $\varepsilon_{\text{eff,I}}$ simply equals the imaginary part of the QD dielectric function, rescaled by the QD volume fraction f and the local field factor f_{LF} .

1.2.2.4 Intrinsic absorption coefficient

The intrinsic absorption coefficient μ_i is a convenient quantity to describe light absorption by a dilute dispersion of nanocrystals. The quantity typically determined in an absorption measurement is the absorbance A which is defined as the base-10 logarithm of the ratio between the incident I_0 and the transmitted I_t light intensity²³

$$A = \log\left(\frac{I_0}{I_t}\right) \quad (1.8)$$

Since A depends on the thickness L of the sample, the measured absorbance is a sample property and not a material property. This A can however be related to the extinction coefficient κ , which is the imaginary part of the complex refractive index $\tilde{n} = n + i\kappa$, making it independent of the thickness and hence a material property. This material property, the absorption coefficient α is defined as follows:

$$\alpha = \frac{\ln(10)A}{L} = \frac{4\pi\kappa}{\lambda} \quad (1.9)$$

This relation remains valid in the case of a MG composite medium, where κ is replaced by an effective extinction coefficient κ_{eff} with $\varepsilon_{\text{eff,I}} = 2n_{\text{eff}}\kappa_{\text{eff}}$. Calling the *absorption coefficient* of the composite μ , we obtain

$$\mu = \frac{\ln(10)A}{L} = \frac{4\pi\kappa_{\text{eff}}}{\lambda} \quad (1.10)$$

Using the MG expressions for $\varepsilon_{\text{eff,R}}$ (Eq. (1.4a)) and $\varepsilon_{\text{eff,I}}$ (Eq. (1.4b)), yields the absorption coefficient μ for a dispersion of QDs as

$$\mu = \frac{2\pi}{\lambda n_s} |f_{\text{LF}}|^2 f \varepsilon_{\text{I}} \quad (1.11)$$

Since μ increases proportionally to f , it makes sense to define an intrinsic absorption coefficient μ_i as:

$$\mu_i = \frac{\mu}{f} = \frac{\ln(10)A}{fL} = \frac{2\pi}{\lambda n_s} \frac{9n_s^4}{(\varepsilon_{\text{R}} + 2n_s^2)^2 + \varepsilon_{\text{I}}^2} \varepsilon_{\text{I}}^2 \quad (1.12)$$

It can be seen from Eq. (1.12) that μ_i only depends on the optical constants of the QDs and the surrounding host, making μ_i a key material property characterizing light absorption by QDs dispersed in a given solvent. For many quasi-spherical QDs, it has been found that μ_i becomes size-independent at short wavelengths with an experimentally verified value

closely matching the value predicted by Eq. (1.12) when using the bulk dielectric function of the QD constituent material. When the dielectric environment of the QDs changes, *e.g.* upon film formation, the local field factor in Eq. (1.12) might change slightly. *E.g.* in thin films, where the permittivity of the QD environment is typically higher compared to dispersion, leads to an increase of the local field factor and hence a slightly larger μ_i can be expected. For materials with different shapes or core/shell composition, Eq. (1.12) must be replaced by more elaborate expressions. It has been found that also for these different shapes the same short wavelength limit applies.²⁴ In the case of core/shell particles, the complication comes from the additional screening by the shell. A more elaborate expression for μ_i of a core/shell QD has been proposed by Neeves *et al.*²⁵, where the indices ‘c’ and ‘sh’ refer to core and shell, respectively:

$$\begin{aligned} \mu_i &= \frac{2\pi}{\lambda n_s} \text{Im}(3\epsilon_s \beta) \\ \text{with } \beta &= \frac{\epsilon_{\text{sh}}\epsilon_a - \epsilon_s\epsilon_b}{\epsilon_{\text{sh}}\epsilon_a + 2\epsilon_s\epsilon_b}, \\ \epsilon_a &= \epsilon_c \left(3 - 2\frac{V_{\text{sh}}}{V_{\text{qd}}} \right) + 2\epsilon_{\text{sh}}\frac{V_{\text{sh}}}{V_{\text{qd}}}, \\ \epsilon_b &= \epsilon_c\frac{V_{\text{sh}}}{V_{\text{qd}}} + \epsilon_{\text{sh}} \left(3 - \frac{V_{\text{sh}}}{V_{\text{qd}}} \right) \end{aligned} \quad (1.13)$$

It can be seen that μ_i no longer solely depends on optical constants, but also on the ratio of the shell volume over the total QD volume f_{sh} . This ratio can be obtained by transmission electron microscopy (TEM) imaging of the core and the core/shell QDs. Figure 1.5a shows the calculated intrinsic absorption coefficient of wurtzite CdSe/CdS in toluene as a function of shell volume fraction, at wavelength 300 nm and 350 nm using Eq. (1.13) and the bulk dielectric constants of CdSe and CdS.

The approach outlined above allows us to calculate a μ_i -spectrum from a regular absorbance spectrum $A(\lambda)$, regardless of the QDs’ dimensions, once the value for μ_i is known at a reference wavelength (*e.g.* $\lambda_{\text{ref}} = 300$ nm):

$$\mu_i(\lambda) = \frac{A(\lambda)}{A(\lambda_{\text{ref}})} \mu_i(\lambda_{\text{ref}}) \quad (1.14)$$

An example is shown in Figure 1.5b. In addition the intrinsic absorption coefficient is also a powerful parameter in the context of optical gain, as will

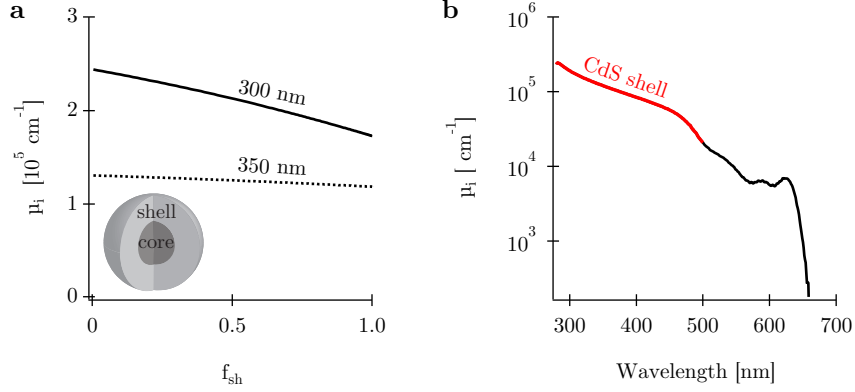


Figure 1.5: (a) Calculated intrinsic absorption coefficient of wurtzite CdSe/CdS in toluene at wavelength 300 nm and 350 nm, for varying composition. (b) μ_i spectrum of a typical CdSe/CdS QD on a logarithmic scale showing the contribution of the strong CdS shell absorption at shorter wavelengths.

be shown in Chapter 4, where the concept of material gain is introduced. Finally we can also define the absorption cross section σ_{abs} as

$$\sigma_{abs} = V_{qd} \mu_i \quad (1.15)$$

where V_{qd} is the volume of a single QD and σ_{abs} has units of area.

1.2.3 Transition rates: quantum picture

Fermi's golden rule is a formula that describes the transition rate (probability of transition per unit time) from one energy eigenstate of a quantum system into another energy eigenstate. The absorption of light with angular frequency ω by a QD, is such a transition, where an energy quantum $\hbar\omega$ (the photon) from a radiation field, results in a transition in the absorbing system (the QD) from an initial state ' i ' to a final state ' f '. The transition rate is given by²⁶

$$\Gamma_{i \rightarrow f} = \frac{2\pi}{\hbar^2} \sum_f \left| \langle f | \hat{H}_1 | i \rangle \right|^2 \delta(\omega_i - \omega_f) \quad (1.16)$$

where $\hat{H}_1 = -\hat{\mu} \cdot \hat{\mathbf{E}}$ is the interaction Hamiltonian in the dipole approximation. This approximation states that 'small' electronic systems, such as

a QD, predominantly behave as a Hertzian dipole with dipole moment μ . The Dirac function ensures energy conservation.

1.2.3.1 Rate of absorption and oscillator strength

When approximating a QD as an exciton two-level system, the absorption of a photon with energy $E = \hbar\omega$ is only possible for a transition from an initial state to a final state, with respective energies of E_1 and E_2 for which $E_2 - E_1 = \hbar\omega$ is valid. For spherical particles in a dielectric medium, the local field E_{loc} is related to the spectral density $\rho(E)$ of the radiation field at energy E through the local field factor f_{LF} , resulting in

$$\Gamma_{1 \rightarrow 2} = \frac{e^2 \pi}{\hbar \epsilon_s \epsilon_0} |\langle 2 | \mathbf{e} \cdot \mathbf{r} | 1 \rangle|^2 |f_{LF}|^2 \rho(E) \quad (1.17)$$

where \mathbf{e} is the polarization vector of the incident light field and \mathbf{r} is the position operator of the electron making the transition between levels 1 and 2. It can be seen that the transition rate depends on two factors: a ‘field’ part which describes the spectral density of the environment, and a ‘system part’ corresponding to the transition matrix describing the internal structure of the system and the strength of the transition between the two states. This transition strength is often referred to as the oscillator strength f_{12} , which is defined as:

$$f_{12} = \frac{2m\omega}{3\hbar} |\langle 2 | \mathbf{r} | 1 \rangle|^2 \quad (1.18)$$

It is a dimensionless number that compares the absorption of light by a quantum transition with a classical electronic oscillator of the same frequency.

1.2.3.2 Spontaneous emission rates and Purcell factor

Spontaneous decay is a pure quantum effect and hence requires a quantum electrodynamics (QED) treatment. Unlike stimulated emission which is the result of an externally applied EM field, spontaneous emission is the result of fluctuations in the vacuum field E_{vac} . Before Purcell’s analysis in 1946,²⁷ spontaneous emission was considered a radiative intrinsic property of atoms or molecules. Purcell noted that, in case the emitter is placed in a resonant cavity, the spontaneous decay rate can be enhanced compared to the free-space decay rate.

Consider a simple non-degenerate dipole transition $|b\rangle \rightarrow |a\rangle$ with a dipole

moment matrix element \mathbf{d}_{ab} in vacuum, the rate of spontaneous emission from $|b\rangle$ to $|a\rangle$ is given by Fermi's golden rule

$$\Gamma^{(\text{QED})} = \frac{2\pi}{\hbar^2} \sum_{\lambda} |\mathbf{d}_{ab} \cdot \boldsymbol{\mathcal{E}}_{\text{vac},\lambda}(\mathbf{r}_0)| \delta(\omega_{\lambda} - \omega_{ab}) \quad (1.19)$$

where λ is the mode index and the *vacuum field* is defined as

$$\boldsymbol{\mathcal{E}}_{\text{vac},\lambda}(\mathbf{r}) = \sqrt{\frac{\hbar\omega_{\lambda}}{2\epsilon_0}} \mathbf{v}_{\lambda}(\mathbf{r}), \quad (1.20)$$

where $\mathbf{v}_{\lambda}(\mathbf{r})$ is the *normalized* mode function:

$$\int \mathbf{v}_{\lambda}(\mathbf{r}) \cdot \mathbf{v}_{\mu}(\mathbf{r}) d^3r = \delta_{\lambda\mu}. \quad (1.21)$$

It can be found that Eq. (1.19) can be written as follows (see appendix A.1):

$$\frac{\Gamma^{(\text{QED})}}{\Gamma_0^{(\text{QED})}} = \frac{6\pi c}{\omega_{ab}} \left\{ \mathbf{n}_{ab}^{\dagger} \Im [\boldsymbol{\mathcal{G}}(\mathbf{r}_0, \mathbf{r}_0, \omega_{ab})] \mathbf{n}_{ab} \right\} \quad (1.22)$$

with

$$\Gamma_0^{(\text{QED})} = \frac{\omega_{ab}^3 |\mathbf{d}_{ab}|^2}{3\pi \hbar \epsilon_0 c^3}, \quad (1.23)$$

the decay rate in free space vacuum. The quantity

$$\rho_{\mathbf{n}}(\mathbf{r}, \omega) = \frac{6\omega}{\pi c^2} \left\{ \mathbf{n}^{\dagger} \Im [\boldsymbol{\mathcal{G}}(\mathbf{r}, \mathbf{r}, \omega)] \mathbf{n} \right\} \quad (1.24)$$

is called the *partial local density of states* (PLDOS) at the point \mathbf{r} and at frequency ω . It corresponds to the number of modes per unit volume and frequency, at the origin \mathbf{r} of the (point-like) quantum system, into which a photon with energy $\hbar\omega$ can be released during the spontaneous decay process. For free vacuum, it reduces to the *total density of states*:

$$\rho_0(\omega) = \frac{\omega^2}{\pi^2 c^3}, \quad (1.25)$$

which is position independent. In terms of the PLDOS, the Fermi Golden Rule reads as

$$\frac{\Gamma^{(\text{QED})}}{\Gamma_0^{(\text{QED})}} = \frac{\rho_{\mathbf{n}_{ab}}(\mathbf{r}_0, \omega_{ab})}{\rho_0(\omega_{ab})} \quad (1.26)$$

Hence when the emitter is placed in a structured environment, such as a resonant cavity where the density of final states is no longer given by

the free space photon density of states, the spontaneous emission rate is modified. This enhancement or inhibition of the spontaneous emission rate Γ compared to the free-space decay rate Γ_0 is also called the Purcell factor. In the case of a cavity, which can be characterized by a quality factor Q and volume V , the photon density of states is proportional to Q/V and is greatly enhanced for small cavities of high quality. It should be noted that in an inhomogeneous environment, Γ might well depend on the dipole orientation. Hence for an isotropic random emitter, such as a QD, the Purcell effect can then be used to privilege one polarization over others, obtaining a polarized dipole emitter. As will be shown in Chapter 2, this can be accomplished by using a well-chosen dielectric environment such as a slot-waveguide.

1.2.3.3 Single-photon source

Solid-state emitters providing single photons on-demand are an essential building block in photonic quantum technology, which involves applications such as quantum cryptography, quantum simulation, and random number generation. Currently, a diversity of material platforms is being considered as single-photon emitters, which include color centers or defects in crystalline hosts, carbon nanotubes, transition metal dichalcogenides, and epitaxial and colloidal semiconductor nanocrystals. Especially colloidal QDs are exceptional candidates because of their extensive design freedom, both at the level of nanocrystal synthesis and device integration, as well as their room-temperature operation. Room-temperature photon antibunching in the luminescence of single colloidal QDs was first reported for CdSe/ZnS core/shell QDs.^{28;29} Their single-photon emission is attributed to the highly efficient and non-radiative Auger recombination of multi-excitons,³⁰ enabling the triggered emission of single photons even when multi-excitons are generated by a high-intensity excitation pulse. One drawback of these dots is however that they show blinking, leading to an unpredictable succession of bright and dark periods. Several attempts have been made to suppress blinking by speeding up the radiative recombination (*e.g.* by alloyed interfaces) this however is detrimental for the Auger recombination, resulting in a loss of purity of single-photon emission. Another route is looking into new semiconductor materials with better optical properties. Recently our group demonstrated single-photon emission from InP/ZnS QDs, showing very little luminescence intermittency.³¹ The analysis of single-particle luminescence statistics places these InP/ZnSe QDs in the class of nearly blinking-free emitters, with emission stabilities comparable to state-of-the-art thick-shell and alloyed-interface CdSe/CdS QDs, but with improved single-photon purity.

1.3 Integrated photonics

It is clear that colloidal QDs are interesting materials, which can be used as the active material in both single-photon sources as well as coherent light sources such as lasers or incoherent broadband LEDs. The low cost of the QD synthesis and deposition methods, typically through non-vacuum techniques, already puts them at the forefront of diverse applications such as displays, lighting, solar cells and luminescent solar concentrators.^{32;33} Since QDs are obtained through a wet chemical synthesis, they are available for film formation as a colloidal dispersion, typically in apolar solvents such as toluene and hexane. As such, typical solution based deposition methods are applicable: dropcasting, doctor blading, inkjet printing, spincoating and Langmuir-blodgett deposition. The latter two were used and will be discussed in the next section. These two techniques in combination with lithography, allows to pattern the dots; another important advantage of QDs for integrated photonics. Finally, the most important deposition techniques and properties of other used materials in our integrated devices are briefly discussed.

1.3.1 QD deposition techniques

Spincoating is a straightforward technique to deposit thin films onto a substrate, allowing a uniform deposition over large areas. Usually a small amount of coating material is applied onto the center of the substrate. The substrate is then rotated at high speed in order to spread the coating material by centrifugal force. Both the QD concentration and spinspeed determine the final film thickness. When a thinner film is needed, it is preferred to dilute the QD dispersion in stead of going to higher spin-speeds, as to limit the amount of material used per spincoating. Spin-speeds between 1500 – 2000 rpm are used for spincoating colloidal QDs, going to a spin-speed lower than 1500 rpm generally results in non-uniform layers. As a rule of thumb, doubling the concentration will generally result in a doubling of the final layer thickness.

Langmuir-Blodgett (LB) deposition is a technique where one or more monolayers of QDs is deposited from the surface of a liquid onto a solid by immersing (or emersing) the solid substrate into (or from) the liquid. A monolayer is adsorbed homogeneously with each immersion or emersion step. It allows for a very accurate control of the layer thickness as formation of perfectly packed layers with monolayer precision on 2D and 3D substrates (*e.g.* photonic structures such as micron sized waveguides and resonators) is possible. Besides vertical deposition, also horizontal deposition or ‘stamping’

is possible, called Langmuir-Schaefer deposition.^{34;35}

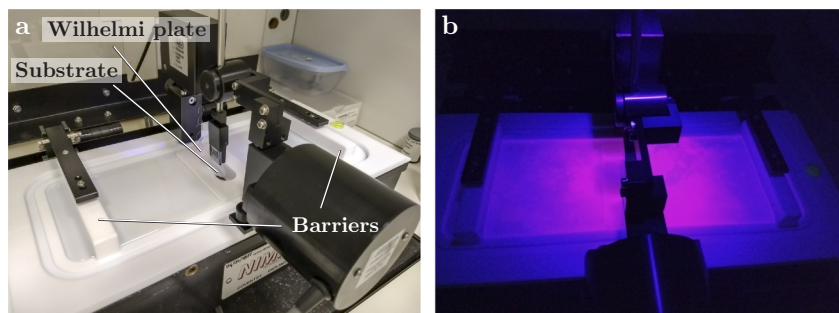


Figure 1.6: (a) LB deposition trough with a water surface, barriers to compress the layer, Wilhelmy plate for measuring the surface pressure and a vertical sample holder to pull the sample out of the water. (b) Colloidal QDs floating on the water surface, illuminated with UV-torch.

The setup for LB deposition is shown in Fig. 1.6a. It consists of a trough with a water surface, barriers to compress the layer, a Wilhelmy plate to continuously measure the surface pressure during compression and a vertical sample holder to pull and transfer the formed layer from the water surface onto the sample. When a drop of QDs in a volatile solvent is dropped on such a surface, the QDs spread to form close packed islands that float on the water surface due to their organic hydrophobic ligand shell. In Figure 1.6b these floating QDs are made visible by illuminating them with a UV-torch. Next, this layer is compressed by moving the two barriers towards each other. The change in surface pressure (so-called isotherm) is monitored in-situ to track the different phases of the QD layer: (a) gass phase, (b) liquid phase and finally (c) the solid phase. A typical surface pressure isotherm with the different phases is shown in Fig. 1.7. During the solid phase, when the islands are compressed into a continuous single monolayer, the substrate is extracted from the water resulting in a single monolayer on the substrate as illustrated in steps (d) and (e).

In order to have a high quality monolayer it is important that the self-assembly of the nanocrystals at the air-water interface is homogenous without any voids upon compression. The presence of these voids is mainly caused by impurities either present in the water sub-phase (*e.g.* dust) or the colloidal dispersion (*e.g.* free ligands). The first is avoided by working in a clean room environment and using high purity DI-water. While for

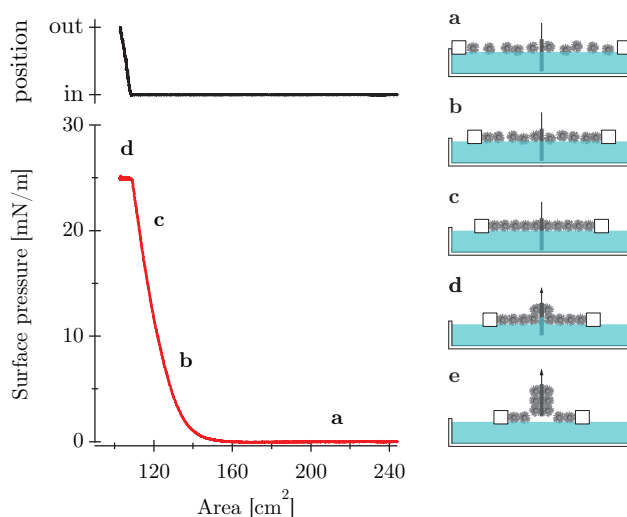


Figure 1.7: A typical isotherm is shown (red), relating surface pressure to the compressed area (or trough area). The different regimes are indicated (a) gaseous phase (b) liquid phase (c) solid phase (d)-(e) monolayer transfer. The black curve indicates the substrates position.

the latter additional purifying and washing steps can be used to avoid any free ligands. By adding some drops of acetonitrile (ACN) and subsequently centrifuging the dispersion, all QDs precipitate. The free ligands are left behind in the solvent (and are thrown away), while the QD precipitate is dispersed again in an apolar solvent. However, as the quality of the QD-layer is also determined by the quality of the ligand shell around the individual QDs, too many purification steps can lead to the stripping of ligands from the nanocrystal surface, deteriorating the layer quality. To restore/increase the ligand density, the QDs are heated to 50°C in the presence of excess ligands over a period of several hours. Afterwards additional purifying steps are of course needed again. Although the deposition technique is compatible with a large variety of QDs, deposition parameters such as the solvent, subphase, deposition pressure and extraction speed have to be optimised for each of them. Figure 1.8a-b shows scanning electron microscope (SEM) images of ‘flash’ CdSe/CdS QDs deposited on a silicon substrate. The first image is an example of a deposition where free ligands were present. Although the compression pressure was increased the original islands do not assemble into a monolayer but tend to collapse and start forming double layers. The QDs were purified and also butanol, in ratio (1:3), was added

to the QD dispersion to allow a better spreading on the water subphase. An optimised deposition pressure of 25 mN/m was chosen resulting in a homogenous monolayer of several square micron.

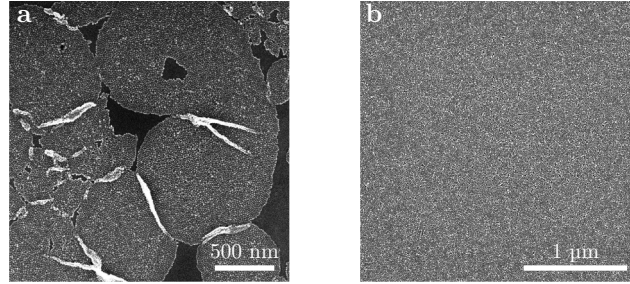


Figure 1.8: SEM images of a monolayer of ‘flash’ CdSe/CdS QDs deposited on Si substrate. (a) bad monolayer: voids, island formation and double layers, (b) uniform monolayer of several square μm .

1.3.2 Patterning of QD (mono)layers

The deterministic positioning of QD films is extremely relevant for both single-photon sources and improving light-matter interactions. Indeed, when the QDs could be deposited where the field intensity of the fundamental mode is highest, modal gain would improve drastically reducing the thresholds for stimulated emission and lasing. The patterning of colloidal QDs is either done by an etching or a lift-off procedure (see Figs. 1.9b and 1.9a). In both techniques the pattern is transferred to the QD (mono)layer by means of lithography. Depending on the resolution of the desired pattern, this can be either optical (μm -scale) or electron beam lithography (nm-scale). Etching can be done either by reactive ion etching (RIE), also called ‘dry’ etching, or wet etching. In case of wet etching, an $\text{HCl}/\text{H}_3\text{PO}_4$ mixture can be used.³⁶ For dry etching generally a gas mixture containing SF_6 is used.³⁷ The difficulty with patterning by etching is that the resist layer needs to be spincoated on top of the QD layer, which can be rough compared to normal dielectric substrates. In addition the etching is more prone to leave QD-residue behind, especially in the case of dry etching (see Section 3.2). Hence, the lift-off technique is often preferred. Using a thinned down resist and an optimized lift-off process we are able to achieve both nanoscale (see Fig. 1.10a-c) and single-dot patterning (see Fig. 1.10d), with a record yield of 40% for single-dot positioning.³⁸

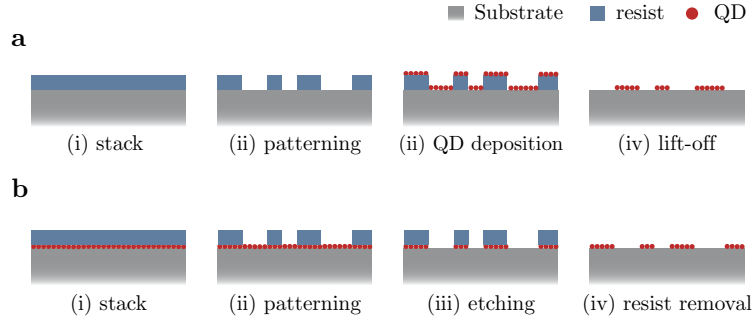


Figure 1.9: Schematic illustration of the two main methods for patterning QD layers: (a) lift-off and (b) etching.

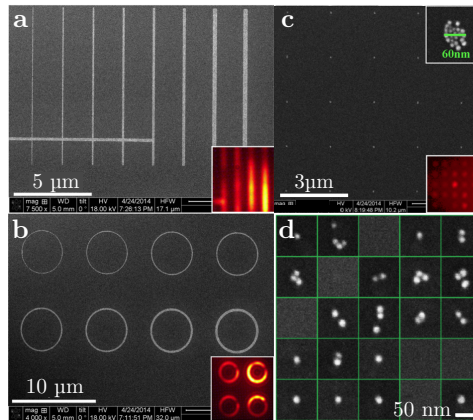


Figure 1.10: SEM images of nanoscale patterned QD films with (a) lines, (b) rings with different widths and (c) dots. The insets at the right lower corners show the respective micro-PL of the patterned shapes. (d) Single-dot patterning: SEM images of 5 x 5 dot patterns containing between 0 – 4 QDs. Adapted from reference³⁸.

1.3.3 QDs in integrated photonic devices

Plasma-enhanced chemical vapour deposition (PECVD) is a relatively fast deposition technique for growing dielectric films on a substrate. The deposition is done at relatively low temperatures (less than 500°C) and allows to grow large film thicknesses (up to 1 μm) in a single run. In the case of silicon nitride, a mixture of silane (SiH₄), ammonia (NH₃) and hydrogen

(H_2) is pumped into the reaction chamber with two parallel electrodes. By applying an alternating current a plasma is formed, inducing a chemical reaction between the gasses resulting in SiN_x being formed at the substrate's interface. The exact composition of the deposited layer depends on temperature, the ratio of flow rates, the RF power and addition of hydrogen gas. The silicon nitride layers deposited in this work use an optimized PECVD process at a temperature of $270^\circ C - 120^\circ C$, hereafter called HT-SiN and LT-SiN respectively. In general a high plasma frequency (HF) results in a more reactive process where a denser layer is formed and concomitant higher refractive index. On the other hand this more reactive process introduces more defects and hence higher optical losses. Low frequency deposited (LF) SiN in general also shows significantly less fluorescence than HF SiN. The $n - \kappa$ spectra of SiN_x and other used dielectrics (Si and SiO_x) are shown in Figs. 1.12a-d. These spectra are used in the FDTD-simulations of the following chapters.

Even though, QDs can be deposited and patterned directly on top of optical components, incorporating them into the bulk of the optical component by embedding dramatically improves the modal overlap and the coupling efficiency. A typical embedding process involves the creation of a $SiN_x/QD/SiN_x$ sandwich, where care is taken during deposition to ensure (a) maximum optical quality of the nitride layers and (b) minimum material damage to the QDs. To this end, the bottom layer is typically deposited at $270^\circ C$, whereas the top layer is deposited at a relatively low temperature of $120^\circ C$ to avoid damage to the QD layer underneath. The deposition at this lower temperature allows to maximally preserve the luminescence of the QDs. Another crucial aspect for the deposition of the top nitride layer is to ensure good contact between the QD-layer, which is a 'soft material', and the nitride capping. Especially for spincoated layers, which are thicker and less smooth than monolayers, the capping layer tends to crack and wrinkle as shown in Figs. 1.11a and 1.11b. To avoid this, a mixed frequency PECVD process is developed that ensures a smooth silicon nitride layer with good adhesion, as shown in Fig. 1.11c.

Finally, after embedding the QDs in a silicon nitride matrix, the initial planar structure needs to be patterned into a waveguide or cavity. Apart from material loss induced by the absorption and scattering in the nitride and/or QD film, modal losses of optical components are often limited by sidewall roughness after the etching step. An optimised etching process was developed to etch stacks of HT/LT- SiN_x with a gas mixture of CF_4/H_2 (80 : 3) where the role of H_2 is to form a polymer inhibitor on lateral side-

walls which protects these from further damage.³⁷ When no specific localisation of QDs within an optical component is required the QD-patterning step can be skipped and one etches directly through the hybrid nitride/QD stack. In this case some SF_6 is added to the gas mixture ($\text{CF}_4/\text{H}_2/\text{SF}_6$ 80:3:7). This approach is more straightforward but in general leads to more roughness and losses.

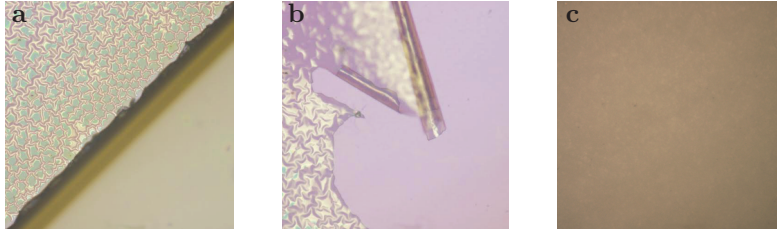


Figure 1.11: Silicon nitride deposited on top of spincoated QD layer using (a)-(b) LF and (c) MF.

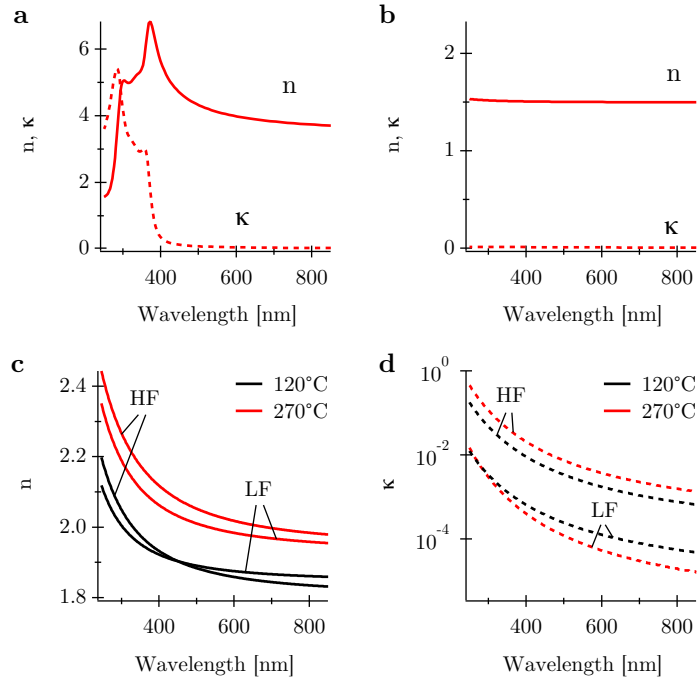


Figure 1.12: $n - \kappa$ spectra of (a) Si ,³⁹ (b) SiO_x ³⁹ and (c)-(d) SiN_x measured using ellipsometry.

The nanopatch-cavities in Chapter 3 also include thin Au-layers. For the deposition of thin metal films, electron beam physical vapor deposition (EBPVD) is used. It is a technique where an electron beam bombards a target anode, causing atoms from the target to transform into the gaseous phase, followed by precipitation into solid form onto the substrate. The $n - \kappa$ spectra of Au are shown in Fig. 1.13 and are used in the FDTD-simulations of Chapter 3.

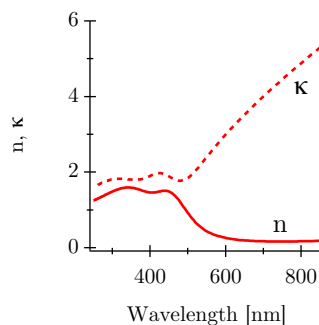


Figure 1.13: $n - \kappa$ spectra of Au⁴⁰ used in FDTD simulations.

1.4 Transient absorption spectroscopy

Many processes in solid state materials, such as photon absorption and emission, Auger recombination, etc. happen on a timescales ranging from tens of femtoseconds to a few nanoseconds. The shorter the detection time, the better the resolution. This leads to the idea that femto-second laser based spectroscopy offers better resolution than longer-laser pulses based spectroscopy. The advent of ultrafast laser systems that produce pulses with femtosecond duration opened up a new area of research and enabled investigation of these photophysical processes in real time. Transient absorption spectroscopy (TAS) encompasses a powerful set of techniques for probing and characterising the electronic and structural properties of short-lived excited states (transient states). In a typical experimental set up, a pump pulse excites the sample after which, a delayed probe pulse strikes the sample. By monitoring the latter these transient states are accessed upon absorption of photons, giving information of these processes as a function of wavelength and time. Here, we provide a basic description of the ultrafast transient absorption technique, setup and the collection of transient absorption data.

1.4.1 TAS technique and setup

TAS, also called white light pump-probe spectroscopy, is a technique where a sample, *e.g.* a dispersion of colloidal QDs, is pumped with an ultrashort laser pulse after which the change in absorbance ΔA is measured by a time-delayed pulse as function of wavelength or energy. In practice, samples are excited using 110 fs pulses at $\lambda_p = 350 - 1500$ nm, created from the 800 nm fundamental (Spitfire Ace, Spectra Physics) through non-linear conversion in an optical parametric amplifier (OPA) (Light Conversion TOPAS). Probe pulses are generated in a thin CaF_2 crystal using 10% of the 800 nm fundamental. The pulses are delayed relative to the pump using a delay stage with maximum delay of 6 ns. The probe spectrum in our experiments covers the UV-VIS window from 350 nm up to 750 nm. A picture of the used TAS setup and schematic are shown in Figs. 1.14 and 1.15.

The quantum dots are dispersed in an optically transparent solvent (*e.g.* toluene) to achieve optical densities of ca. 0.1 at the first exciton transition. During the experiment the sample is continuously stirred to avoid charging or photo-degradation. The average number of absorbed photons per QD (or equivalently created excitons) at time zero, noted as $\langle N \rangle$, can be calculated from the photon flux J_{ph} , the cuvette length L and the QD's absorption cross section at the pump wavelength $\sigma_{abs}(\lambda_p)$ (see Eq. (1.15)):

$$\langle N \rangle = J_{ph} \sigma_{abs}(\lambda_p) \frac{1 - e^{-A_0(\lambda_p)L}}{A_0(\lambda_p)L} \quad (1.27)$$

The additional factor corrects for variation of the pump fluence along the pump beam path length. The photon flux is calculated using

$$J_{ph} = \frac{P}{E_{ph}} \frac{1}{0.5 \text{ kHz } A_{\text{beam}}} \quad (1.28)$$

with P the pump power, $E_{ph} = \hbar\omega$ the energy of a photon, and A_{beam} the beam area. The latter is obtained through a Thorlabs CCD beam profiler, and defined as $A_{\text{beam}} = 2\pi \sigma_x \sigma_y$ where σ_i is the standard deviation in the $i = x, y$ direction. The repetition rate of the pump pulses is 0.5 kHz after the chopper.

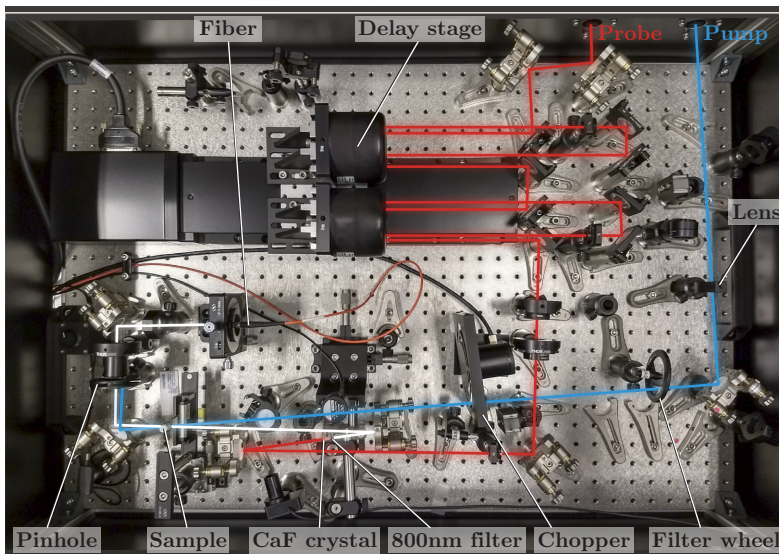


Figure 1.14: Picture of TAS setup with the pump (blue) and probe (white) beam. The latter is created by pumping a CaF_2 crystal with the 800 nm fundamental (red line) which is sent through a delay stage. The intensity of the pump can be changed using a ND-wheel. The pump and white light probe cross at the sample position. Next, the white light probe is collected with a fiber-to-CCD configuration.

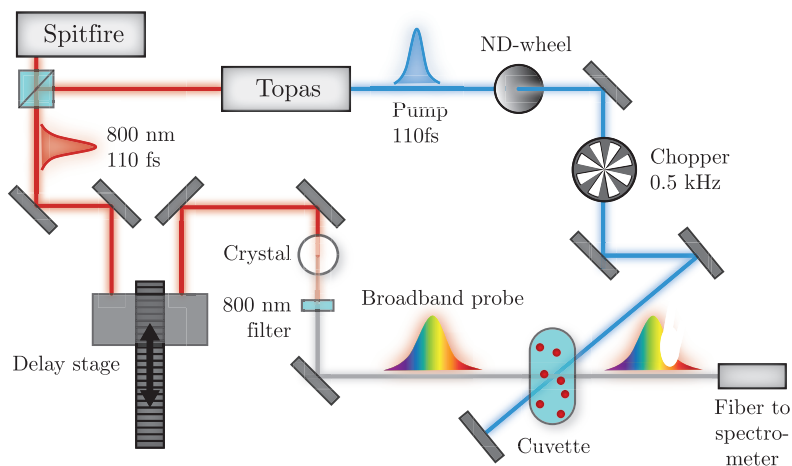


Figure 1.15: Schematic of TAS setup shown in Figure 1.14

1.4.2 Ultra-fast properties

The absorbance of a QD ensemble changes due to the presence of excitons created by the pump pulse. It is exactly this change that is measured using TAS. The differential absorbance ΔA has three main contributions:

Interband Bleach: When carriers are created upon excitation, they will occupy the empty spaces on discrete energy levels. As there is only a finite number of spaces available on an energy level, this filling results in the blocking of optical transitions between those levels. This translates in a reduction of the absorbance, also called bleach.

Intraband Absorption: Similarly as the absorption of a photon can promote an electron from the valence to the conduction band, the promotion of electrons/holes within the same band to a higher energy level is also possible. This phenomenon can only occur when an exciton is already present.

Spectral Shifts: The presence of (unbalanced) electrical charges implies the presence of electric fields. The latter can shift the linear absorbance spectrum either to higher or lower energy depending on the details of the nanostructure (so-called Stark effect).

Also smaller effects can play a role, such as a change in the oscillator strength of an optical transitions. It is the combination of all these effect that result in the differential absorbance that is measured in a TAS-experiment. The experimentally accessible linear absorbance A_0 and differential absorbance ΔA combine to the actual non-linear absorbance: $A = \Delta A + A_0$; the absorbance of the sample after photoexcitation. Considering the simple case of a g -fold degenerate valence and conduction band edge and an exciton population below g , we can write the non-linear absorbance A as:⁴¹

$$A(E) = \sum_{N=0}^g P(N) \left\{ \left(1 - \frac{N}{g} \right) A_0(E - (N-1)\delta E) - \frac{N}{g} A_0(E - N\delta E) + N A_{IB}(E) \right\} \quad (1.29)$$

with $P(N)$ the probability to have N excitons in a nanocrystal ensemble with average number of excitons $\langle N \rangle$. This can be described by a Poisson distribution

$$P(N) = \frac{\langle N \rangle^N e^{-\langle N \rangle}}{N!} \quad (1.30)$$

The first term in Equation (1.29) accounts for the reduction in absorbance, called bleach, while the second terms accounts for stimulated emission, both weighed with the relative occupations of the valence and conduction band. The third term accounts for intraband absorption and δE accounts for a possible spectral shift, which can be either positive or negative. The simple case of $g = 2$ (with $\delta E = 0$) is illustrated in Figure 1.16.

We can distinguish three regimes:

- (a) $A > 0$: when $N = 0$ there is only absorbance and the net absorbance is positive.
- (b) $A = 0$: when $N = 1$ stimulated emission (grey dashed line) and absorption (black dashed line) compensate each other, this is called ‘optical transparency’.
- (c) $A < 0$: when $N = 2$ stimulated emission dominates over absorption resulting in a negative A . In this situation net optical gain is achieved.

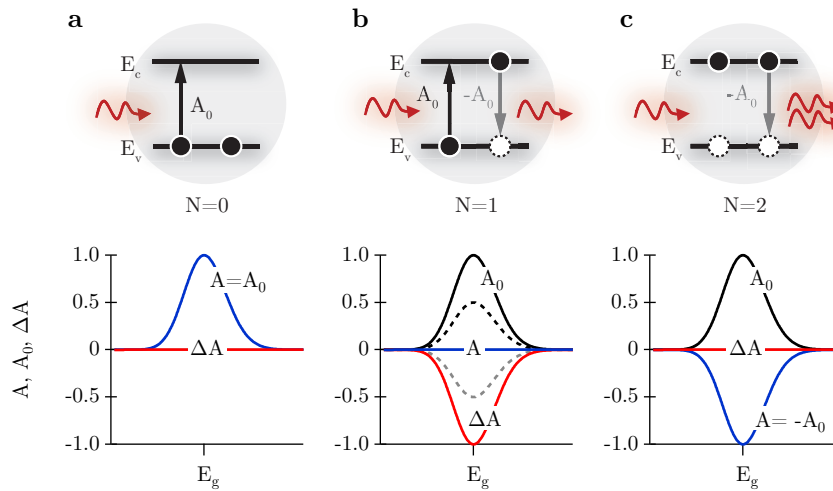


Figure 1.16: Simple case of $g = 2$ (and $\delta E = 0$). (top) Schematic of the energy levels and (bottom) corresponding A (blue) and ΔA (red) for the different regimes: (a) net absorption $A > 0$, (b) transparency $A = 0$ and (c) net gain $A < 0$.

1.5 Thesis layout

In this thesis we aimed at using colloidal quantum dots as the active material for the development of integrated light sources, specifically in the visible light range. Following the excellent luminescent properties of colloidal QDs both in the single-photon and optical gain regime, we have explored both the development of single-photon sources and integrated lasers on the silicon nitride platform. In this first chapter we introduced colloidal QDs and discussing the properties relevant for single-photon emission and/or optical gain, followed by a some background on their heterogenous integration on the silicon nitride platform.

The next two chapters focus on colloidal QDs as single-photon emitters and study the possibility to integrate them directly on a photonic chip. The coupling of single-photon emitters to dielectric cavities or plasmonic cavities/antennas has been demonstrated using a variety of physical systems with the aim of making the source brighter and more directive. A major challenge consists in efficiently extracting their emission into a single guided mode. This is the subject of Chapter 2, where we used 3D finite-difference time-domain simulations to investigate the single-photon emission from dipole-like nanometer-sized inclusions embedded into different silicon nitride photonic nanowire waveguide designs. With these simulations we elucidating the effect of the geometry on the emission lifetime and the polarization of the emitted single photon. In Chapter 3 we demonstrate the fabrication and characterisation of on-chip vertically-emitting SiN_x/Au nanopatch cavities containing a monolayer of colloidal quantum dots. The fabrication process is based on electron-beam lithography and allows to deterministically position both the cavity and the emitters within the cavity with an accuracy of 10 nm. The Purcell enhancement of the spontaneous emission of the quantum dots is studied theoretically and experimentally. This work paves the way towards scalable fabrication of bright and directive single-photon sources.

CQDs have emerged as a most attractive optical gain medium in recent years. They offer a broad gain spectrum that can be readily adjusted by exploiting size-dependent quantum confinement, a specific choice of QD material or the judicious formation of heterostructured core/shell QDs. Together with their suitability for solution-based processing, this makes them a most versatile gain medium for photonic integrated circuits. CdSe/CdS core/shell CQDs in particular have shown amplified spontaneous emission (ASE) and lasing under femtosecond and nanosecond pumping. However,

to fully assess their potential for micro- and nanophotonics, a quantitative understanding of their gain characteristics is needed. This is the subject of Chapter 4, where we introduce the concept of material gain and show that it can be conveniently measured using ultrafast transient absorption spectroscopy on colloidal dispersions. Material gain is a key parameter that makes it possible to compare different QD samples on the same footing. We focus on core/shell CdSe/CdS QDs and elucidate the effect of the QD's morphology on gain properties such as material gain, gain threshold and inversion lifetime. Especially the inversion lifetime has important implications for continuous-wave (CW)-pumped lasers.

In the Chapter 5, we study gain in $\text{SiN}_x/\text{QD}/\text{SiN}_x$ strip waveguides and show that the experimental modal gain can be interpreted as the product of the material gain of the QDs, their volume fraction and the overlap between the optical mode and the QD layer. This exemplifies the benefits of material gain as a design parameter for the simulation and optimization of future QD-based amplifiers and microlasers. Following the characterisation of the gain properties of CdSe/CdS QDs in Chapter 4, a 'best' sample was chosen to be integrated in a distributed feedback (DFB)-laser. The fabricated lasers are studied and characterised under nano-second laser pumping. The results showcase the advantages of colloidal QDs as an enabling gain material for integrated SiN-photonics. We end with a general conclusion and outlook on the potential of colloidal QDs as an active material for on-chip integrated light sources.

1.6 Publications

List of Articles

1. S. Bisschop, P. Geiregat, L. Elsinger, E. Drijvers, D. Van Thourhout, Z. Hens, and E. Brainis, "Fabrication and characterization of SiN_x/Au cavities with colloidal nanocrystals," *Optics Express*, vol. 26, no. 5, pp. 6046–6055, 2018.
2. S. Bisschop, A. Guille, D. Van Thourhout, Z. Hens, and E. Brainis, "Broadband enhancement of single photon emission and polarization dependent coupling in silicon nitride waveguides," *Optics Express*, vol. 23, no. 11, pp. 13713–13724, 2015.
3. Y. Zhu, W. Xie, S. Bisschop, T. Aubert, E. Brainis, P. Geiregat, Z. Hens, and D. Van Thourhout, "On-chip single-mode distributed

- feedback colloidal quantum dot laser under nanosecond pumping,” *ACS photonics*, vol. 4, no. 10, pp. 2446–2452, 2017.
4. W. Xie, Y. Zhu, S. Bisschop, T. Aubert, Z. Hens, D. Van Thourhout, and P. Geiregat, “Colloidal quantum dots enabling coherent light sources for integrated silicon-nitride photonics,” *IEEE journal of selected topics in quantum electronics*, vol. 23, no. 5, p. 12, 2017.
 5. W. Xie, T. Stöferle, G. Rainò, T. Aubert, S. Bisschop, Y. Zhu, R. F. Mahrt, P. Geiregat, E. Brainis, Z. Hens, and D. Van Thourhout, “On-chip integrated quantum-dot-silicon-nitride microdisk lasers,” *Advanced Materials*, vol. 29, no. 16, 2017.
 6. W. Xie, R. F. Gomes Pinto Fernandes, T. Aubert, S. Bisschop, Y. Zhu, Z. Hens, E. Brainis, and D. Van Thourhout, “Nanoscale and single-dot patterning of colloidal quantum dots,” *Nano Letters*, vol. 15, no. 11, pp. 7481–7487, 2015.

List of Conference contributions

1. S. Bisschop, P. Geiregat, T. Aubert, D. Van Thourhout, E. Brainis, Z. Hens, “A quantitative study of the material gain in colloidal core/shell Quantum Dots,” in *E-MRS Spring meeting, LT6YT*, 2017
2. Y. Zhu, W. Xie, P. Geiregat, S. Bisschop, T. Aubert, E. Brainis, Z. Hens, and D. Van Thourhout, “On-chip-threshold silicon nitride distributed feedback colloidal quantum dot laser,” in *CLEO 2017*, pp. paper JW2A.126:1–paper JW2A.126:2, 2017.
3. S. Bisschop, P. Geiregat, Z. Hens, D. Van Thourhout, and E. Brainis, “Fabrication and characterization of SiN_x/Au nanopatch cavities with colloidal nanocrystals,” in *CLEO:2016 : Laser Science to Photonic Applications*, paper FTu4B.6, OSA, 2016.
4. S. Bisschop, P. Geiregat, Y. Zhu, W. Xie, T. Aubert, E. Brainis, D. Van Thourhout, and Z. Hens, “Optical gain with colloidal quantum dots : from material photo-physics to integrated devices,” in *Proceedings Symposium IEEE Photonics Society Benelux* pp. 239–242, 2016.
5. Y. Zhu, W. Xie, P. Geiregat, S. Bisschop, T. Aubert, E. Brainis, Z. Hens, and D. Van Thourhout, “Hybrid colloidal quantum dot silicon nitride waveguide gain measurement based on variable stripe length method,” in *OSA Technical Digest*, p. 2, The Optical Society (OSA), 2016.

6. S. Bisschop, J. Ciers, A. Guille, P. Geiregat, E. Brainis, Z. Hens, and D. Van Thourhout, “Subwavelength nanopatch sin/au nanocavities with colloidal nanocrystals,” in *2015 European Conference on Lasers and Electro-Optics : European Quantum Electronics Conference, Abstracts*, Optical Society of America, 2015.
7. S. Bisschop, A. Guille, E. Brainis, D. Van Thourhout, and Z. Hens, “Broadband light enhancement and polarization dependent coupling in si₃n₄ slot waveguides,” in *Quantum Optics, 21st Central European workshop, Abstracts*, 2014.
8. S. Bisschop, Y. Zhu, W. Xie, A. Guille, Z. Hens, D. Van Thourhout, and E. Brainis, “Progress towards on-chip single photon sources based on colloidal quantum dots in silicon nitride devices,” in *Conference on Lasers and Electro-Optics*, p. 2, Optical Society of America (OSA), 2014.

References

- [1] Q. Liu, X. Tu, K. W. Kim, J. S. Kee, Y. Shin, K. Han, Y.-J. Yoon, G.-Q. Lo, and M. K. Park, “Highly sensitive mach-zehnder interferometer biosensor based on silicon nitride slot waveguide,” *Sensors and Actuators B: Chemical*, vol. 188, no. Supplement C, pp. 681 – 688, 2013.
- [2] E. Ryckeboer, X. Nie, A. Z. Subramanian, D. Martens, P. Bienstman, S. Clemmen, S. Severi, R. Jansen, G. Roelkens, and R. Baets, “Cmos-compatible silicon nitride spectrometers for lab-on-a-chip spectral sensing,” *Proc.SPIE*, vol. 9891, pp. 9891 – 9891 – 9, 2016.
- [3] S. Romero-Garcia, F. Merget, F. Zhong, H. Finkelstein, and J. Witzens, “Silicon nitride cmos-compatible platform for integrated photonics applications at visible wavelengths,” *Opt. Express*, vol. 21, pp. 14036–14046, Jun 2013.
- [4] M.-C. Tien, J. F. Bauters, M. J. R. Heck, D. T. Spencer, D. J. Blumenthal, and J. E. Bowers, “Ultra-high quality factor planar si₃n₄ ring resonators on si substrates,” *Opt. Express*, vol. 19, pp. 13551–13556, Jul 2011.
- [5] Y. Shirasaki, G. Supran, M. Bawendi, and V. Bulovic, “Emergence of colloidal quantum-dot light-emitting technologies,” *Nature Photonics*, 2013.
- [6] G. Konstantatos, I. Howard, A. Fischer, S. Hoogland, J. Clifford, E. Klem, L. Levina, and E. Sargent, “Ultrasensitive solution-cast quantum dot photodetectors,” *Nature*, 2006.
- [7] B. Min, S. Kim, K. Okamoto, L. Yang, A. Scherer, H. Atwater, and K. Vahala, “Ultralow threshold on-chip microcavity nanocrystal quantum dot lasers,” *Applied Physics Letters*, 2006.
- [8] B. De Geyter, K. Komorowska, E. Brainis, P. Emplit, P. Geiregat, A. Hassinen, Z. Hens, and D. Van Thourhout, “From fabrication to mode mapping in silicon nitride microdisks with embedded colloidal quantum dots,” *Applied Physics Letters*, vol. 101, no. 16, p. 161101, 2012.
- [9] W. Xie, T. Stöferle, G. Rainò, T. Aubert, S. Bisschop, Y. Zhu, R. F. Mahrt, P. Geiregat, E. Brainis, Z. Hens, and D. Van Thourhout, “On-chip integrated quantum-dot silicon-nitride microdisk lasers,” *Advanced Materials*, vol. 29, no. 16, pp. 1604866–n/a, 2017. 1604866.

- [10] G. Pucker, M. Ghulinyan, A. Pitanti, M. Xie, D. Navarro-Urrios, A. Lui, L. Pavesi, and A. Simoni, “Silicon quantum dots in microdisk resonators: whispering-gallery modes, stress-induced Q-factor tuning and enhancement,” *Proceedings SPIE*, 2009.
- [11] F. Pisanello, L. Martiradonna, A. Quattieri, T. Stomeo, M. Grande, P. Pompa, R. Cingolani, A. Bramati, and M. D. Vittorio, “Silicon nitride PhC nanocavities as versatile platform for visible spectral range devices,” *Photonics and Nanostructures - Fundamentals and Applications*, 2012.
- [12] M. Barth, J. Stingl, N. Nüsse, B. Löchel, and O. Benson, “Controlled coupling of nanoparticles to photonic crystal cavities,” *Proceedings SPIE*, 2009.
- [13] C. B. Murray, D. J. Norris, and M. G. Bawendi, “Synthesis and characterization of nearly monodisperse cde (e = sulfur, selenium, tellurium) semiconductor nanocrystallites,” *Journal of the American Chemical Society*, vol. 115, no. 19, pp. 8706–8715, 1993.
- [14] P. D. Cozzoli, T. Pellegrino, and L. Manna, “Synthesis, properties and perspectives of hybrid nanocrystal structures,” *Chem. Soc. Rev.*, vol. 35, pp. 1195–1208, 2006.
- [15] A. Rogach, D. Talapin, E. Shevchenko, A. Kornowski, M. Haase, and H. Weller, “Organization of matter on different size scales: Monodisperse nanocrystals and their superstructures,” *Advanced Functional Materials*, vol. 12, no. 10, pp. 653–664, 2002.
- [16] X. Peng, “An essay on synthetic chemistry of colloidal nanocrystals,” *Nano Research*, vol. 2, pp. 425–447, June 2009.
- [17] M. A. Hines and P. Guyot-Sionnest, “Synthesis and characterization of strongly luminescing zns-capped cdse nanocrystals,” *The Journal of Physical Chemistry*, vol. 100, no. 2, pp. 468–471, 1996.
- [18] M. Cirillo, T. Aubert, R. Gomes, R. Van Deun, P. Emplit, A. Biermann, H. Lange, C. Thomsen, E. Brainis, and Z. Hens, ““flash” synthesis of cdse/cds core-shell quantum dots,” *Chemistry of Materials*, vol. 26, no. 2, pp. 1154–1160, 2014.
- [19] S. Buckley, K. Rivoire, and J. Vuckovic, “Engineered quantum dot single-photon sources,” *Reports on Progress in Physics*, vol. 75, no. 12, p. 126503, 2012.

- [20] P. S. Parfenov, A. P. Litvin, A. V. Baranov, E. V. Ushakova, A. V. Fedorov, A. V. Prudnikov, and M. V. Artemyev, "Measurement of the luminescence decay times of pbs quantum dots in the near-ir spectral range," *Optics and Spectroscopy*, vol. 112, pp. 868–873, Jun 2012.
- [21] L. E. Brus, "Electron-electron and electron-hole interactions in small semiconductor crystallites: The size dependence of the lowest excited electronic state," *The Journal of Chemical Physics*, vol. 80, no. 9, pp. 4403–4409, 1984.
- [22] D. V. Talapin, A. L. Rogach, A. Kornowski, M. Haase, and H. Weller, "Highly luminescent monodisperse cdse and cdse/zns nanocrystals synthesized in a hexadecylamine-trioctylphosphine oxide-trioctylphosphine mixture," *Nano Letters*, vol. 1, no. 4, pp. 207–211, 2001.
- [23] Z. Hens and I. Moreels, "Light Absorption by Colloidal Semiconductor Quantum Dots," *J. Mat. Chem.*, vol. 22, no. 21, pp. 10406–10415, 2012.
- [24] A. W. Achtstein, A. Antanovich, A. Prudnikau, R. Scott, U. Woggon, and M. Artemyev, "Linear absorption in cdse nanoplates: Thickness and lateral size dependency of the intrinsic absorption," *The Journal of Physical Chemistry C*, vol. 119, no. 34, pp. 20156–20161, 2015.
- [25] A. E. Neeves and M. H. Birnboim, "Composite structures for the enhancement of nonlinear-optical susceptibility," *J. Opt. Soc. Am. B*, vol. 6, pp. 787–796, Apr 1989.
- [26] L. Novotny and B. Hecht, *Principles of Nano-Optics*. Cambridge University Press, 2006.
- [27] E. M. Purcell, "Spontaneous emission probabilities at radio frequencies," *Physical Review*, vol. 69, pp. 681+, 1946.
- [28] B. Lounis, H. Bechtel, D. Gerion, P. Alivisatos, and W. Moerner, "Photon antibunching in single cdse/zns quantum dot fluorescence," *Chemical Physics Letters*, vol. 329, no. 5, pp. 399 – 404, 2000.
- [29] P. Michler, A. Imamoglu, M. D. Mason, P. J. Carson, G. F. Strouse, and S. K. Buratto, "Quantum correlation among photons from a single quantum dot at room temperature," *Nature*, vol. 406, p. 968, aug 2000.
- [30] M. De Vittorio, F. Pisanello, L. Martiradonna, A. Quattieri, T. Stomeo, A. Bramati, and R. Cingolani, "Recent advances on single photon sources based on single colloidal nanocrystals," *Opto-Electronics Review*, vol. 18, p. 1, Dec 2009.

- [31] V. Chandrasekaran, M. D. Tessier, D. Dupont, P. Geiregat, Z. Hens, and E. Brainis, “Nearly blinking-free, high-purity single-photon emission by colloidal inp/znse quantum dots,” *Nano Letters*, vol. 17, no. 10, pp. 6104–6109, 2017.
- [32] Y. Shirasaki, G. J. Supran, M. G. Bawendi, and V. Bulović, “Emergence of colloidal quantum-dot light-emitting technologies,” *Nature Photonics*, vol. 7, p. 13, dec 2012.
- [33] F. Meinardi, H. McDaniel, F. Carulli, A. Colombo, K. A. Velizhanin, N. S. Makarov, R. Simonutti, V. I. Klimov, and S. Brovelli, “Highly efficient large-area colourless luminescent solar concentrators using heavy-metal-free colloidal quantum dots,” *Nature Nanotechnology*, vol. 10, p. 878, aug 2015.
- [34] K. Lambert, R. K. Capek, M. I. Bodnarchuk, M. V. Kovalenko, D. Van Thourhout, W. Heiss, and Z. Hens, “Langmuir-schaefer deposition of quantum dot multilayers,” *Langmuir*, vol. 26, no. 11, pp. 7732–7736, 2010.
- [35] V. Santhanam and R. P. Andres, “Microcontact printing of uniform nanoparticle arrays,” *Nano Letters*, vol. 4, no. 1, pp. 41–44, 2004.
- [36] C. Hu, T. Aubert, Y. Justo Zarraguiños, S. Flamée, M. Cirillo, A. Gassenq, O. Drobchak, F. Beunis, G. Roelkens, and Z. Hens, “The micropatterning of layers of colloidal quantum dots with inorganic ligands using selective wet etching,” *Nanotechnology*, vol. 25, no. 17, p. 11, 2014.
- [37] W. Xie, Y. Zhu, T. Aubert, S. Verstuyft, Z. Hens, and D. V. Thourhout, “Low-loss silicon nitride waveguide hybridly integrated with colloidal quantum dots,” *Opt. Express*, vol. 23, pp. 12152–12160, May 2015.
- [38] W. Xie, R. Gomes, T. Aubert, S. Bisschop, Y. Zhu, Z. Hens, E. Brainis, and D. Van Thourhout, “Nanoscale and single-dot patterning of colloidal quantum dots,” *Nano Letters*, vol. 15, no. 11, pp. 7481–7487, 2015.
- [39] E. Palik, *Handbook of Optical Constants of Solids*. No. v. 4 in Handbook of Optical Constants of Solids, Academic Press, 1998.
- [40] P. B. Johnson and R. W. Christy, “Optical constants of the noble metals,” *Phys. Rev. B*, vol. 6, pp. 4370–4379, Dec 1972.
- [41] V. I. Klimov, *Nanocrystal Quantum Dots*, vol. 187. CRC Press, 2010.

2

Broadband enhancement of single-photon emission and polarization dependent coupling in SiN waveguides

One of the challenges to have a triggered solid-state single-photon source on a photonic chip, is the efficiently extraction of their emission into a single guided mode. Using 3D finite-difference time-domain simulations, we investigate the single-photon emission from dipole-like inclusions embedded into different silicon nitride photonic nanowire waveguide designs, elucidating the effect of the geometry on the emission lifetime and the polarization of the emitted single photon.

2.1 Introduction

Single-photon (SP) sources are important for a number of optical quantum information processing applications such as quantum computing,¹⁻³ quantum cryptography,⁴⁻⁶ and random number generation.⁷ In these applications, the photon wave function is processed by performing operations such

as polarization rotations, phase shifts and path splitting/recombination in order to en- or decode information. In early demonstrations of quantum computing and quantum communication protocols, these operations were usually performed with table-top optical components,^{8;9} and later with fibre optics elements.^{10–12} These approaches offer high flexibility but suffer from thermal and mechanical instabilities that hinder their scalability. Complex optical circuits are best realized using integrated photonic devices on a micro-chip. Many recent experiments successfully validated this approach by performing quantum optics experiments with photons propagating in integrated photonic circuits.^{13–16}

In this chapter, we study the possibility to integrate triggered solid-state SP emitters *directly* on a photonic chip. A major challenge consists in efficiently extracting their emission into a single guided mode. This is seen by many as a stumbling block precluding their usage in practical implementations. In 2010, a record photon extraction efficiency of 72% was first demonstrated by embedding the SP emitter into a tapered photonic nanowire.^{17–19} Following this approach, we consider different source designs in which the SP emitter is embedded into a photonic nanowire *waveguide*. This contrasts with the traditional approach consisting in placing the emitter in a high Q/V cavity, a method that is only efficient for very narrowband emitters such as epitaxially grown quantum dots at cryogenic temperatures. A good polarization control is key to most applications, including linear quantum computing and quantum cryptography. As shown in this work, efficient, directive, and broadband SP sources with well defined polarization states can be engineered.

We specifically investigate photonic chips made of silicon nitride (SiN_x) devices. Silicon nitride is an amorphous material that has a larger refractive index than silica ($n = 2$) and is highly transparent in both visible and near-infrared ranges. In addition, SiN_x devices and circuits can be realized on a silicon-on-insulator chip using standard complementary metal oxide semiconductor (CMOS) compatible processing technologies. This technology is suitable for developing a universal platform for quantum optics and quantum information processing applications in conjunction with many common solid-state emitters. It offers the possibility to embed alien solid-state inclusions acting as SP emitters directly inside the SiN_x host. Such inclusions can be colloidal quantum dots,^{20–23} nanoparticles containing a single color centre,^{24;25} or nanoparticles doped with a single ion.²⁶ This approach offers a very flexible route to future on-chip quantum optics experiments by separating the engineering of the emitter from the engineering of the photonic

circuit itself. In addition this approach would also be scalable since it allows many integrated SP sources and optical circuits to operate in parallel. In this prospect, colloidal quantum dots are of primary interest for proof-of-principal demonstrations because of their ability to emit single photons with a quantum yield as high as 80% at room temperatures^{20–23} and the fact that their embedding in SiN_x photonic structures has been recently achieved.²⁷

We investigate the SP emission from dipole-like nanometer-sized inclusions embedded in four types of SiN_x waveguiding structures as represented in Fig. 2.1. The first and simplest structure is a strip SiN_x waveguide on the top of a silicon oxide (SiO_x) substrate (Fig. 2.1a). A more elaborated design giving better performance consists in a slot waveguide in which a SiO_x layer is sandwiched between a lower and upper SiN_x layer (Fig. 2.1c). Using wet etching the substrate can be removed to create suspended strip and slot waveguides such as those represented in Fig. 2.1b and c, respectively. In each case, the SP emitter is positioned at the center of the structure. They are assumed to be effectively degenerate two-level systems with no preferential dipole moment orientation. Several experiments and theoretical works investigated light emission in such silicon stripe and slot structures.^{28–30} Here, we extend this work to realistic 3D SiN_x structures. More importantly, we elucidate the effect of the geometry on the emission lifetime and the polarization of the emitted single photons.

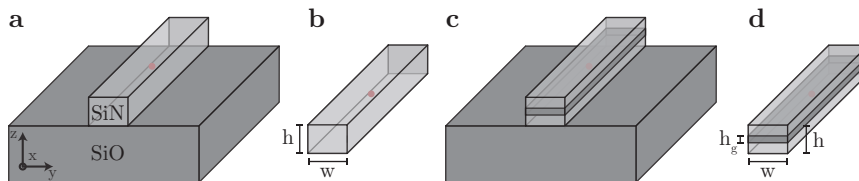


Figure 2.1: Layout of the simulated structures: (a) silicon nitride (SiN_x) strip waveguide on top of silicon oxide (SiO_x) substrate, (b) suspended SiN_x strip waveguide, (c) SiN_x slot waveguide on top of SiO_x substrate with SiO_x slot, (d) suspended SiN_x slot waveguide with SiO_x slot. The dipole is located at the center of the waveguide (red dot).

2.2 Classical dipole in inhomogeneous dielectric media

As is well known, both the spontaneous emission rate and the radiation pattern of the light emitted by a quantum dipole transition depend on the environment into which the light is emitted. The spontaneous emission rate from a non degenerate two-level dipole transition is given by Fermi's Golden Rule (see Section 1.2.3.2), where we see that the two main factors that influence the spontaneous emission rate are: (i) the modal field intensities at the position of the emitter and (ii) the spectral densities of the modes at the frequency of the emitting transition. The modes to take into account include guided modes as well as radiated modes. With a careful design of the waveguide one can modify both these factors by changing the number of guided modes (with specific polarization; transverse electric (TE) or transverse magnetic (TM)) and their mode profiles. The resulting spontaneous emission rate can be quite different from the rate Γ_0 that one would observe if the emitter was embedded in a homogeneous medium of index n . This enhancement (or inhibition) of the spontaneous emission rate due to the structuring of the photonic environment of the emitter is expressed by the *Purcell factor*:

$$F = \frac{\Gamma}{\Gamma_0(n)} \quad (2.1)$$

Consider now a classical dipole \mathbf{d} vibration at point \mathbf{r}_0 in the direction of the unit vector $\mathbf{n} = \mathbf{d}/|\mathbf{d}|$ with the same frequency ω_{ab} as the quantum dipole. The power radiated by this classical dipole is³¹

$$P = \frac{\omega_{ab}^3}{2 \epsilon_0 \epsilon_r c^2} |\mathbf{d}|^2 \{ \mathbf{n}^\dagger \Im [\mathcal{G}(\mathbf{r}_0, \mathbf{r}_0, \omega_{ab})] \mathbf{n} \}, \quad (2.2)$$

where ϵ_r is the relative permittivity of the material at the point \mathbf{r}_0 . Therefore the *classical* photon emission rate $\Gamma = P/(\hbar\omega_{ab})$ is

$$\Gamma = \frac{\omega_{ab}^2}{2 \hbar \epsilon_0 \epsilon_r c^2} |\mathbf{d}|^2 \{ \mathbf{n}^\dagger \Im [\mathcal{G}(\mathbf{r}_0, \mathbf{r}_0, \omega_{ab})] \mathbf{n} \}. \quad (2.3)$$

Clearly, if we look to the particular case of vacuum ($\epsilon_r = 1$), we see that the emission rate of a classical dipole \mathbf{d} differs from the emission rate of a quantum dipole \mathbf{d}_{ab} with the same frequency, amplitude and direction (see Appendix A, Eq. (A.15)). For instance, a classical dipole in free space would decay with the rate³¹

$$\Gamma_0 = \frac{n \omega_{ab}^3 |\mathbf{d}|^2}{12\pi \hbar \epsilon_0 c^3}, \quad (2.4)$$

with $n = \sqrt{\epsilon_r}$ the index of refraction. However the ratio Γ/Γ_0 is the same as in QED:

$$\frac{\Gamma^{(\text{QED})}}{\Gamma_0^{(\text{QED})}} = \frac{\Gamma}{\Gamma_0} = \frac{6\pi c}{\omega_{ab} n^3} \{ \mathbf{n}^\dagger \Im [\mathcal{G}(\mathbf{r}_0, \mathbf{r}_0, \omega_{ab})] \mathbf{n} \}. \quad (2.5)$$

Although the value $\Gamma_0^{(\text{QED})}$ requires an independent QED calculation, any departure from the decay in a homogeneous medium of index n due to nanostructuring of the environment, can be computed classically using numerical electromagnetic methods. The Purcell factor of the emitter can be written as:

$$F = \frac{P}{P_0(n)} \quad (2.6)$$

where P and P_0 are the classical powers radiated in the actual environment and homogeneous space of refractive index n respectively.

2.3 Light emission from randomly polarized dipoles

In the case of a randomly polarized SP emitter, the orientation of the dipole moment \mathbf{d} is random. Each orientation direction $i \in \{x, y, z\}$ can be seen as an independent de-excitation channel for the emitter. Therefore the total spontaneous emission rate is the sum of the spontaneous emission rates Γ_i corresponding to each possible orientation: $\Gamma = \sum_i \Gamma_i$. In a nanostructured environment such as a waveguide, the rates Γ_i will generally differ from each other and so will the Purcell factors $F_i = \Gamma_i/\Gamma_0$ associated to each possible vibration direction. The spontaneous emission enhancement is measured by the Purcell factor: $F = \Gamma/\Gamma_0 = \sum_i F_i$. When a single photon is emitted as a result of a de-excitation process, the probability that it is emitted by a dipole oscillating in the i -direction is

$$p_i = \frac{\Gamma_i}{\Gamma} = \frac{F_i}{F} \quad (2.7)$$

Waveguides can be engineered such that a dipole oscillating in a specific direction has a much larger Purcell factor than a dipole oscillating in any other two directions. In such a case, the photonic environment would turn an intrinsically unpolarized emitter into a polarized one, one with a p_i which is much larger than the p_i for the other directions.

To make an efficient directional SP source, the light from the SP emitter must mainly couple to the *guided* modes of the waveguide. Since photon emission into the guided and radiated modes can be seen as independent de-excitation channels, each spontaneous emission rate $\Gamma_i = \Gamma_i^g + \Gamma_i^r$ can be further split into an emission rate into the guided modes (Γ_i^g) and an emission rate into the radiated modes (Γ_i^r). The fraction of light that is emitted by an i -polarized dipole into the guided modes of the waveguiding structure, is equal to $f_i = \Gamma_i^g/\Gamma_i$. For a randomly polarized SP emitter, the probability that a photon is emitted into the guided modes is given by the coupling efficiency

$$\beta = \sum_i p_i f_i = \frac{1}{\Gamma} \sum_i \Gamma_i^g \quad (2.8)$$

The fraction of the guided light originating from an i -polarized oscillating dipole is given by the factor

$$\beta_i = p_i f_i = \frac{\Gamma_i^g}{\Gamma} \quad (2.9)$$

Hence, an efficient, directional and polarized SP source requires that one of the β_i -factors, either β_y or β_z , is as close as possible to one (see coordinate system in Fig.2.1).

2.4 Results and discussion

Light emission from a single photon (SP) emitting inclusion embedded in the four photonic structures represented in Fig. 2.1 has been investigated by performing 3D finite-difference time-domain (FDTD) simulations. In all simulations the emitter is located at the center of the waveguide and is emitting at a wavelength of 650 nm. A photon emitted in a waveguide is in a superposition of two opposite propagation directions. The waveguide coupling factors and emission rates mentioned in the text account for both propagation directions ($\pm x$). A directional emission can be obtained by placing a reflector at one end of the waveguide.

2.4.1 Strip waveguides

Strip waveguides are simple to design and to fabricate using standard lithographic techniques. In the case depicted in Fig. 2.1a, the strip waveguide lies on a thick silicon oxide layer (refractive index $n = 1.46$) on a silicon chip. The case in Fig. 2.1b corresponds to an under-etched waveguide: the silicon oxide layer under the waveguide has been chemically removed and the

waveguide is suspended above the silicon chip. Both cases were simulated for different values of the waveguide width w and height h (see Fig. 2.1).

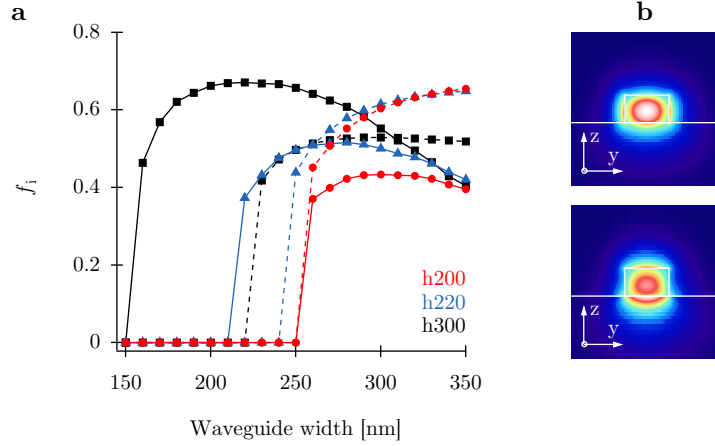


Figure 2.2: Strip SiN_x waveguide on substrate: (a) fraction of light radiated by a y-oscillating dipole (f_y , dashed line) and by a z-oscillating dipole (f_z , plain line) that is coupled to the guided modes as a function of the waveguide width w for three different waveguide heights $h = 200$ nm (red), 220 nm (blue), and 300 nm (black). (b) Mode profiles of the two guided modes for a waveguide with $h = 220$ nm and $w = 350$ nm. Top: fundamental TE mode. Bottom: fundamental TM mode.

Figure 2.2a displays the fraction of the light radiated by an oscillating dipole which is effectively coupled to guided modes. The coupled fraction f_y (f_z) radiated by a horizontally (vertically) oscillating dipole is plotted with dashed (plain) lines. A dipole oscillating in the longitudinal (x) direction does not couple efficiently to the waveguide ($f_x < 0.028$ in all cases). Three waveguide heights are considered: $h = 200$ nm (red curves), 220 nm (blue curves), and 300 nm (black curves). For each value of h , f_y and f_z are plotted as a function of the width w , ranging between 150 and 350 nm. In this parameter range, the waveguide can only support one TM mode and/or one TE mode. A vertically oscillating dipole couples mainly to the TM mode while a horizontally oscillating dipole couples mainly to the TE mode. When the width is swept from lower to higher values, the TM mode appears first. The mode profiles for a waveguide with $h = 220$ nm and $w = 350$ nm are shown in Fig. 2.2b. Figure 2.2a shows that the TM (TE) is supported from $w = 160$ nm ($w = 230$ nm) in waveguides with $h = 300$ nm, and from larger widths in the case of thinner waveguides. f_y and f_z on the order of 50%

and 65% respectively are achievable in 300 nm thick waveguides.

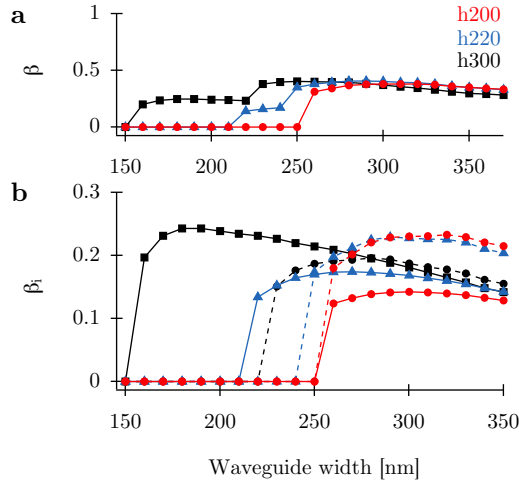


Figure 2.3: Strip SiN_x waveguide on substrate: (a) Total coupling factor β to the guided modes as a function of the waveguide width w for three different waveguide heights $h = 200$ nm (red), 220 nm (blue), and 300 nm (black). (b) Polarization dependent coupling factors β_y (dashed line) and β_z (plain line) as a function of the waveguide width w for three different waveguide heights $h = 200$ nm (red), 220 nm (blue), and 300 nm (black).

FDTD simulations were performed to calculate the radiation damping rates for dipoles oscillating in the three i -directions. The deduced Purcell factors F_i are found to be almost independent of the dipole polarization direction and the resulting probabilities p_i to emit in a specific polarization range between 0.21 and 0.45 in the entire range of interest. In Figure 2.3, the total coupling factor β (Fig. 2.3a) and the partial coupling factors β_y and β_z (Fig. 2.3b) are shown for the same waveguide geometries as in Fig. 2.2. For the taller waveguides ($h = 300$ nm), Fig. 2.3a shows that the coupling to the waveguide is only 25% in the single mode regime since only the field radiated by the z -polarization is guided. However, the collected light is perfectly polarized (TM mode). In the two-mode regime a collection efficiency of 40% can be reached at the expense of losing the control over the polarization state of the collected photon. Clearly the light collection efficiency in a strip SiN_x waveguide is not high enough to make an efficient single-photon source. However, the coupling can be dramatically improved by modifying the design of the waveguide.

The simplest modification consists in underetching the strip waveguide to create a suspended structure such as the one depicted in Fig. 2.1b. The underetching provides a better light confinement of the guided modes which improves the coupling to the emitter. In the range of heights and widths considered here the waveguide supports at least two modes: the fundamental TE and the following TM mode. Figure 2.4 shows that for taller waveguides ($h = 220$ nm, blue curves), the partial Purcell factors F_i range between 0.6 and 1.1. As in the case of SiN_x strip waveguides, this does not provide sufficient polarization selectivity to force the dipole to oscillate preferentially in one specific direction, and since the suspended waveguide always supports both a TE and a TM mode (see the mode profiles in Fig. 2.4b), no polarization selectivity of the photon source can be expected in this case. In thin waveguides, the field of the TM mode is expelled from within the waveguide. This is clearly seen in Fig. 2.4c for a waveguide with $h = 100$ nm. As a consequence the radiation of a z -polarized dipole is significantly inhibited (see Eq. 1.1), resulting in a small $F_z < 0.16$ factor. An unpolarized emitter placed in such a thin suspended waveguide would radiate as a y -polarized dipole with a probability p_y as high as 55% and potentially lead to highly polarized guided photons if the coupling to the TE mode is strong enough.

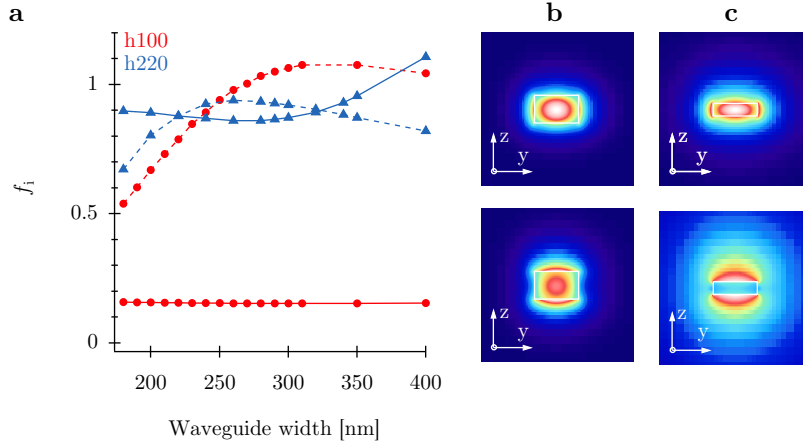


Figure 2.4: Suspended SiN_x waveguide: (a) Partial Purcell factor F_y (dashed line), and F_z (plain line) as a function of the waveguide width w for two waveguide heights: $h = 100$ nm (red) and $h = 200$ nm (blue). Mode profiles of guided fundamental TE and TM modes for a waveguide with dimensions: (b) $h = 200$ nm and $w = 350$ nm, (c) $h = 100$ nm and $w = 350$ nm.

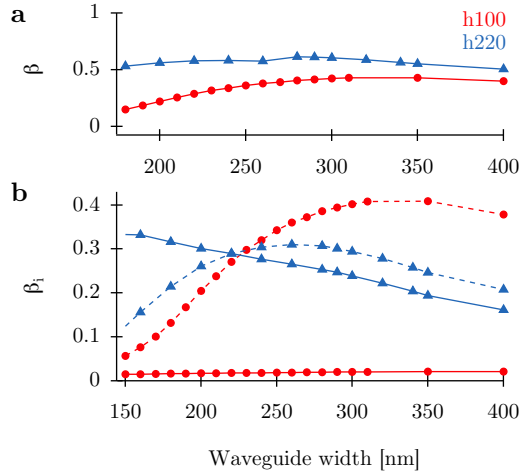


Figure 2.5: Suspended SiN_x waveguide: (a) Total coupling factor β to the guided modes as a function of the waveguide width W for two different waveguide heights $h = 100$ nm (red) and 220 nm (blue). (b) Polarization dependent coupling factors β_y (dashed line) and β_z (plain line) as a function of the waveguide width W for two different waveguide heights $h = 100$ nm (red) and 220 nm (blue).

The total coupling factor β is plotted as a function of w in Fig. 2.5a for waveguides with heights $h = 100$ nm (red curve) and $h = 220$ nm (blue curve). In Fig. 2.5b, the corresponding partial coupling factors β_y (dashed lines) and β_z (plain lines) are displayed. The coupling factor β_x is omitted because it is negligible for $h = 100$ nm and does not exceed 14% for $h = 220$ nm. In the case of tall waveguides ($h = 220$ nm, blue curve), the underetching significantly improves the coupling to guided modes, the β factor reaching values higher than 60%. This is essentially due to a better field confinement as can be seen by comparing the field profiles of Fig. 2.4b to those of Fig. 2.2b. However no polarization control is achievable in this case because the geometry does not provide a sufficient Purcell enhancement/inhibition and β_y and β_z have similar values, as shown in Fig. 2.5b. In the case of thin waveguides ($h = 100$ nm, red curve), a β -factor of 43% can be reached. The value is lower than in the case of tall waveguides because the confinement of the TM mode is worse. However, the geometry allows for a remarkable control over the polarization of the photons coupled to the waveguide. Indeed, Fig. 2.5 shows that the collected light is almost completely polarized in the y -direction, *e.g.* $\beta_y/\beta = 95\%$ for a

width $w = 310$ nm. In other words, the thin suspended waveguide geometry turns a completely unpolarized single-photon emitter into a linearly polarized single-photon source with a reasonable photon collection efficiency of 43%.

2.4.2 Slot waveguides

The efficiency of the photon/waveguide coupling can be enhanced by embedding the emitter into a thin SiO_x layer in the center of the SiN_x waveguide (see Figs. 2.1c and 2.1d). This kind of waveguide is called a slot-waveguide. Due to the continuity of the displacement field at any interface, this nanometer-sized slot of low index material ($n = 1.46$) in between two higher index ($n = 2$) regions results in a discontinuity of the electric field near the slot boundaries. Hence a large electric field develops in the low-index slot region for the mode which has its polarization orthogonal to the slot, in this case the TM mode (z -polarization). This improves the mode confinement and enhances the field strength at the position of the emitter, improving the coupling of the light emission into the waveguide. To illustrate the performance enhancement provided by a thin SiO_x -slot, let us consider the case of a tall ($h > w$) SiN_x strip waveguide only supporting a single TM mode (see Figs. 2.2a and 2.3). Such waveguides allows for the emission of perfectly polarized guided single-photons. Without a slot, the coupling efficiency factor is only $\beta = 25\%$. Figure 2.6a shows how introducing a 20-nm SiO_x slot improves the coupling efficiency. The taller the waveguide the easier single-mode operation can be achieved over a wide range of widths. For $h = 500$ nm, a β -factor of 37% can be reached. The light coupled into the waveguide is entirely polarized along the z -direction ($\beta \approx \beta_z$), see Fig. 2.6b. Simulations show that departing from the chosen slot height $h_g = 20$ nm does not change β significantly ($h_g \pm 10$ nm $\approx \beta \pm 4\%$). Figure 2.6c shows the mode profiles of the supported TE and TM modes for $h = 220$ nm and $w = 350$ nm. Comparing with Fig. 2.2b, we see that the TE-mode is not significantly modified by the slot, while the TM-mode shows an enhancement of the local field strength within the slot. The same local field enhancement is observed for tall waveguides ($h > w$) and is responsible for the improved coupling of the emitted photon to the single TM-mode, as discussed above.

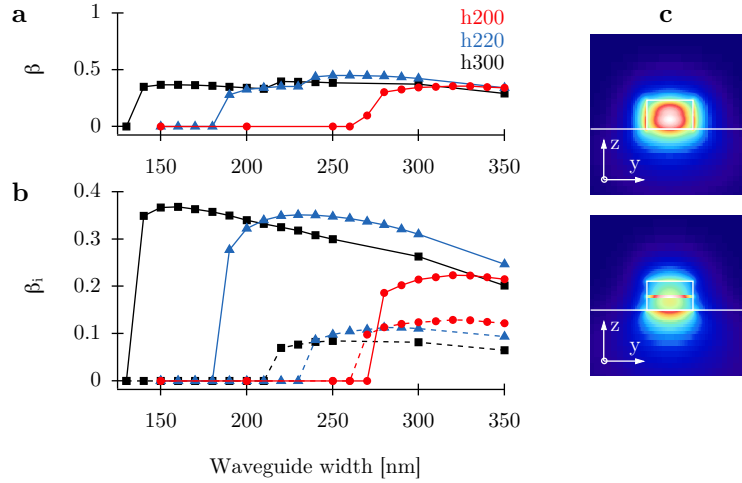


Figure 2.6: SiN Slot waveguide on substrate: (a) Total coupling factor β to the guided modes as a function of the waveguide width w for waveguide heights $h = 220$ nm (red), 300 nm (blue) and 500 nm (black). (b) Polarization dependent coupling factors β_y (dashed line) and β_z (plain line) for the same waveguide dimensions as in (a). The slot height is $h_g = 20$ nm. (c) mode profiles of the two guided modes for a waveguide with $h = 220$ nm and $w = 350$ nm. Top: fundamental TE mode. Bottom: fundamental TM mode.

The best coupling efficiencies in this study are obtained for suspended slot-waveguides, as in Fig. 2.1d. Figure 2.7a displays the partial Purcell factors F_y (dashed lines), and F_z (plain lines) as a function of the waveguide width w for two waveguide heights: $h = 300$ nm (red curve) and $h = 500$ nm (blue curve). In striking contrast with the suspended waveguide without a slot (see Fig. 2.4a), the partial Purcell factor F_z now takes values significantly higher than one, ranging between 2.6 and 4.4 in the investigated range. Also notice that the partial Purcell factor F_y can be made much smaller than one when w approaches 100 nm. This shows that one can simultaneously enhance the spontaneous emission from a z -polarized dipole and inhibit the spontaneous emission from a y -polarized dipole. In that case, a highly polarized emission is expected in a TM-mode, despite the existence of a TE-mode. The simultaneous enhancement of F_z and reduction of F_y can be understood by looking at the mode profiles. Figure 2.7b shows that the slot enhances the strength of the TM modal field at the center of the wave-

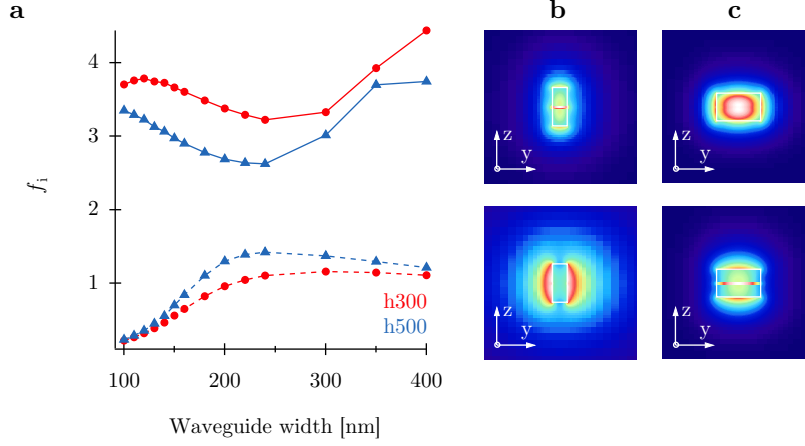


Figure 2.7: Suspended SiN_x slot-waveguide: (a) Partial Purcell factor F_y (dashed line), and F_z (plain line) as a function of the waveguide width W for two waveguide heights: $h = 300$ nm (red) and $h = 500$ nm (blue). (b) Mode profiles of guided fundamental TE and TM modes for a waveguide with dimensions: (b) $h = 220$ nm and $w = 350$ nm, (c) $h = 300$ nm and $w = 130$ nm.

uide where the emitter is positioned. The enhancement is stronger when there is no substrate under the waveguide since the modal area is smaller. It is responsible for the high values of F_z over the entire range of parameters. The reduced value of F_y is explained by the phenomenon already observed in Fig. 2.4c. When the waveguide becomes thin enough in one particular dimension, the field of the mode polarized orthogonally to that direction is expelled from the centre of the waveguide, resulting in a reduced matter light coupling. Here, the TE-field is expelled from the waveguide when $w < 150$ nm, which results in a F_y -value significantly smaller than one.

Figure 2.8 displays the total coupling factor β and the partial coupling factors β_y and β_z for suspended slot-waveguides with height $h = 300$ nm (red curves) and $h = 500$ nm (blue curves). Figure 2.8a shows that, for both heights, the waveguide geometry leads to coupling factors as high as $\beta = 59\%$ when $w = 120$ nm. Figure 2.8b further shows that the β_z/β_y ratio is higher in the $h = 300$ nm case than in the $h = 500$ nm case, in accordance with the discussion above and the Purcell factors displayed in Fig. 2.7a. For $w = 120$ nm, β_x is negligible, $\beta_y = 3\%$, and $\beta_z = 56\%$. This results in a very high polarization ratio $\beta_z/\beta = 96\%$ for the guided light. Going to

wider waveguides results in a higher β but also in a lower polarization ratio. A maximal overall coupling of 67% is found for a waveguide with dimension $h = 300$ nm and $w = 220$ nm, and $\beta_z/\beta = 74\%$. Replacing the SiO_x layer by an air slot, would result in even higher Purcell factors (F_z up to 14) and hence an even higher degree of polarization (98%) and total coupling (59%) can be achieved.

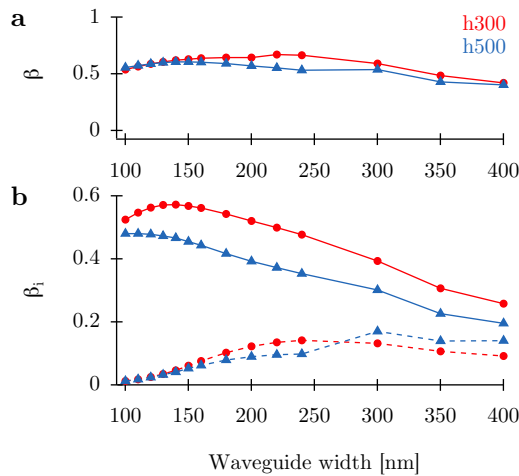


Figure 2.8: Suspended SiN_x slot-waveguide: (a) Total coupling factor β to the guided modes as a function of the waveguide width W for two different waveguide heights $h = 300$ nm (red) and 500 nm (blue). (b) Polarization dependent coupling factors β_y (dashed line) and β_z (plain line) as a function of the waveguide width W for two different waveguide heights $h = 300$ nm (red) and 500 nm (blue).

2.5 Conclusion

Our study shows that high efficiency in-plane SP sources can in principal be realized using SiN_x photonic devices as simple as waveguides. We showed that light from a SP emitter can be efficiently coupled to the waveguide. High coupling factors β ranging between 40% and 67% were found in the four waveguide geometries under investigation. Furthermore, we showed that under certain geometrical conditions, the emitted photon can be coupled to a single polarized guided (TE or TM) mode. In that case, an effective polarized SP source is built even if the SP emitter itself is unpolarized. In

suspended strip waveguides, we show that one can simultaneously achieve a good coupling factor $\beta = 43\%$ and a high polarization ratio $\beta_y/\beta = 95\%$. In suspended slot waveguides, a higher coupling factor $\beta = 56\%$ is achievable in combination with a similar polarization ratio $\beta_z/\beta = 96\%$.

These results demonstrate that high efficiency single-photon sources and complex optical circuits can be combined on a single photonic chip for quantum optics experiments. The SiN_x sources and optical circuits can be manufactured using well-established CMOS-compatible processing technology. Because the SiN_x transparency range extends from the visible to the infrared, the envisaged platform is compatible with several types SP emitting inclusions such as colloidal quantum dots, nanoparticles containing a single color centre, and single-ion doped nanoparticles.

References

- [1] E. Knill, R. Laflamme, and G. J. Milburn, “A scheme for efficient quantum computation with linear optics,” *Nature*, vol. 409, pp. 46–52, jan 2001.
- [2] M. Varnava, D. E. Browne, and T. Rudolph, “How good must single photon sources and detectors be for efficient linear optical quantum computation?,” *Physical Review Letters*, vol. 100, no. 6, pp. 1–4, 2008.
- [3] T. D. Ladd, F. Jelezko, R. Laflamme, Y. Nakamura, C. Monroe, and J. L. O’Brien, “Quantum computers,” *Nature*, vol. 464, pp. 45–53, mar 2010.
- [4] N. Gisin, G. Ribordy, W. Tittel, and H. Zbinden, “Quantum cryptography,” *Reviews of Modern Physics*, vol. 74, no. 1, pp. 145–195, 2002.
- [5] V. Scarani, H. Bechmann-Pasquinucci, N. J. Cerf, M. Dusek, N. Lütkenhaus, and M. Peev, “The security of practical quantum key distribution,” *Reviews of Modern Physics*, vol. 81, no. 3, pp. 1301–1350, 2009.
- [6] M. Rau, T. Heindel, S. Unsleber, T. Braun, J. Fischer, S. Frick, S. Nauerth, C. Schneider, G. Vest, S. Reitzenstein, M. Kamp, A. Forchel, S. Höfling, and H. Weinfurter, “Free space quantum key distribution over 500 meters using electrically driven quantum dot single-photon sources - A proof of principle experiment,” *New Journal of Physics*, vol. 16, 2014.
- [7] J. F. Dynes, Z. L. Yuan, A. W. Sharpe, and A. J. Shields, “A high speed, postprocessing free, quantum random number generator,” *Applied Physics Letters*, vol. 93, no. 3, pp. 3–5, 2008.
- [8] C. H. Bennett, F. Bessette, G. Brassard, L. Salvail, and J. Smolin, “Experimental quantum cryptography,” *Journal of Cryptology*, vol. 5, no. 1, pp. 3–28, 1992.
- [9] S. Takeuchi, “Experimental demonstration of a three-qubit quantum computation algorithm using a single photon and linear optics,” *Physical Review A*, vol. 62, p. 32301, aug 2000.
- [10] E. Brainin, L.-P. Lamoureux, N. J. Cerf, P. Emplit, M. Haelterman, and S. Massar, “Fiber-Optics Implementation of the Deutsch-Jozsa and Bernstein-Vazirani Quantum Algorithms with Three Qubits,” *Physical Review Letters*, vol. 90, p. 157902, apr 2003.

- [11] L. P. Lamoureux, E. Brainis, D. Amans, J. Barrett, and S. Massar, “Provably Secure Experimental Quantum Bit-String Generation,” *Physical Review Letters*, vol. 94, p. 50503, feb 2005.
- [12] L. P. Lamoureux, E. Brainis, N. J. Cerf, P. Emplit, M. Haelterman, and S. Massar, “Experimental error filtration for quantum communication over highly noisy channels,” *Physical Review Letters*, vol. 94, no. 23, pp. 1–4, 2005.
- [13] A. Crespi, R. Osellame, R. Ramponi, D. J. Brod, E. F. Galvao, N. Spagnolo, C. Vitelli, E. Maiorino, P. Mataloni, and F. Sciarrino, “Integrated multimode interferometers with arbitrary designs for photonic boson sampling,” *Nat Photon*, vol. 7, pp. 545–549, jul 2013.
- [14] A. Politi, M. J. Cryan, J. G. Rarity, S. Yu, and J. L. O’Brien, “Silicon-Silicon Waveguide Quantum Circuits,” *Science*, vol. 320, no. 5876, pp. 646–649, 2008.
- [15] J. B. Spring, B. J. Metcalf, P. C. Humphreys, W. S. Kolthammer, X.-M. Jin, M. Barbieri, A. Datta, N. Thomas-Peter, N. K. Langford, D. Kundys, J. C. Gates, B. J. Smith, P. G. R. Smith, and I. A. Walmsley, “Boson Sampling on a Photonic Chip,” *Science*, vol. 339, pp. 798 LP – 801, feb 2013.
- [16] N. Spagnolo, C. Vitelli, M. Bentivegna, D. J. Brod, A. Crespi, F. Flamini, S. Giacomini, G. Milani, R. Ramponi, P. Mataloni, R. Osellame, E. F. Galvao, and F. Sciarrino, “Experimental validation of photonic boson sampling,” *Nat Photon*, vol. 8, pp. 615–620, aug 2014.
- [17] J. Claudon, J. Bleuse, N. S. Malik, M. Bazin, N. Gregersen, C. Sauvan, P. Lalanne, and Gerard, “A highly efficient single-photon source based on a quantum dot in a photonic nanowire,” *Nature Photonics*, vol. 4, no. March, pp. 174–177, 2010.
- [18] N. Gregersen, T. R. Nielsen, J. Mørk, J. Claudon, and J.-M. Gérard, “Designs for high-efficiency electrically pumped photonic nanowire single-photon sources,” *Optics Express*, vol. 18, no. 20, pp. 21204–21218, 2010.
- [19] M. E. Reimer, G. Bulgarini, N. Akopian, M. Hocevar, M. B. Bavinck, M. A. Verheijen, E. P. Bakkers, L. P. Kouwenhoven, and V. Zwiller, “Bright single-photon sources in bottom-up tailored nanowires,” *Nature Commun.*, vol. 3, p. 737, 2012.

- [20] X. Brokmann, G. Messin, P. Desbiolles, E. Giacobino, M. Dahan, and J. P. Hermier, “Colloidal CdSe/ZnS quantum dots as single-photon sources,” *New Journal of Physics*, vol. 6, pp. 1–8, 2004.
- [21] Y. Chen, J. Vela, H. Htoon, J. L. Casson, D. J. Werder, D. A. Bussian, V. I. Klimov, and J. A. Hollingsworth, “Giant Multishell CdSe Nanocrystal Quantum Dots with Suppressed Blinking,” *Journal of the American Chemical Society*, vol. 130, pp. 5026–5027, apr 2008.
- [22] B. Mahler, P. Spinicelli, S. Buil, X. Quelin, J.-P. Hermier, and B. Dubertret, “Towards non-blinking colloidal quantum dots,” *Nat Mater*, vol. 7, pp. 659–664, aug 2008.
- [23] F. Pisanello, L. Martiradonna, G. Leménager, P. Spinicelli, A. Fiore, L. Manna, J. P. Hermier, R. Cingolani, E. Giacobino, M. De Vittorio, and A. Bramati, “Room temperature-dipolelike single photon source with a colloidal dot-in-rod,” *Applied Physics Letters*, vol. 96, no. 3, pp. 3–6, 2010.
- [24] A. Beveratos, R. Brouri, T. Gacoin, J.-P. Poizat, and P. Grangier, “Nonclassical radiation from diamond nanocrystals,” *Physical Review A*, vol. 64, p. 61802, nov 2001.
- [25] Y. Shen, T. M. Sweeney, and H. Wang, “Zero-phonon linewidth of single nitrogen vacancy centers in diamond nanocrystals,” *Physical Review B*, vol. 77, p. 33201, jan 2008.
- [26] R. Kolesov, K. Xia, R. Reuter, R. Stöhr, A. Zappe, J. Meijer, P. R. Hemmer, and J. Wrachtrup, “Optical detection of a single rare-earth ion in a crystal,” *Nature Communications*, vol. 3, p. 1029, aug 2012.
- [27] B. De Geyter, K. Komorowska, E. Brainis, P. Emplit, P. Geiregat, A. Hassinen, Z. Hens, and D. Van Thourhout, “From fabrication to mode mapping in silicon nitride microdisks with embedded colloidal quantum dots,” *Applied Physics Letters*, vol. 101, no. 16, p. 161101, 2012.
- [28] Q. Xu, V. R. Almeida, R. R. Panepucci, and M. Lipson, “Experimental demonstration of guiding and confining light in nanometer-size low-refractive-index material,” *Optics Letters*, vol. 29, no. 14, pp. 1626–1628, 2004.
- [29] M. Galli, D. Gerace, A. Politi, M. Liscidini, M. Patrini, L. C. Andreani, A. Canino, M. Miritello, R. L. Savio, A. Irrera, and F. Priolo, “Direct evidence of light confinement and emission enhancement in active

- silicon-on-insulator slot waveguides,” *Applied Physics Letters*, vol. 89, no. 24, pp. 1–4, 2006.
- [30] Y. C. Jun, R. M. Briggs, H. a. Atwater, and M. L. Brongersma, “Broadband enhancement of light emission in silicon slot waveguides.,” *Optics express*, vol. 17, pp. 7479–90, apr 2009.
- [31] L. Novotny and B. Hecht, *Principles of Nano-Optics*. Cambridge University Press, 2006.

3

Fabrication and characterization of SiN_x/Au cavities with colloidal QDs

In this chapter we demonstrate the fabrication and characterization of on-chip vertically-emitting SiN_x/Au nanopatch cavities containing a monolayer of colloidal quantum dots. The Purcell enhancement of the spontaneous emission of the quantum dots is studied theoretically and experimentally. The fabrication process is based on electron-beam lithography and allows to deterministically position both the cavity and the emitters within the cavity.

3.1 Introduction

The coupling of single-photon emitters to dielectric cavities or plasmonic cavities/antennas has been demonstrated using a variety of physical systems with the aim of making the source brighter and more directive.¹ Some examples include microcavities at cryogenic temperatures,²⁻⁵ photonic crystal waveguides,⁶ nanobeam waveguides⁷ and near-field coupling to metallic nano-antennas.^{8:9} Such solid-state single-photon sources are key for optical quantum information processing. Engineering an efficient solid-state single-photon source requires one to address several important challenges, some

of which are sometimes overlooked: (i) the single-photon source must be fabricated in a robust, scalable and reproducible manner, (ii) the position of the single-photon source on the chip must be controlled with nanometer to micrometer accuracy (depending on the application), (iii) the fabrication methods must be compatible with a deterministic positioning of a single emitter at the required site within the device with a few nanometer accuracy, (iv) the radiative yield of the single-photon device must be as high as possible and ideally close to one.

With their large absorption cross section and high radiative quantum yield (as high as 90% in the best cases) colloidal core/shell quantum dots (QDs), such as the CdSe/CdS QDs fabricated according to the so-called ‘flash’ synthesis method¹⁰ or the recently demonstrated InP/ZnSe QDs,¹¹ are suitable room-temperature single-photon emitters. Good quality monolayers of such QDs are obtained by Langmuir-Blodgett deposition.¹² We recently showed that such monolayers can be nano-patterned with very high accuracy and demonstrated that single QDs can be isolated at predefined locations with a record success probability of over 40%.¹³ However, their deterministic positioning and coupling to resonators still remains challenging. Because of their broad emission line at room-temperature (10 – 30 nm), the resonator must combine a large resonance linewidth with an ultra-small mode volume. In the past, this has been achieved through plasmonic coupling. Plasmonic coupling has proven to be very effective to speed up radiative decay; *e.g.* a record 540-fold reduction in the luminescence lifetime has recently been observed in a system consisting of ad hoc positioned QDs and silver nanocubes.^{8;14} The local-field enhancement at the nanocube corners is responsible for this exceptionally strong Purcell effect. In circular cavities and nanostructures, more modest enhancements of the spontaneous emission rates of QDs have been reported before,^{9;15} typically of the order of 30 or less. Similar enhancements have also been observed with other types of quantum emitters such as molecules¹⁶ or nitrogen-vacancy centers in diamond nanocrystals.¹⁷ However, devices based of plasmonic coupling usually suffer from non-radiative energy dissipation, significantly reducing their effective quantum yield and precluding their usage for applications where a high radiative quantum yield is of the essence. For instance, in the nanopatch-cavity design demonstrated in reference⁹ by Belacel *et al.*, the radiative efficiency was only a few percent.

Here, we investigated a different circular metallic *nanopatch-cavity* design in which the coupling between the QDs and the scalable circular cavity is dominantly dielectric rather than plasmonic. Our cavities are accurately

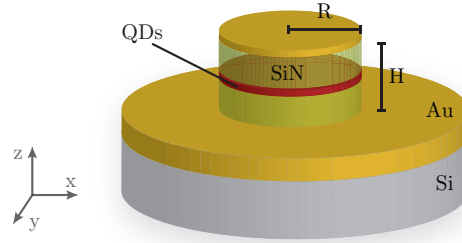


Figure 3.1: Schematic representation of a nanopatch cavity with height H and radius R

fabricated using modern and scalable lithographic techniques. They are fully etched to reduce losses and increase the radiative yields of the device up to about 60%, while still providing a broad cavity resonance line and a subwavelength mode volume. This type of resonators has been used in the past to demonstrate small mode volume infrared semiconductor lasing.¹⁸ Also in contrast with reference⁹, in which QDs were transferred to the substrate by dip coating and formed randomly distributed clusters containing a random number of QDs, our cavities contain a uniform monolayer of QDs that can be further patterned down to a single QD, as shown in reference¹³. In addition, our fabrication method is compatible with any colloidal QD material, such that further optimisation of the SP emitter (*e.g.* through synthesis) can be done independently from the cavity fabrication.

3.2 Cavity structure and fabrication

The nanopatch cavities consist of a monolayer of QDs embedded in a silicon nitride (SiN_x) matrix sandwiched between two Au layers (see Fig. 3.1) resulting in subwavelength confinement of the optical resonant modes. As the Purcell factor F scales with Q/V , large enhancements are expected for cavities with high Q-factors and small mode volumes. Because the emission line of QDs is broad at room temperature (typically 30 nm), only a low Q-factor of 20 or less is required. From finite-difference time-domain (FDTD) simulations (see Section 3.3.2), Purcell factors of 5 – 10 are nevertheless expected for a single QD in the center of the cavity, due to the small mode volume. A fabrication process was designed that allows for the fabrication of large arrays of such cavities with fixed height H and varying radii R . Figure 3.2 shows a small area of such an array in which cavities with a ra-

dus of 300 nm were formed every 5 μm . Figure 3.3 schematically shows the fabrication flow of the nanopatches. First, 2–3 nm of titanium (adhesion layer) is sputtered onto a silicon wafer, followed by the evaporation of a 100 nm thick Au layer. Note that such a Ti layer is deposited before each of the following Au deposition steps. Next a 60 nm SiN_x layer is deposited using an optimized plasma-enhanced chemical vapor deposition (PECVD) process at a temperature of 120°C.¹⁹ A low plasma frequency is chosen to reduce the optical loss as well as the material luminescence of the SiN_x layer (see Section 1.3.3). Next, cross-shaped Au markers are patterned using Electron-beam (e-beam) lithography and a standard lift-off process, see Fig. 3.5a. These markers are used in the following lithographic steps to ensure that the QDs are accurately positioned at the center of the cavity. Some additional large crosses were added at the bottom of each write field to allow a quick assessment of both Au-pattern and QD-pattern alignment using a microscope, see Figs. 3.5c and 3.5d respectively.

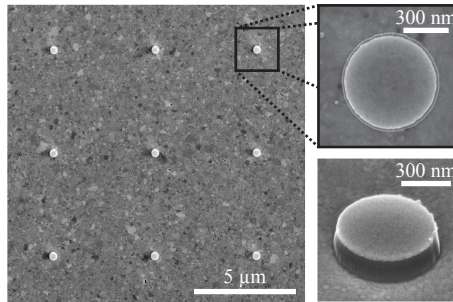


Figure 3.2: SEM images of an array of deterministically positioned nanopatches, and zoom of (top) top view and (bottom) tilted view of a single nanopatch cavity.

The deposition of the QDs follows the process developed in reference¹³ and constitutes the next three steps depicted in Fig. 3.3. It consists of (ii) the definition of the deposition area by e-beam lithography, (iii) the formation of a uniform QD-monolayer using Langmuir-Blodgett deposition, and (iv) a lift-off step to remove the QDs covering the e-beam resist. We used oleate-passivated CdSe/CdS core/shell QDs synthesized by a seeded-growth ‘flash’ approach¹⁰ with a core diameter of 3.1 nm, total diameter of 9.5 nm and a central emission peak of 630 nm. After the patterning step, circular patches of monolayer-QDs stay behind. Their quality was examined using a high-resolution scanning electron microscope (SEM) (FEI Nova 600), see Fig. 3.4a. By automated image recognition, the QD-patches were accurately

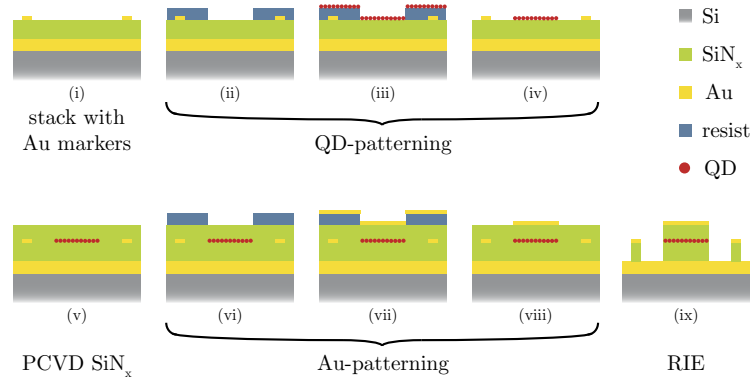


Figure 3.3: Schematic representation of the nanoptach fabrication flow.

aligned with respect to the Au-markers, allowing to deterministically position them in the center of the cavities and leave no QDs outside the cavities. This technique provides a good control of both the quality and thickness of the QD layer, which is important to control the shape of the pattern and the *number of QDs* per cavity which can be controlled down to a single QD with a high probability of success, as demonstrated in reference¹³. A second 60 nm SiN_x layer is subsequently deposited using the same PECVD process for embedding the QDs, as shown in step (v). As demonstrated in previous work²⁰, this low temperature SiN_x deposition is crucial for preserving the luminescent properties of the QDs, such as a high quantum yield. The size and shape of the circular top Au layer (40 nm thickness), which define the resonant wavelength, are precisely controlled during a final e-beam lithography step (vi) and lift-off step (vii)-(viii). The deposition of the Au patches is again aligned with respect to the Au markers. Finally, the resonators are etched using an optimized dry etching process (RIE with CF₄/H₂), in which the top Au disks act as a hard mask. As a demonstration of our alignment accuracy, we fabricated patches in which the QD patches have a diameter two times smaller than the cavity itself. The result is displayed in Fig. 3.4b and c, where a cross-section and a tilted view of the final cavity are shown. In both SEM-pictures the area containing the QDs is clearly visible and it can be seen that they are patterned exactly in the center. Figures 3.4d and 3.4e are SEM images of a misaligned disk shaped QD-pattern with a diameter equal to the cavity itself, demonstrating the importance of this patterning step to ensure a clean and nicely defined cavity. As mentioned in Section 1.3.3, dry etching of QDs is possible but generally require longer

etching times compared to SiN_x , such that QDs outside the cavity leave behind a rough background with lots of residu. The final cavity with correct alignment is shown in Fig. 3.4f. This process-flow allows us to deterministically position the QDs in the cavity, and align the cavity itself on the chip with an accuracy of 10 nm, which corresponds to roughly the size of one QD.

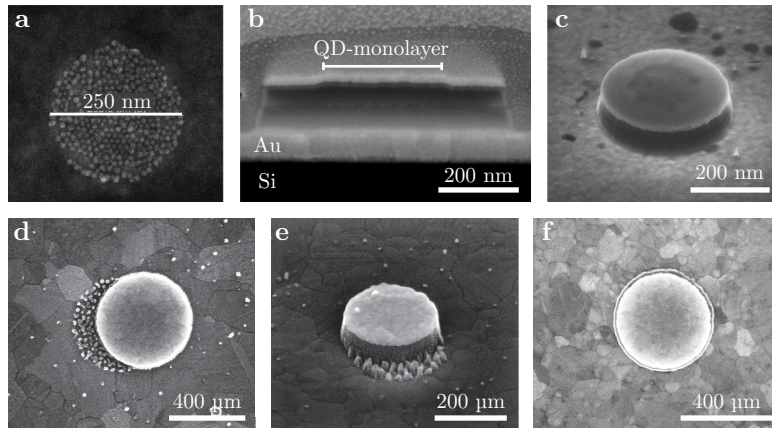


Figure 3.4: (a) Disk-shape patterned monolayer of QDs, (c)-(d) Illustration of alignment accuracy: cross-section of a cavity of radius $R = 300$ nm with a QD monolayer forming a circular patch of radius 150 nm right in the center of the cavity. Tilted view of the same cavity shown in (b). The height difference caused by the QD-pattern can be seen in the top Au layer. (d)-(e) Top and tilted view of etched QDs pattern outside of cavity. (f) Top view of final cavity with correct alignment.



Figure 3.5: Microscope images of the final photonic chip. The large bars around the photonic structures makes it easier to find the actual cavities under the optical microscope, SEM and the PL-setup. (a) Zoom of Au-markers. The big cross is used for rough alignment, followed by a fine alignment with the small crosses. (b) Zoom of one WF, each write field is aligned separately (automatically). The big crosses at the bottom of each WF are used for checking the alignment of (c) Au-pattern and (d) QD-patterns.

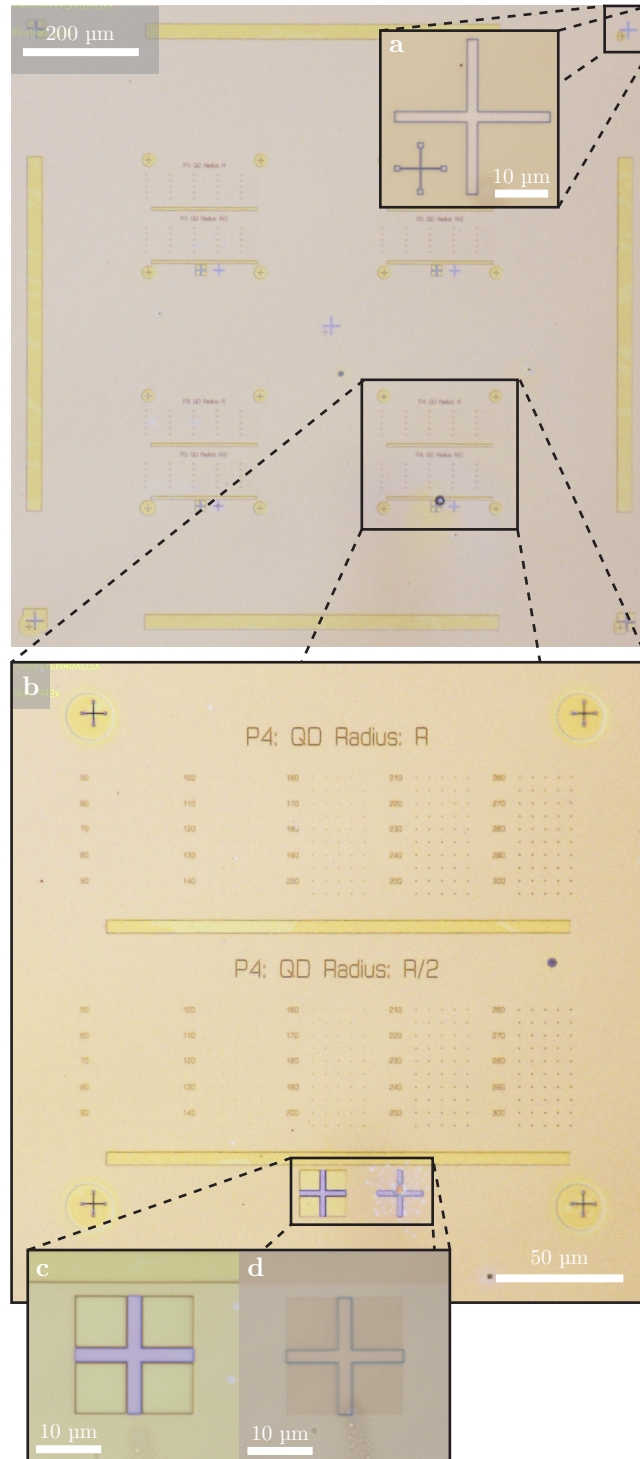


Figure 3.5

3.3 Simulations

To theoretically study the Purcell enhancement of the spontaneous emission of the quantum dots in a nanopatch-cavity, 3D FDTD simulations are performed, in which the QDs are modelled by classical electric dipoles with a well defined linear dipole moment and orientation. An important and non-trivial optical parameter needed in such a simulation is the dielectric function of the used dielectrics. Due to quantum confinement, the permittivity of QDs is substantially different from their bulk counterparts. In addition, QDs consists of both semiconductor material and organic ligands. Ellipsometry, the usual method to determine the optical properties of a layer, requires knowledge of a good model, which is not available in this case. However, it is possible to determine the complex dielectric function from an experimental absorption spectrum by using an iterative procedure based on a combination of the Kramers-Krönig (KK) relations and the Maxwell-Garnett effective medium approximation.

3.3.1 Permittivity of a QD layer

In bulk materials, the optical constants can be determined from the KK analysis of their absorption coefficient α . The extinction coefficient κ , being the imaginary part of the complex refractive index $\tilde{n} = n + i\kappa$, is directly related to α by $\alpha = 2\kappa\omega/c$. If κ can be determined over a wide enough spectral range, the refractive index n can be found using the KK relation relating the real and imaginary part of a causal complex function:

$$n(\omega) = 1 + \frac{2}{\pi} \mathcal{P} \int_0^{\infty} \frac{\omega' \kappa(\omega')}{\omega'^2 - \omega^2} d\omega' \quad (3.1)$$

From these values ε_R and ε_I can be determined. However, according to the Maxwell-Garnett effective medium theory, the intrinsic absorption coefficient μ of a QD dispersion is determined by both real and imaginary parts of ε and the solvent refractive index n_s (see Eq. (1.12)). Although this hampers a straightforward KK analysis, we can still obtain ε by an iterative procedure which was developed at our group.²¹ We start from trial functions $\varepsilon_{I,0}$ and $\varepsilon_{R,0}$ from which μ_0 is calculated using Eq. (1.12), yielding an initial estimate with obviously $\mu_0 \neq \mu$. Next, this μ_0 is compared with an experimentally measured absorption coefficient μ , which can be found by rescaling the absorption spectrum at short wavelengths as explained in Section 1.2.2.4. This difference $\Delta\mu$ is transformed back in $\Delta\varepsilon_I$, which is the difference between the trial function and the true value: $\varepsilon_I = \varepsilon_{I,0} + \Delta\varepsilon_I$. Just as for ε , the change $\Delta\varepsilon$ must also obey the KK relations, resulting in

$\varepsilon_R = \varepsilon_{R,0} + \Delta\varepsilon_R$. From these updated dielectric functions ε_I and ε_R an improved μ -spectrum is calculated, which is compared again with the experimental one. This process continues until μ converges to the experimental one with a root-mean-square error $< 10^{-6}$.

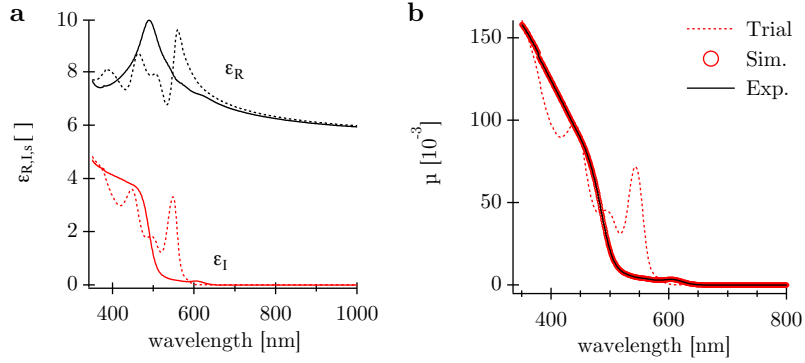


Figure 3.6: (a) Real (black) and imaginary (red) parts of permittivity function of core/shell CdSe/CdS QDs, dashed lines are initial guesses, full lines are the simulation results. (b) The corresponding absorption coefficient μ , with red dashed curve the first guess and open red circles the μ obtained after the simulation has converged to the experimentally measured μ (black).

As a first guess, we used the dielectric function obtained by Alves-Santos *et al.*²² for zincblende CdSe QDs with a diameter of 3.2 nm, which is close to the size of the cores of our dots ($d = 3.1$ nm). The first-guess $\varepsilon_{I,0}$ and $\varepsilon_{R,0}$ and corresponding μ_0 are shown in figures 3.6a and 3.6b respectively by dashed lines. The full lines are the resulting ε_I and ε_R and μ spectra after the calculation has converged. From this complex dielectric function the real refractive index of the QDs can be calculated according to:

$$n = \sqrt{\frac{\sqrt{\varepsilon_R^2 + \varepsilon_I^2} + \varepsilon_R}{2}} \quad (3.2)$$

The result is shown as a red curve in Fig. 3.7. However, a layer of QDs consists also of organic ligands and in order to obtain an effective permittivity ε_{eff} , we can again use the Maxwell-Garnet model from Eq. (1.3). We assume a closest packing of the QDs, with a 25% volume fraction of QDs, 50% of ligands ($n = 1.5$) and 25% of air ($n = 1$). Using again Eq. (3.2) the real refractive index of the QD layer can be calculated and is shown in Fig. 3.7

as a black curve. We find a refractive index of 1.6 at wavelength 630 nm. This value can be used in the FDTD simulations. The optical parameters of SiN_x , SiO_2 , and Au are shown in Figs. 1.12 and 1.13.

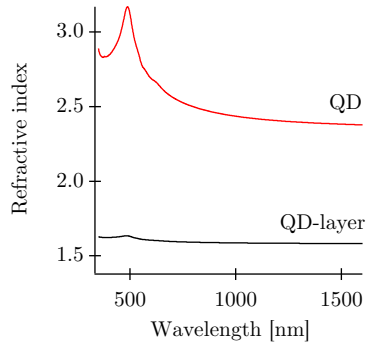


Figure 3.7: Calculated refractive index as a function of wavelength for a CdSe/CdS QD (red) and a layer of the same dots (black) using the permittivity spectra found in Figure 3.6a.

3.3.2 Optical modes in the nanopatch cavity

Depending on the dimensions of the cavities, various optical modes are supported. We are interested in the subwavelength modes that exhibit small optical losses and a large spatial and spectral overlap with our active material. We present FDTD simulation results for the fundamental quasi- TM_{111} and quasi- TE_{011} modes; the analytical expressions of these modes have been reported in literature.^{23;24} In all our simulations, the thickness of the top and bottom Au layers was taken to be 40 nm and 100 nm, respectively. In order to characterize these modes, we first determined their resonance wavelength λ_{res} as function of cavity parameters H and R . The results for TM_{111} and TE_{011} modes are shown in Fig. 3.8a and 3.8b respectively. The TE mode does not couple well with the surface plasmons and requires a larger cavity dimension to achieve the same mode wavelength compared to the TM mode. The central wavelength of a TE mode is also more sensitive to the radius of the cavity. The horizontal dotted line represents the emission wavelength of our QDs ($\lambda = 630$ nm) and the grey area around it corresponds to the FWHM of the QDs emission line. By selecting the cavity height and the cavity radius such that λ_{res} falls in the center of the grey region, a resonance with the QD emission is achieved. The spatial energy distributions of these modes (top and side views) are also shown

as insets in Fig. 3.8. The FDTD simulations also provides the FWHM of the cavity lines ($\Delta\lambda$), from which the quality factor $Q = \lambda_{\text{res}}/\Delta\lambda$ can be deduced. Q -factors were only computed for those cavities that support a mode resonating with the QDs. We found Q -factors in the 10 – 15 range for the TM-modes and in the 13 – 16 range for the TE-modes.

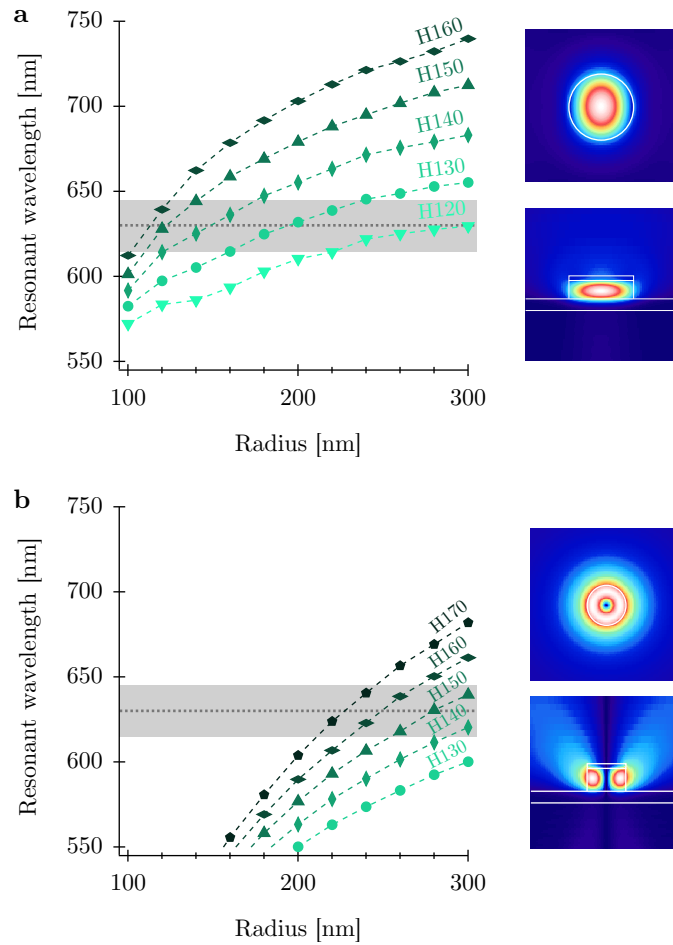


Figure 3.8: Resonant wavelength of the (a) TM₁₁₁ and (b) TE₀₁₁ modes as a function of cavity dimensions radius R and height H (ranging from 120 nm to 170 nm, see data labels). The central emission wavelength and linewidth of the QDs, which were integrated in the cavities, are indicated in grey. To the right, a horizontal and vertical slice of the magnitude of the electric field mode profiles are shown.

Next we calculated the radiative decay rates Γ_i ($i \in \{x, y, z\}$) of classical dipoles oscillating in the x , y and z directions. In a structured environment, the decay rates Γ_i usually differ from each other and lead to an enhancement (or inhibition) characterized by the Purcell factor $F_i = \Gamma_i/\Gamma_{\text{hom}}$, where Γ_{hom} is the decay rate the dipole would have in a homogeneous medium. The highest enhancement is found when the dipole is placed at the position of the highest mode field intensity and has a polarization tangential to the electric field lines. In the case of a linear dipole coupled to a TM_{111} mode, this occurs for an electric dipole positioned in the center of the cavity with the dipole moment in the xy -plane. The dipole then couples to the TM_{111} mode with field lines parallel to the polarization direction of the linear dipole.¹⁸ Figure 3.9a shows the values of the Purcell factor F_x at wavelength 630 nm for a x -polarized dipole at the center of the cavity with varying cavity dimensions (for symmetry reasons, the result is the same for a y -polarized dipole, thus $F_y = F_x$). It can be seen that the highest enhancement ($F_x = F_y = 7.4$) is found for a cavity with height $H = 130$ nm and radius $R = 200$ nm. Note that these values also strongly depend on the thickness of the top Au layer. Figure 3.9b shows F_x (at $\lambda = 630$ nm) in a cavity with a top Au-layer thicknesses varying between 20 – 60 nm and a fixed cavity height of $H = 130$ nm. As expected, thinner Au layers result in

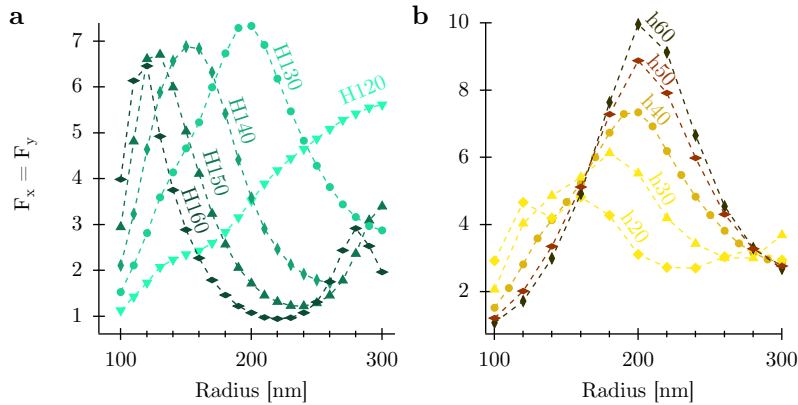


Figure 3.9: (a) Purcell factor $F_x = F_y$ for a linear dipole (emitting at 630 nm) positioned at the center of the cavity as a function of cavity radius R for (a) five different cavity heights H ranging from 120 to 160 nm and (b) varying thickness of the top Au layer ranging from 20 to 60 nm and fixed H of 130 nm. The maxima of each curve corresponds to resonance with TM_{111} .

less confinement and hence lower enhancements. In addition the peak, which corresponds to resonance, shifts towards smaller radii. Although thicker Au layers result in higher enhancement, we chose to work with a thickness of 40 nm as the cavities are pumped and collect from the top. The thickness of the bottom Au layer has a similar effect. However, going to layers which are > 100 nm thick is not economical, as increasing the thickness even further results in minor additional enhancements.

The same analysis for the TE₀₁₁ mode (which has field lines circulating around the center of the cavity¹⁸) shows that the highest Purcell factor is obtained for an electric linear dipole positioned at a distance $0.75 R$ from the cavity center with its dipole moment in the cavity plane in the direction orthogonal to that displacement. By sweeping through the values of H and R , the highest Purcell factor found in this case is slightly smaller than 4. Because the TM₁₁₁ mode offers a larger Purcell enhancement, we decided to design our nanopatch-cavities for the TM₁₁₁ modes. The Far-field projection of this TM₁₁₁ is shown in Fig. 3.10, showing that most of the upward emitted light ($\sim 83\%$) falls within a 40° cone.

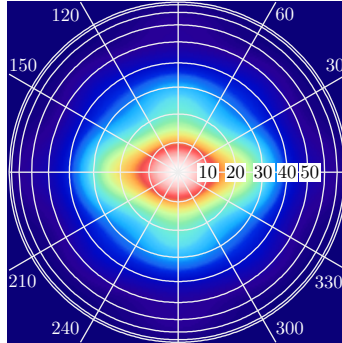


Figure 3.10: Farfield radiation pattern for TM₁₁₁ mode.

Consider a cavity geometry supporting a resonant TM₁₁₁ mode at 630 nm, *e.g.* $R = 200$ nm and $H = 130$ nm. When the linear dipole is moved away from the cavity center, the coupling to the TM₁₁₁ modes changes, and so does the enhancement of the spontaneous decay rate. Figure 3.11 shows the evolution of the Purcell factors F_x , F_y and F_z when the dipole is displaced in the x -direction. The factors F_x and F_y do not evolve exactly in the same manner because dipoles vibrating in the x - and y -directions couple to hybrid TM₁₁₁ modes with different intensity profiles which are slightly elongated in the direction orthogonal to the E-field in the center of the cavity. Note that a dipole vibrating in the z -direction does not experience

much Purcell enhancement. This is in striking contrast with the nanopatch cavities of reference⁹ in which F_z factors of the order of 50 have been reached by plasmonic coupling at the expense of very large optical losses.

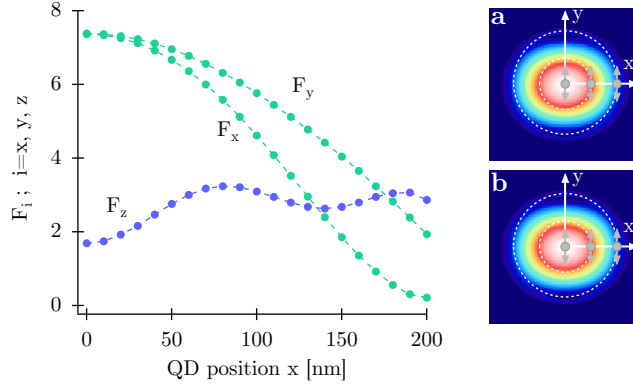


Figure 3.11: Purcell factors F_i ($i \in \{x, y, z\}$) as a function of dipole position x in a cavity with $H = 130$ nm and $R = 200$ nm. The insets show the mode profiles of the two hybrid TM_{111} modes excited by an x - and y - polarised dipole respectively.

3.3.3 Effect of random QD orientation and position

Low temperature measurements reveal that QD excitons can recombine through π (linear dipole along the QD c -axis) and σ_{\pm} (circular dipoles in the plane orthogonal to the QD c -axis) transitions within the fine structure of the fundamental excitonic line.²⁵ At room temperature, the relative strengths of these transitions (f_{π} , f_{σ_+} , and f_{σ_-}) depend on the size and geometry of the QD. The average Purcell factor experienced by a QD can be written as

$$F = \sum_{\chi \in \{\pi, \sigma_+, \sigma_-\}} f_{\chi} F_{\chi}(r, \vec{\Omega}), \quad (3.3)$$

where r stands for the distance of the QD to the cavity center and $\vec{\Omega} = (\theta, \varphi)$ for the orientation of the QD c -axis with respect to the z -axis of the cavity. The analysis can be greatly simplified if one neglects the mode profile difference between the x - and y -polarized TM_{111} modes (see Fig. 3.11), i.e. one assumes that $F_x \approx F_y$ and that a linear dipole vibrating in the xy -plane experiences a Purcell enhancement $F_{\parallel} = (F_x + F_y)/2$ while a linear

dipole vibrating in the z -axis direction experiences a Purcell enhancement $F_{\perp} = F_z$. With this simplification, F_{χ} does *not* depend on the azimuthal angle φ and (see Appendix A.2)

$$F_{\pi}(r, \theta) = F_{\parallel}(r) \sin^2 \theta + F_{\perp}(r) \cos^2 \theta \quad (3.4a)$$

$$F_{\sigma_{\pm}}(r, \theta) = \frac{1}{2} [F_{\parallel}(r)(1 + \cos^2 \theta) + F_{\perp}(r) \sin^2 \theta] \quad (3.4b)$$

Because of the spatial dependence of $F_{\parallel}(r)$ and $F_{\perp}(r)$ and random orientation of the c -axis of the QDs, the spontaneous decay from a monolayer of QDs is expected to be highly multi-exponential. Consider the emission from a QD at a distance r from the cavity center. In order to take into account the random direction of its c -axis, any emission-related property would have to be averaged. Assuming a uniform statistical distribution of c -axis directions, the orientation average reads:

$$\langle \dots \rangle_{\theta} = \int_0^{\frac{\pi}{2}} \dots \sin \theta \, d\theta = \int_{F_{\min}}^{F_{\max}} \dots P_{\chi}(F; r) \, dF, \quad (3.5)$$

where $P_{\chi}(F; r)$ is the statistical distribution of the Purcell factor resulting from the random distribution of the polar angle θ , $F_{\min} = \min [F_{\parallel}(r), F_{\perp}(r)]$, and $F_{\max} = \max [F_{\parallel}(r), 1/2 (F_{\parallel}(r) + F_{\perp}(r))]$. The distribution $P_{\chi}(F; r)$ can be deduced from the functional relationship between F and θ in Eqs. 3.4. It depends on whether the emission is a π or σ transition:

$$P_{\pi}(F; r) = \frac{1}{2} [(F_{\parallel}(r) - F_{\perp}(r)) (F_{\parallel}(r) - F)]^{-\frac{1}{2}} \quad (3.6a)$$

$$P_{\sigma_{\pm}}(F; r) = [(F_{\parallel}(r) - F_{\perp}(r)) (F_{\parallel}(r) + F_{\perp}(r) - 2F)]^{-\frac{1}{2}}. \quad (3.6b)$$

Fig. 3.12a compares the distributions $P_{\pi}(F; r)$ and $P_{\sigma_{\pm}}(F; r)$ for a QD located in the center of a nanopatch cavity of height $H = 130$ nm and radius $R = 200$ nm and for a QD located 180 nm away from the center. The understanding of the emission from a circular QDs monolayer of radius $R_{\text{ml}} \leq R$ (see Fig. 3.4) requires an additional spatial-averaging step

$$\langle \dots \rangle_r = \frac{2}{R_{\text{ml}}^2} \int_0^{R_{\text{ml}}} \dots r \, dr. \quad (3.7)$$

Fig. 3.12b shows the space-averaged Purcell factor distributions $P_{\pi}(F) = \langle P_{\pi}(F; r) \rangle_r$ and $P_{\sigma_{\pm}}(F) = \langle P_{\sigma_{\pm}}(F; r) \rangle_r$ for a monolayer of QDs filling a

nanopatch cavity of height $H = 130$ nm and radius $R = 200$ nm ($R_{\text{ml}} = R$). Despite qualitative differences, both distributions span a broad range of Purcell factors ranging from 1 to 7.4, have the same average value $\bar{F} = \bar{F}_\pi = \bar{F}_{\sigma_\pm} = 3.4$, and are expected to result in very similar non-exponential decay traces.

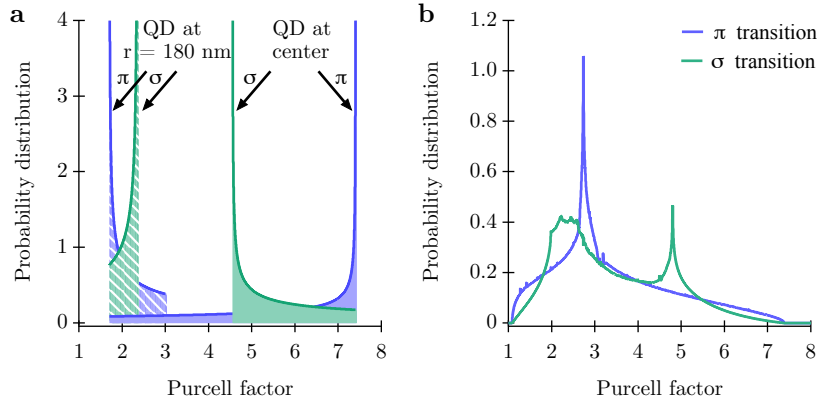


Figure 3.12: (a) Statistical distributions of the Purcell factor $P_\pi(F; r)$ and $P_{\sigma_\pm}(F; r)$ for a QD in the center of a nanopatch cavity of height $H = 130$ nm and radius $R = 200$ nm, and 180 nm away from the center. (b) Statistical distributions of the Purcell factor $P_\pi(F)$ and $P_{\sigma_\pm}(F)$ in a monolayer of QDs filling the same nanopatch cavity.

3.4 Measurements and results

Our CdSe/CdS core/shell QDs have a peak emission at 630 nm and a luminescence quantum yield of 60–75 %. When dispersed in toluene (refractive index $n = 1.5$), the decay is almost single-exponential, see the black dots in Fig. 3.14a, with an average decay time $\bar{\tau}_{\text{tol}} = 40.7$ ns. We define the average decay time of a decay trace $I(t)$ as

$$\bar{\tau} = \frac{\int_0^\infty t I(t) dt}{\int_0^\infty I(t) dt}. \quad (3.8)$$

A bi-exponential fit (red trace in Fig. 3.14a) shows one principal (short) decay time $\tau_{\text{tol},1} = 33.0$ ns accounting for 4/5 of the decay and one secondary (long) decay time $\tau_{\text{tol},2} = 72.3$ ns accounting for 1/5 of the decay.

In a first experiment, we fabricated a reference sample with a monolayer of QDs embedded between two 60 nm layers of SiN_x. Since SiN_x has a higher index of refraction than toluene ($n = 1.86$), additional dielectric screening was expected to shorten the radiative decay time. Indeed, the radiative decay time $\tau(n)$ of a QD embedded in an homogeneous medium of index n is connected to the radiative decay time τ_0 of the QD in vacuum through the relation $\tau(n) = \tau_0 / (n |f_{LF}|^2)$, where

$$f_{LF}(n) = \frac{3 n^2}{\varepsilon + 2 n^2} \quad (3.9)$$

is the local field factor and ε the complex relative permittivity of the QD ($\varepsilon = 7.05 + i 0.06$ at 630 nm for our CdSe/CdS QDs). For this reason, a lifetime shortening by a factor $\tau(1.86)/\tau(1.5) = 0.5$ was expected, leading to bi-exponential decay, as in toluene, but with lifetimes $\tau_{\text{SiN}_x,1} = 16.5$ ns and $\tau_{\text{SiN}_x,2} = 36.1$ ns. This theoretical prediction is displayed by the dashed red line in Fig. 3.14a. The experimental decay trace from our sample is also shown in Fig. 3.14a (blue dots) for comparison. The agreement with the local field theory is very good, though not perfect. A bi-exponential fit (yellow plain trace in Fig. 3.14a) of the experimental data shows that the fast decay time is a bit smaller than expected ($\tau_{\text{SiN}_x,1} = 13.3$ ns) while the slow decay time is almost identical ($\tau_{\text{SiN}_x,2} = 39.5$ ns). This demonstrates that the Langmuir-Blodgett deposition of the QDs and their embedding in SiN_x does not significantly degrade the emission quantum yield. The average decay time of QDs embedded in SiN_x is $\bar{\tau}_{\text{SiN}} = 22.9$ ns.

The luminescence decay from the nanopatch cavities was investigated using a micro-photoluminescence setup (see Fig. 3.13). The excitation beam at 445 nm was produced by a PicoQuant LDH-D-C-440M laser diode. The laser diode operates in either cw or pulsed mode (in which case it produces short pulses of less than 100 ps at a variable repetition rate in the kHz-MHz range). The excitation beam was focused on the sample using a 100× Olympus objective lens and shaped using a digital micro-mirror device (Texas Instrument, 0.55" XGA 2x LVDS DMD) to allow custom excitation patterns (*e.g.* exciting a single micrometer-sized spot or the entire field of view). The luminescence was collected through the same objective lens and directed either to an imaging spectrometer (Andor Shamrock 330i) equipped with an EMCCD camera (Andor iXon DU897) or to a photon-timing setup consisting of a silicon photon-counting module (Perkin Elmer SPCM-AQRH-14) with a time resolution of about 500 ps and start-stop time correlator (PicoQuant, PicoHarp 300).

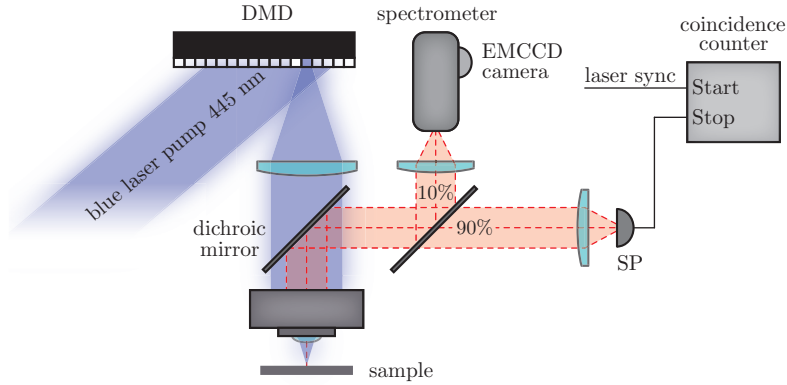


Figure 3.13: Micro-photoluminescence setup. The excitation beam at 445 nm is shaped by a DMD and then focused by an objective lens on the sample. The luminescence was collected through the same objective lens and directed either to an imaging spectrometer or to a photon-timing setup consisting of a silicon photon-counting module.

The inset of Fig. 3.14a shows the photoluminescence (PL) image of an array of nanopatch cavities under cw excitation as captured by the EMCCD camera. The sample consists of an array of cavities with the same height $H = 130$ nm, but different radii. When excited with short pulses at 445 nm, the PL of the QDs embedded in the nanopatch cavities produces highly non-exponential decay traces $I(t)$. The fastest decays were observed in cavities with radii $R = 260$, 270, and 280 nm; these are represented in Fig. 3.14a by green dots of different tones. For every cavity tested, the average decay time $\bar{\tau}$ ranged between 9.4 ns and 16.7 ns, see the blue data points in Fig. 3.14b. The cavity showing the strongest lifetime shortening ($\bar{\tau} = 9.4$ ns) had a radius $R = 270$ nm (light-green decay trace in Fig. 3.14a). According to simulations, the cavity radius realising the resonance condition was $R = 200$ nm. The discrepancy between the theory and experiment is due to the fact that the cavity height is difficult to control with an accuracy of 10 nm during the fabrication process and also difficult to estimate with that accuracy from the cavity cross-sections. According to Fig. 3.8a, the resonance condition for a cavity of radius $R = 270$ nm is fulfilled if the height is $H = 123$ nm. For that cavity height, the maximum Purcell enhancement F_{\parallel} in the center of the cavity would be slightly reduced (~ 6 instead of 7.4).

In order to compare the experimental decay traces to the theoretical one

expected for the optimal cavity design ($H = 130$ nm, $R = 200$ nm), we also plotted the decay

$$I_{\chi}(t) = \int I_{\text{SiN}_x} \left(t; \frac{\tau_{\text{SiN}_x,1}}{F}, \frac{\tau_{\text{SiN}_x,2}}{F} \right) P_{\chi}(F) dF + B \quad (3.10)$$

in Fig. 3.14a (dashed orange line), where $I_{\text{SiN}_x}(t; \tau_{\text{SiN}_x,1}, \tau_{\text{SiN}_x,2})$ is the bi-exponential fit to the decay data in SiN_x, $P_{\chi}(F)$ ($\chi \in \{\pi, \sigma_{\pm}\}$) are the Purcell factor distributions displayed in Fig. 3.12b, and $B = 10^{-3}$ a constant mimicking the experimental background noise. Remarkably, $I_{\pi}(t) \approx I_{\sigma_{\pm}}(t)$: the difference between the two functions is barely noticeable, resulting in a single characteristic non-exponential decay.

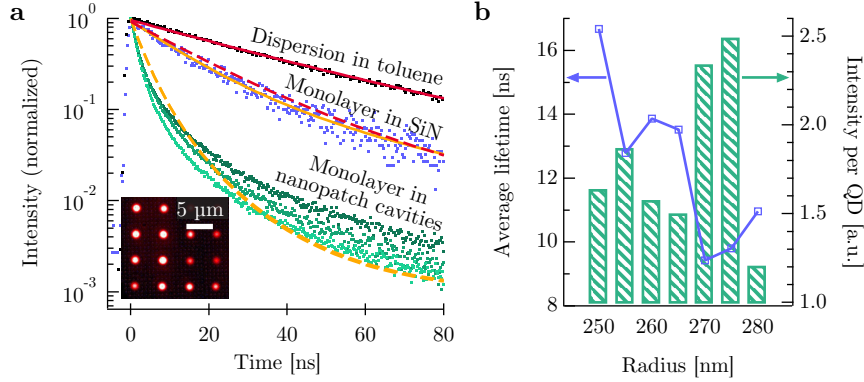


Figure 3.14: (a) PL decay traces from QDs embedded in nanopatch cavities of height $H = 130$ nm and radii $R = 260, 270,$ and 280 nm (green dots) show Purcell reduction of the luminescence decay time compared to: the same QDs suspended in toluene (black dots) and a monolayer of QDs embedded between two 60 nm thick layers of SiN_x (blue dots). The plain lines (red and yellow) are bi-exponential fits to the data. The dashed lines (red and yellow) are theoretical predictions (explanations in the text). Inset: PL image from an array of nanopatch cavities with height $H = 130$ nm under cw excitation at 445 nm. (b) Average PL decay times (blue squares) and PL intensity per QD (histogram) in nanopatch cavities as a function of the cavity radius R .

According to simulations, $\sim 60\%$ of the total energy radiated by a dipole located in the center of the cavity, where the coupling to the mainly vertical emitting TM mode is best, is radiative while the rest is dissipated. When pumped at 445 nm, the luminescence I of a nanopatch cavity is expected to

be proportional to the number of emitters N_{qd} in the cavity and inversely proportional to the emitter decay time. In Fig. 3.14b, we plotted the luminescence intensity per QD I/N_{qd} (histogram) as a function of the cavity radius. As expected, cavities with shorter decay times tend to emit more photons per QD. The product $I/N_{\text{qd}} \times \bar{\tau}$ is equal to 23.24 in average with a standard deviation of 1.9. However, some cavities showed less luminescence than expected, likely because of structural defects causing a less favourable balance between radiation and dissipation.

3.5 Conclusion

We have developed a straightforward fabrication method, based on e-beam lithography that allows a precise control on the positioning of emitter and cavity. More specifically we demonstrated that a uniform monolayer of colloidal QDs can be precisely positioned in the center of a sub-wavelength SiN_x/Au cavity, which can be further patterned down to a single QD in future experiments. However to develop such a single-photon source, it is crucial to study the SP properties of the emitter itself, to determine which kind of dots have superior SP properties (*e.g.* InP/ZnSe as shown in¹¹) and more importantly, which ones preserve these properties after embedding/-patterning them. As our fabrication method is compatible with any colloidal QD material, the final combination of the best emitter with our nanoptach cavities does not pose any additional challenges. Finally we have also studied and clarified the non-exponential behaviour of the decay traces when an emitter is placed off center or in the case of a film of multiple emitters. Although the speed-up of the spontaneous emission of these QD monolayers is modest, the expected radiative efficiency for these single-photon cavities is high compared to plasmonic cavities with stronger Purcell enhancement. The circular shape of our cavities, together with the mode profile of the targeted mode and the possibility to deterministically position both cavity and emitter allows for a robust and reproducible source. As the patterning and cavity fabrication can be seen as two independent fabrication steps with respective yields of 40% and 100%, we can estimate that the yield of these scalable single-photon sources can be up to 40%.

References

- [1] I. Aharonovich, D. Englund, and M. Toth, “Solid-state single-photon emitters,” *Nature Photonics*, vol. 10, p. 631, sep 2016.
- [2] N. Somaschi, V. Giesz, L. De Santis, J. C. Loredano, M. P. Almeida, G. Hornecker, S. L. Portalupi, T. Grange, C. Antón, J. Demory, C. Gómez, I. Sagnes, N. D. Lanzillotti-Kimura, A. Lemaitre, A. Auffeves, A. G. White, L. Lanco, and P. Senellart, “Near-optimal single-photon sources in the solid state,” *Nature Photonics*, vol. 10, pp. 340 EP –, 03 2016.
- [3] J. Claudon, J. Bleuse, N. S. Malik, M. Bazin, N. Gregersen, C. Sauvan, P. Lalanne, and Gerard, “A highly efficient single-photon source based on a quantum dot in a photonic nanowire,” *Nature Photonics*, vol. 4, no. March, pp. 174–177, 2010.
- [4] G. Juska, V. Dimastrodonato, L. O. Mereni, A. Gocalinska, and E. Pelucchi, “Towards quantum-dot arrays of entangled photon emitters,” *Nature Photonics*, vol. 7, pp. 527 EP –, 05 2013.
- [5] C. Schneider, T. Heindel, A. Huggenberger, P. Weinmann, C. Kistner, M. Kamp, S. Reitzenstein, S. Höfling, and A. Forchel, “Single photon emission from a site-controlled quantum dot-micropillar cavity system,” *Applied Physics Letters*, vol. 94, no. 11, p. 111111, 2009.
- [6] M. Arcari, I. Söllner, A. Javadi, S. Lindskov Hansen, S. Mahmoodian, J. Liu, H. Thyrrestrup, E. H. Lee, J. D. Song, S. Stobbe, and P. Lodahl, “Near-unity coupling efficiency of a quantum emitter to a photonic crystal waveguide,” *Phys. Rev. Lett.*, vol. 113, p. 093603, Aug 2014.
- [7] G. Kirsanske, H. Thyrrestrup, R. S. Daveau, C. L. Dreeßen, T. Pregnolato, L. Midolo, P. Tighineanu, A. Javadi, S. Stobbe, R. Schott, A. Ludwig, A. D. Wieck, S. I. Park, J. D. Song, A. V. Kuhlmann, I. Söllner, M. C. Löbl, R. J. Warburton, and P. Lodahl, “Indistinguishable and efficient single photons from a quantum dot in a planar nanobeam waveguide,” *Phys. Rev. B*, vol. 96, p. 165306, Oct 2017.
- [8] T. B. Hoang, G. M. Akselrod, and M. H. Mikkelsen, “Ultrafast room-temperature single photon emission from quantum dots coupled to plasmonic nanocavities,” *Nano Letters*, vol. 16, pp. 270–275, 2016.
- [9] C. Belacel, B. Habert, F. Bigourdan, F. Marquier, J.-P. Hugonin, S. Michaelis de Vasconcellos, X. Lafosse, L. Coolen, C. Schwob, C. Javaux, B. Dubertret, J.-J. Greffet, P. Senellart, and A. Maitre,

- “Controlling spontaneous emission with plasmonic optical patch antennas,” *Nano Letters*, vol. 13, no. 4, pp. 1516–1521, 2013.
- [10] M. Cirillo, T. Aubert, R. Gomes, R. Van Deun, P. Emplit, A. Biermann, H. Lange, C. Thomsen, E. Brainis, and Z. Hens, ““flash” synthesis of cdse/cds core-shell quantum dots,” *Chemistry of Materials*, vol. 26, no. 2, pp. 1154–1160, 2014.
- [11] V. Chandrasekaran, M. D. Tessier, D. Dupont, P. Geiregat, Z. Hens, and E. Brainis, “Nearly blinking-free, high-purity single-photon emission by colloidal inp/znse quantum dots,” *Nano Letters*, vol. 17, no. 10, pp. 6104–6109, 2017.
- [12] K. Lambert, R. K. Capek, M. I. Bodnarchuk, M. V. Kovalenko, D. Van Thourhout, W. Heiss, and Z. Hens, “Langmuir-schaefer deposition of quantum dot multilayers,” *Langmuir*, vol. 26, no. 11, pp. 7732–7736, 2010.
- [13] W. Xie, R. Gomes, T. Aubert, S. Bisschop, Y. Zhu, Z. Hens, E. Brainis, and D. Van Thourhout, “Nanoscale and single-dot patterning of colloidal quantum dots,” *Nano Letters*, vol. 15, no. 11, pp. 7481–7487, 2015.
- [14] T. B. Hoang, G. M. Akselrod, C. Argyropoulos, J. Huang, D. R. Smith, and M. H. Mikkelsen, “Ultrafast spontaneous emission source using plasmonic nanoantennas,” *Nature Communications*, vol. 6, p. 7788, 2015.
- [15] P. Kolchin, N. Pholchai, M. H. Mikkelsen, J. Oh, S. Ota, M. S. Islam, X. Yin, and X. Zhang, “High purcell factor due to coupling of a single emitter to a dielectric slot waveguide,” *Nano Letters*, vol. 15, no. 1, pp. 464–468, 2014.
- [16] A. Kinkhabwala, Z. Yu, S. Fan, Y. Avlasevich, K. Müllen, and W. Moerner, “Large single-molecule fluorescence enhancements produced by a bowtie nanoantenna,” *Nature Photonics*, vol. 3, no. 11, pp. 654–657, 2009.
- [17] J. T. Choy, B. J. Hausmann, T. M. Babinec, I. Bulu, M. Khan, P. Maletinsky, A. Yacoby, and M. Loncar, “Enhanced single-photon emission from a diamond-silver aperture,” *Nature Photonics*, vol. 5, no. 12, pp. 738–743, 2011.
- [18] K. Yu, A. Lakhani, and M. C. Wu, “Subwavelength metal-optic semiconductor nanopatch lasers,” *Optics Express*, vol. 18, pp. 8790–8799, Apr 2010.

-
- [19] W. Xie, Y. Zhu, T. Aubert, S. Verstyft, Z. Hens, and D. V. Thourhout, “Low-loss silicon nitride waveguide hybridly integrated with colloidal quantum dots,” *Opt. Express*, vol. 23, pp. 12152–12160, May 2015.
- [20] W. Xie, Y. Zhu, S. Bisschop, T. Aubert, Z. Hens, D. van Thourhout, and P. Geiregat, “Colloidal quantum dots enabling coherent light sources for integrated silicon-nitride photonics,” *IEEE Journal of Selected Topics in Quantum Electronics*, vol. 23, pp. 1–13, Sept 2017.
- [21] I. Moreels, G. Allan, B. De Geyter, L. Wirtz, C. Delerue, and Z. Hens, “Dielectric function of colloidal lead chalcogenide quantum dots obtained by a Kramers-Krönig analysis of the absorbance spectrum,” *Physical Review B*, vol. 81, p. 235319, jun 2010.
- [22] M. Alves-Santos, R. D. Felice, and G. Goldoni, “Dielectric functions of semiconductor nanoparticles from the optical absorption spectrum: The case of cdse and cds,” *The Journal of Physical Chemistry C*, vol. 114, no. 9, pp. 3776–3780, 2010.
- [23] C. A. Balanis, *Advanced Engineering Electromagnetics*. Wiley NewYork, 1989.
- [24] C. Manolatu and F. Rana, “Subwavelength nanopatch cavities for semiconductor plasmon lasers,” *IEEE Journal of Quantum Electronics*, vol. 44, pp. 435–447, May 2008.
- [25] I. Chung, K. T. Shimizu, and M. G. Bawendi, “Room temperature measurements of the 3d orientation of single cdse quantum dots using polarization microscopy,” *Proceedings of the National Academy of Sciences*, vol. 100, no. 2, pp. 405–408, 2003.

4

The impact of core/shell geometry on the optical gain characteristics of CdSe/CdS QDs

After the first demonstrations of optical gain in colloidal QDs, several efforts have been made to improve the overall lasing performance of these materials. Although this optimization mainly focused on strategies that reduce the gain threshold, the role of the gain coefficient to reach lasing action should not be overlooked. Here, we address both the relation between the structure of CdSe/CdS core/shell QDs, their optical gain – which we quantify as the material gain – and their threshold needed to attain net stimulated emission. We analyzed these relations by means of transient absorption spectroscopy and show that large core/thin shell QDs combine a larger material gain with a lower threshold electron-hole pair occupation and a long gain window. These insights are most valuable to guide future work to improve colloidal QDs for optical gain applications and develop optimized QD-lasers.

4.1 Introduction

Optical gain in quasi-spherical colloidal semiconductor nanocrystals or quantum dots (QDs) was demonstrated shortly after the development of synthesis methods that yielded monodisperse QD dispersions.¹ Since QDs combine size-tunable optical properties with a suitability for solution-based processing, they are highly attractive nanomaterials for optical amplifiers and lasers.^{2;3} Soon after the first successful demonstration of optical gain in colloidal QDs¹, their integration within dielectric host materials to make optically pumped solid-state QD-lasers became a subject of intense research and several research groups were able to demonstrate lasing action under pulsed optical excitation using different cavity designs⁴⁻⁶. Follow-up efforts have resulted in considerable improvements in the overall lasing performance by reducing the lasing threshold, but it was not until recently that also (quasi-) continuous-wave lasing devices were demonstrated.^{7;8}

The step towards actual device development leads almost naturally to the question of optimization, *i.e.*, the development of QD-lasers featuring, for example, a minimized pumping threshold or footprint. Meaningful optimization, however, requires (1) a framework that translates optical gain by quantum dots into a measurable and reproducible quantity, (2) a microscopic model that links optical gain to the opto-electronic properties – and thus the structure – of individual QDs, and (3) device-level simulations to model and quantify lasing action. In literature, especially the second point has been deeply studied from the perspective of the population inversion lifetime. Early work on CdSe-based QDs showed that net optical gain results from so-called biexcitons, which recombine rapidly through non-radiative Auger processes.⁹ Especially in the case of CdSe/CdS core/shell QDs, it proved possible to limit Auger recombination rates by developing thick shell QDs with an alloyed core/shell interface.¹⁰⁻¹⁴ These results paved the way for the development of QD-based lasers that work under nanosecond and continuous-wave optical pumping.^{7;8} The role of Auger recombination was further addressed recently at the level of device simulations by Park *et al.*¹⁵ These authors use a simplified model of QDs featuring 2-fold degenerate band-edge states to link a reduction of the Auger recombination rate to a lowering of lasing thresholds under pulsed and continuous-wave optical pumping.

The initial reports on optical gain by QDs expressed the condition to reach stimulated emission in a QD-based material in terms of the Auger recombination rate and the gain coefficient of the material. Whereas, as dis-

cussed above, the development of QDs optimized for lasing applications has mainly focused on strategies to reduce Auger recombination, the recent development of integrated microlasers based on CdSe/CdS core/shell QDs highlighted the role of the gain threshold to reach lasing action.^{16;17} In this case, lasing could only be attained in sufficiently large resonators, in which the modal gain could counter the optical losses. Therefore, when optimizing a gain material, the quantitative gain of the material must be addressed next to the lasing threshold and the population inversion lifetime. Returning to the optimization problem, this raises the question as to how optical gain by QDs is best quantified, and how gain coefficients are related to the QD's structure and opto-electronic properties. Take for example the case of films of core/shell QDs shown in Fig. 4.1, where an increase of the shell volume will always come at the cost of a diluted core concentration for a given core size. Since stimulated emission comes from core-related transitions, one expects a concomitant reduction of the gain coefficient of the film. At the same time, since less electron-hole pairs need to be created per unit volume, more voluminous shells could make for lower lasing thresholds, in particular when the shell can absorb pump light. Until now, however, such tradeoffs have not been experimentally verified, let alone that they have been exploited to optimize QD-lasers.

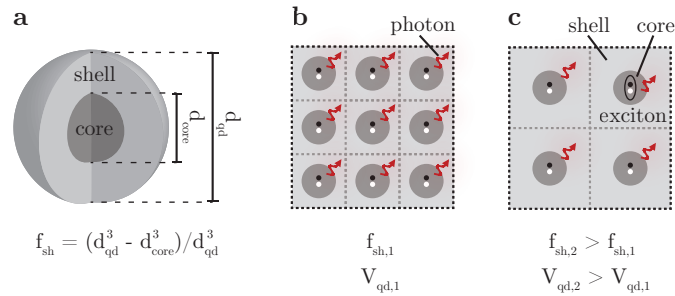


Figure 4.1: (a) Schematic representation of a core/shell QD (b) Cartoon of a film consisting of densely packed (volume fraction $f = 1$) core/shell QDs. For simplicity, shells have been given a square geometry and electron-hole pairs are depicted by a combination of a black and a white circle. (c) Same volume filled with core/shell QDs, that have an identical core as in (b) but a thicker shell ($f_{\text{sh},2} > f_{\text{sh},1}$) and thus a larger total volume ($V_{\text{qd},2} > V_{\text{qd},1}$). The figure clarifies the effects of dilution (less core QDs per unit volume) leading to a lower gain coefficient and a possibly lower gain threshold.

Here, we address the relation between the structure of CdSe/CdS core/shell

QDs, their optical gain – which we quantify as the material gain – and the threshold needed to attain net stimulated emission. We first build on the simplified electronic structure model introduced by Park *et al.*¹⁵ to show that increasing the shell-to-total-QD volume fraction should markedly reduce the gain threshold when pumping at photon energies above the band gap of the shell, at the expense of a markedly lower material gain. We analyze these predictions by means of transient absorption spectroscopy on dispersions of CdSe/CdS QDs with different core-shell geometries. It follows that thin shell QDs indeed feature the highest gain coefficients. On the other hand, the significant threshold reduction expected for more voluminous QDs is absent. In fact, the thresholds of small-core/thick-shell QDs were found to be higher than for core/shell QDs with thinner shells. Using a QD model to simulate the QD gain spectrum, we show that this increasing gain thresholds for thicker-shell QDs finds its origin in a varying exciton-exciton Coulomb interaction, which shifts from attractive for CdSe/CdS QDs with a thin shell to repulsive for thick-shell QDs. Such shifts greatly influence the gain threshold, up to the point where large-core/thin-shell QDs, which exhibit a redshifted biexciton transition, are the overall champion core/shell configuration in terms of both material gain and gain threshold.

4.2 Background

4.2.1 Material gain

To compare the performance of different core/shell QDs as gain material, we use the material gain g_i as a quantitative measure of optical gain. To define this material gain, we start from the notion that the absorption coefficient of a composite material consisting of QDs dispersed in a non-absorbing medium can be seen as the product of the QD volume fraction f , *i.e.*, the ratio between the total QD volume and the sample volume, and the intrinsic absorption coefficient μ_i of the QDs:¹⁸

$$\mu = \mu_i f \quad (4.1)$$

Defined according to Eq. (4.1), μ_i is the absorption coefficient of a fictitious QD dispersion that has a QD volume fraction of 1. Defining an intrinsic absorption coefficient is a way of normalizing the absorbance A , and turn it into a material property that is independent of the sample thickness L and QD volume fraction f .

$$\mu_i = \frac{A_0}{L f} \ln 10 \quad (4.2)$$

Here, A_0 is the absorbance and L the thickness of the QD sample analyzed. In principle, size quantisation makes μ_i dependent on the wavelength and the size of the QDs. However, it was found that μ_i becomes size-independent at short wavelengths, with an experimental value closely matching the value predicted by Maxwell-Garnett theory based on the bulk dielectric function of the QD material.¹⁸ Hence, using μ_i and A_0 at such a reference wavelength, any absorbance spectrum $A(\lambda)$ can be normalized to obtain the spectrum of the intrinsic absorption coefficient:

$$\mu_i(\lambda, t) = \frac{A(\lambda, t)}{A_0(\lambda_{\text{ref}})} \mu_i(\lambda_{\text{ref}}) \quad (4.3)$$

In the case that a QD dispersion exhibits optical gain, for example following optical excitation by a femtosecond laser pulse, the same normalization procedure can be applied to the absorbance $A = \Delta A + A_0$ at any moment after photoexcitation. Since optical gain yields a negative absorbance, we define the QD material gain g_i as:

$$g_i(\lambda, t) = -\frac{A(\lambda, t)}{A_0(\lambda_{\text{ref}})} \mu_i(\lambda_{\text{ref}}) \quad (4.4)$$

Hence, g_i represents the gain a QD material with a QD volume fraction $f = 1$ would have under the same conditions of optical pumping as the actual sample, and the product of g_i and f yields the gain of any QD sample. Hence, our rephrasing of the intrinsic gain coefficient as the material gain. In addition, it is exactly this non-linear absorbance A that we can measure using transient absorption spectroscopy (TAS). As it can be measured directly on a colloidal dispersion, the material gain is a most useful characteristic of colloidal QDs that can be used to quantify gain and compare gain in different structures and material systems.

4.2.2 Influence of core/shell morphology

To estimate what influence the shell volume can have on the gain characteristics of CdSe/CdS QDs, we analyzed the relation between the material gain and the core/shell morphology starting from a core/shell model system. As shown in Figure 4.2, we assumed that stimulated emission was related to a transition between a g_e -fold degenerate upper state (conduction-band edge) and a g_h -fold degenerate lower state (valence-band edge) in the core QD. Furthermore, we discarded spectral shifts and we assumed that the oscillator strength of the band-edge transition is independent of the level occupation.

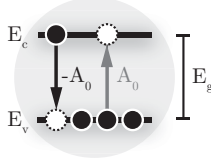


Figure 4.2: Representation of a QD core as a 2-level system featuring a $g_h = 4$ and $g_e = 2$ fold degenerate valence and conduction band edge.

In that case, the absorbance $\mathcal{A}(N_e, N_h)$ of light by the band-edge transition of a QD containing N_e band-edge electrons and N_h band-edge holes can be written as a fraction of the band-edge absorbance A_0 by unexcited QDs:

$$\mathcal{A}(N_e, N_h) = \left(1 - \frac{N_e}{g_e}\right) \left(1 - \frac{N_h}{g_h}\right) A_0 \quad (4.5)$$

In the same way, stimulated emission of light by this transition will result in an amplification $\mathcal{G}(N_e, N_h)$ given by:

$$\mathcal{G}(N_e, N_h) = \frac{N_e}{g_e} \frac{N_h}{g_h} A_0 \quad (4.6)$$

Note that N_e and N_h need not be identical. Especially at non-resonant excitation, electrons and holes can also occupy higher energy states, which makes different occupations of the band-edge states possible. Combining Eqs. (4.5) and (4.6), the net absorbance $A(N_e, N_h)$ is obtained as:

$$A(N_e, N_h) = \mathcal{A}(N_e, N_h) - \mathcal{G}(N_e, N_h) = \left(1 - \frac{N_e}{g_e} - \frac{N_h}{g_h}\right) A_0 \quad (4.7)$$

In the case of a QD ensemble containing on average $\langle N \rangle$ electron-hole pairs, the net absorbance $A(\langle N \rangle)$ can be seen as the sum of the absorbance of QDs containing 0, 1, 2, ..., electron hole pairs. Writing the probability that a QD contains N electron-hole pairs as $P(N)$, we thus have:

$$A(\langle N \rangle) = \sum_{N=0}^{\infty} P(N) \left(1 - \frac{N_e(N)}{g_e} - \frac{N_h(N)}{g_h}\right) A_0 \quad (4.8)$$

Here, we took $N_e(N)$ and $N_h(N)$ identical to N as long as the occupancies are smaller than or equal to g_e and g_h , respectively, whereas they were set equal to these respective degeneracies for larger N . In the case that electron-hole pairs are created by femtosecond pulsed excitation, $P(N)$ can

be described by a Poisson distribution as long as delays short as compared to multi-exciton lifetimes are considered. If we then represent the A_0 -spectrum of the band-edge transition by a single Gaussian with central energy E_g , the corresponding non-linear absorbance $A(\langle N \rangle)$ can be readily calculated using Eq. (4.8). The resulting normalized spectra are shown in Figure 4.3a, where $A > 0$ corresponds to net absorbance (grey area) while $A < 0$ corresponds to net stimulated emission. Figure 4.3b represents $-A/A_0$ at the band gap energy E_g , from which one can see that increasing $\langle N \rangle$ first leads to a linear reduction of the absorbance, after which a regime of net gain is reached at $\langle N \rangle = 1.54$. Finally, the normalized amplification levels off at 1 at high exciton populations, so the maximum gain equals the original absorbance when the system is completely inverted. Based on this result, the maximum attainable gain $g_{i,\max}$ can be written as:

$$g_{i,\max}(\lambda) = \frac{A_0(\lambda)}{A_0(\lambda_{\text{ref}})} \mu_i(\lambda_{\text{ref}}) \quad (4.9)$$

In what follows, we will use this equation to estimate the effect of the core and shell volumes on $g_{i,\max}$. To focus on the main trends, this involves a zero order approximation where we assume that the absorbance $A_0(\lambda)$ due to the band-edge transition scales with the core volume and is not affected by the presence of the shell.

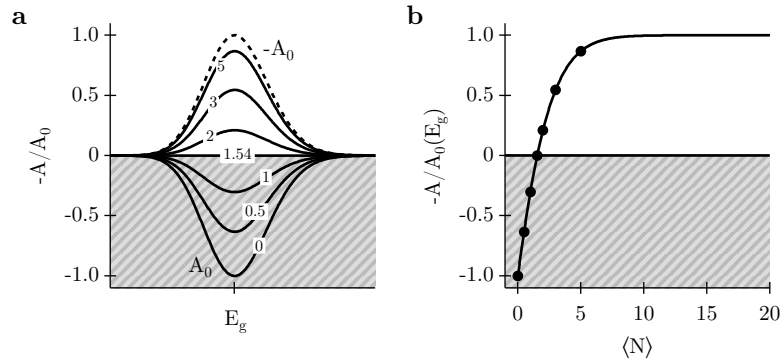


Figure 4.3: (a) $-A/A_0$ - spectra as a function of E for various electron-hole pair occupation numbers $\langle N \rangle$. (b) Variation of $-A/A_0$ - spectra at E_g with $\langle N \rangle$, showing the gain threshold $\langle N \rangle_{\text{th}} = 1.54$ and saturation value $A = -A_0$.

Focusing on $g_{i,\max}$ first, the point is that optical pumping is possible through higher energy transitions that can involve initial and final states in the shell.

Hence, upon increasing the shell thickness for a given core diameter, the ratio $A_0(\lambda)/A_0(\lambda_{\text{ref}})$ will scale as $V_c/V_{\text{qd}} = 1 - f_{\text{sh}}$ once λ_{ref} is a wavelength shorter than the band-gap of the shell. Here, V_{qd} refers to the total QD volume, V_c to the core volume and f_{sh} is the volume fraction of the shell. Figure 4.4 shows μ_i , calculated according to Maxwell-Garnett theory, of CdSe/CdS QDs at a reference wavelength $\lambda_{\text{ref}} = 350$ nm as a function of f_{sh} . One sees that at such a wavelength, which is shorter than the shell band-edge transition, $\mu_i(\lambda_{\text{ref}})$ is largely independent of the dimensions of core and shell. Hence, the same scaling with $1 - f_{\text{sh}}$ that we put forward for $A_0(\lambda)/A_0(\lambda_{\text{ref}})$, will apply to $g_{i,\text{max}}$. As shown in Figure 4.5a, we thus expect $g_{i,\text{max}}$ to go down with increasing shell thickness for a given core QD, up to the point where it vanishes for $f_{\text{sh}} \rightarrow 1$.

In view of gain thresholds, Figures 4.3a and b indicate that transparency is reached when $\langle N \rangle_{\text{th}} = 1.54$ for the case that $g_e = 2$ and $g_h = 4$. Importantly, this number only depends on the degeneracy of the band-edge states, and is therefore independent of the presence or not of any shell around the initial core QD. At the same time, the average number of electron-hole pairs $\langle N \rangle$ that is created per QD by a given photon flux scales with the absorption cross section σ of the QDs at the pump wavelength. Since σ is given by the product $\mu_i \times V_{\text{qd}}$, it follows that the photon flux needed to reach this threshold occupation will scale inversely with V_{qd} . This conclusion can be extended to core/shell QDs, provided that excitation wavelengths shorter than the shell band-gap transition are used. As shown in Figure 4.5b, we thus expect lower lasing thresholds for the most voluminous QDs when such pump wavelengths are used.

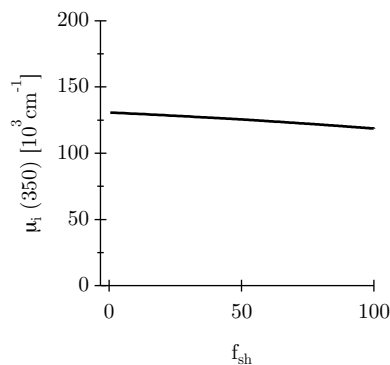


Figure 4.4: μ_i at $\lambda = 350$ nm versus f_{sh} , as predicted by the Maxwell-Garnett (MG) theory.

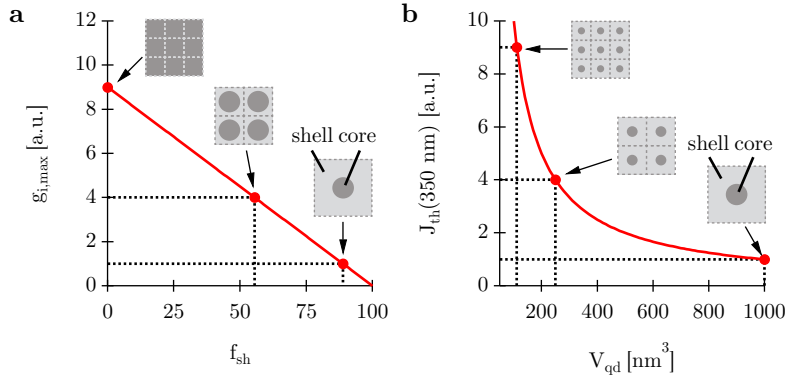


Figure 4.5: (a) Theoretically predicted $g_{i,max}$ as a function of f_{sh} for fixed core size. (b) Theoretically predicted J_{th} as a function of V_{qd} for fixed shell volume fraction.

4.3 Experimental results

To assess the relations put forward between the morphology of core/shell QDs and their optical gain characteristics, we analyzed a set of 7 CdSe/CdS core/shell QDs that each have a different combination of volume V_{qd} and shell volume fraction f_{sh} (see Table 4.1 and Fig. A.1). All samples consisted of oleate-capped core/shell QDs synthesized using a seeded-growth *flash* method as previously described in the literature.^{19;20} Specific to this synthesis is that CdS shells are rapidly grown around wurtzite CdSe core QDs by heterogeneous nucleation at high temperature. The approach enabled us to change the core/shell morphology by simply varying the size of the injected core QDs and adapting the amount of Cd and S precursor used for shell growth. The resulting QDs feature an alloyed CdSe/CdS interface,¹⁹ which can mitigate strain and slow down non-radiative Auger recombination of multi-excitons^{11;12;21}

4.3.1 Spectroscopic characteristics

Figure 4.7a presents an overview of the absorption and photoluminescence spectra of all 7 samples used in this study. Note that the sample color code introduced in Fig. 4.7a will be used in all the following figures. In all cases, the absorption spectra exhibit a pronounced shell-enhanced absorption at wavelengths shorter than the CdS bulk bandgap of ~ 520 nm (see Fig. 4.7b),

Table 4.1: Morphological descriptors d_c , d_{qd} and f_{sh} of the different CdSe/CdS QD samples used for this study. The radiative lifetimes τ_X extracted from the fits on the PL time traces in Fig. 4.6.

Sample	d_c [nm]	d_{qd} [nm]	f_{sh}	τ_X [ns]
S1	4.0	7.3	84	15.1
S2	4.0	9.0	92	18.1
S3	2.9	8.6	96	16.0
S4	2.9	9.4	97	24.0
S5	2.4	10.1	99	30.9
S6	2.9	11.0	98	43.4
S7	2.3	11.8	99	54.2

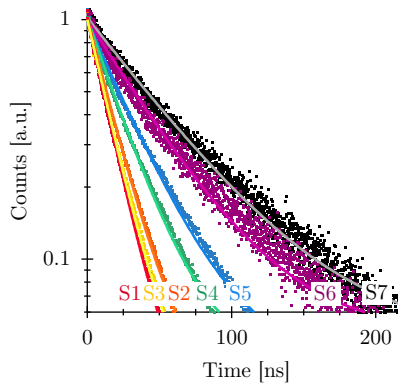


Figure 4.6: Measured PL-time traces, fitted with a single exponential. The resulting τ_X -values are given in Table 4.1.

whereas various features that are characteristic of transitions within the core CdSe QDs can be seen at wavelengths longer than the CdS bulk bandgap. These features can be traced back more readily by means of the second derivative of the absorbance spectrum, which is shown in Fig. 4.7c for the case of sample S1. Here, the most relevant features have been assigned according to literature.²² The emission of the different samples has a central wavelength that varies between 610 – 625 nm and features a full-width at half-maximum (FWHM) ranging between 25 – 48 nm, depending on core size and shell thickness. Such values are typical for colloidal CdSe/CdS QDs. The quantum yield is about 30 – 45% and the radiative lifetimes range between 15 – 54 ns, where bigger nanocrystals have the longest lifetimes (see

Fig. 4.6 and Table 4.1).

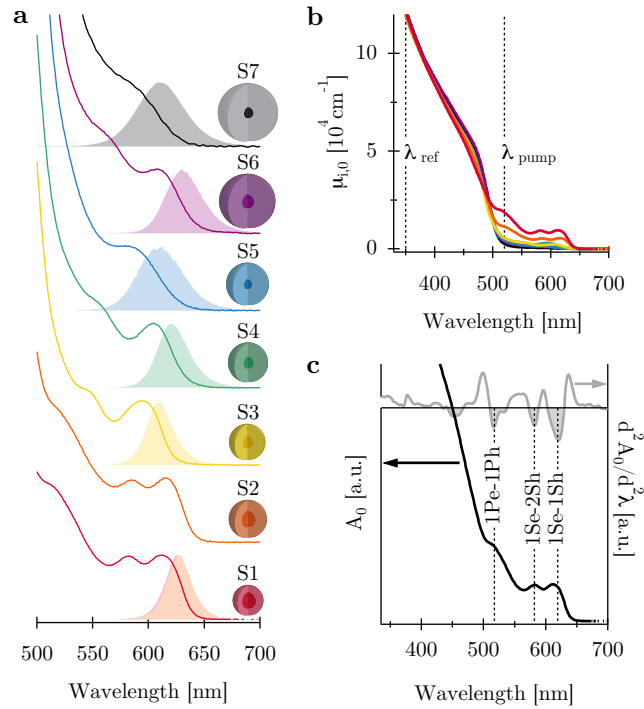


Figure 4.7: (a) Overview of absorption and PL-spectra for the different CdSe/CdS core/shell samples S1-S7. See Table 4.1 for an overview of core and total diameters, and shell volume fraction. (b) $\mu_{i,0}$ -spectra, calculated using Eq. (4.3) and the measured A_0 -spectra. (c) A_0 -spectrum (black) of sample S1 and second derivative (grey), with the assignment of the most relevant absorption features as the $1S_e - 1S_h$, $1S_e - 2S_h$ and $1P_e - 1P_h$ transitions.

To quantify stimulated emission by CdSe/CdS QDs, we determined the non-linear absorbance $A(\lambda)$ of the different QD dispersions using pump-probe transient absorption spectroscopy (TAS). For this, stirred dispersions were excited using a 110 fs pump pulse and the change in absorbance ΔA was measured as a function of the probe wavelength and the pump-probe delay. Figure 4.8a shows such a 2D transient absorption map recorded on sample S1 dispersed in toluene, when pumped with 520 nm light at a pump energy fluence of 0.73 mJ/cm^2 . The map is characterized by a pronounced bleach of the absorbance ($\Delta A < 0$) at wavelengths corresponding to the different core related transitions. In line with literature, we attribute this to filling of the band-edge states with photogenerated electrons and holes, and the gradual reduction of the bleach signal is then indicative of the recombination of photo-excited electron-hole pairs.²²

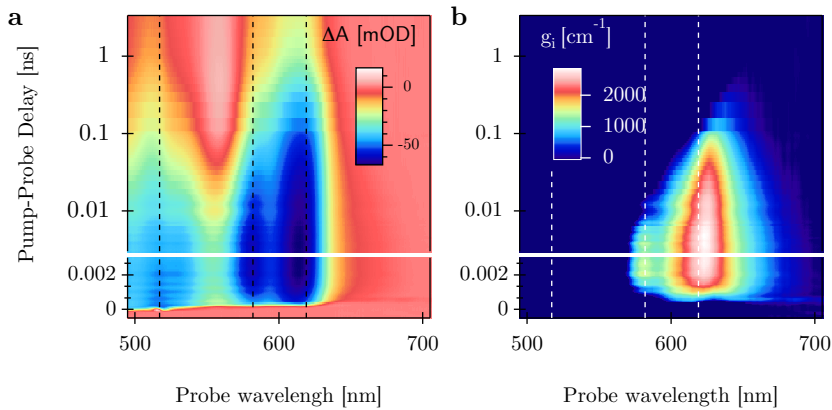


Figure 4.8: (a) Time-wavelength map of the differential absorbance for the same sample. The sample was pumped with an energy fluence of 0.73 mJ/cm^2 and wavelength 520 nm. (b) The concomitant map of the material gain calculated using Eq. (4.3), showing a material gain up to 2800 cm^{-1} . Vertical dashed lines indicate $1S_e - 1S_h$, $1S_e - 2S_h$ and $1P_e - 1P_h$ transitions.

By adding the linear absorbance A_0 to the transient absorbance ΔA , we obtained the non-linear absorbance A of the CdSe/CdS QDs after photoexcitation as a function of wavelength and pump-probe delay. In the resulting non-linear absorbance map, areas where $A > 0$ point to remaining absorption after photoexcitation, whereas a negative absorbance $A < 0$ is indicative of optical gain. As outlined in the background section, such a non-linear

absorbance map can be rescaled to a map of the material gain g_i , which is an intrinsic material property that enables optical gain by different samples to be compared on the same footing. Figure 4.8b shows the material gain map that corresponds to the ΔA map shown in Fig. 4.8a. It can be seen that especially around the band-edge transition, the aforementioned bleach feature reflects a situation of optical gain. More specifically, we find that the used conditions of optical pumping lead to a gain band that is more than 100 nm wide, centred around the first $1S_e - 1S_h$ transition, and that lasts up to 600 ps. Moreover, we find a maximum material gain in this case of 2800 cm^{-1} .

To study the time constants of the decay of the photo-excited state, we analyzed the non-linear absorbance at the band-edge as a function of pump-probe delay for different pump powers. To obtain the lifetime of the various multi-exciton states, we fitted such decay traces to a sum of exponentials, while constraining the decay rates such that they reflect the known scaling of Auger recombination rates with the exciton number. To determine the biexciton lifetime, a pump fluence is chosen such that $\langle N \rangle \leq 1$ at $t = 0$. This way the probability to have more than 4 excitons, $P(N \geq 4) = 0.019$, is negligible compared to the probabilities to have $N = 0, 1, 2$ or 3 excitons. Figure 4.9 shows such time-slices for sample S1. These time traces can be fitted with a sum of three exponentials:

$$I(t) = A_1 \exp\left(\frac{-t}{\tau_1}\right) + A_2 \exp\left(\frac{-t}{\tau_2}\right) + A_3 \exp\left(\frac{-t}{\tau_3}\right) \quad (4.10)$$

However, since the ratios of the bi- and tri-exciton to single exciton population scale according to $P(N = 2)/P(N = 1) = \langle N \rangle/2$ and $P(N = 3)/P(N = 1) = \langle N \rangle^2/6$ respectively, Eq. (4.10) becomes:

$$I(t) = A_1 \exp\left(\frac{-t}{\tau_1}\right) + \frac{\langle N \rangle}{2} A_1 \exp\left(\frac{-t}{\tau_2}\right) + \frac{\langle N \rangle^2}{6} A_1 \exp\left(\frac{-t}{\tau_3}\right) \quad (4.11)$$

In addition, the multiparticle relaxation times scale cubic with respect to the carrier density,⁹ progressively becoming faster as the number of $e-h$ pairs per dot increases. Hence, $\tau_3/\tau_2 = 2^2/3^2 = 0.44$, resulting in a fit function with only 3 independent fitting coefficients

$$I(t) = A_1 \exp\left(\frac{-t}{\tau_1}\right) + \frac{\langle N \rangle}{2} A_1 \exp\left(\frac{-t}{\tau_2}\right) + \frac{\langle N \rangle^2}{6} A_1 \exp\left(\frac{-t}{0.44 \tau_2}\right) \quad (4.12)$$

with τ_2 the biexciton lifetime. The fitted biexciton lifetime for samples S1 – S7 are shown in Table 4.2. Depending on the core and shell dimensions, this yielded a biexciton lifetime ranging from 190 to 390 ps. Moreover, considering sets of samples with similar core sizes, such as (S1; S2), (S3; S4; S6), and (S5; S7), we systematically find that the biexciton lifetime increases with increasing QD volume. Such values and trends are in line with literature reports on the biexciton lifetime in CdSe/CdS QDs, and they are comparable to the time span a state of net gain is maintained after pumping (see Fig.4.8b). In line with literature, we thus assign the optical gain observed after photo-excitation of CdSe/CdS QDs to stimulated emission from bi- or multi-excitons states.^{15;22}

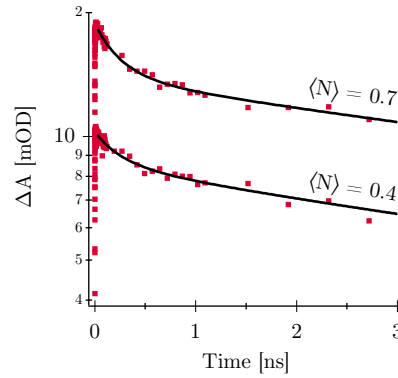


Figure 4.9: ΔA -time slices of sample S1 (red) for $\langle N \rangle < 1$, fitted with Eq. (4.12) (black).

Table 4.2: The biexciton lifetimes τ_{XX} , which are found using the procedure outlined above.

Sample	d_c [nm]	V_{qd} [nm ³]	τ_{XX} [ps]
S1	4.0	210.9	295
S2	4.0	415.6	364
S3	2.9	348.8	190
S4	2.9	461.8	328
S5	2.4	562.3	214
S6	2.9	699.4	390
S7	2.3	870.7	228

4.3.2 Quantitative analysis of optical gain

By means of material gain maps recorded at different pumping powers, we made a quantitative study of optical gain in all 7 CdSe/CdS samples. To provide an overview of the main trends, Figs. 4.10a-c represent transient material gain spectra recorded for sample S1, S3 and S5, respectively. In all cases, a time delay of 3 ps was chosen as this delay generally yields the maximum gain. Considering the much longer multi-exciton decay time constants, we can still assume the initial carrier density is present. In addition, the pump wavelength was set at 520 or 530 nm, *i.e.*, slightly below the CdS absorption edge, to ensure a constant excitation profile throughout the samples. This implies we are pumping carriers into the highly degenerate shell and/or p-states and as such, no instantaneous saturation is expected nor observed at the pump wavelength. For all 3 spectra shown, we found that increasing the pump fluence brings the QD dispersions in a regime of net optical gain. At first, gain appears at around the $1S_e - 1S_h$ band-edge transition. Interestingly, in the case of the large core/thin shell sample S1, this initial gain band exhibits a redshift as compared to the band-edge transition, whereas for the small core/thick shell sample S5, the initial gain band is blue shifted. We will come back to this remarkable observation later. With increasing pump power, the gain band develops into a broad gain spectrum that can be up to 150 nm wide in the case of sample S1. Since this gain band has the imprint of the higher energy $1S_e - 2S_h$ transition, we attribute this broadening of the gain spectrum to filling of the higher-energy $2S_h$ hole level.

In Figure 4.10d, we show the maximum material gain as a function of the pump fluence for all 7 samples studied. In line with Fig. 4.3, we find that this maximum material gain first increases linearly and then levels off – or even slightly decreases – when the pump fluence is raised. Comparing the saturation traces for S1 and S3 with Figs. 4.10a and 4.10b, it follows that the gain saturates at pulse energies where gain through the higher energy $1S_e - 2S_h$ transition becomes possible. Hence, it seems that gain saturation is indeed due to the complete occupation of the band-edge states with electrons and holes. Considering sets of samples with similar core sizes, *i.e.*, (S1; S2), (S3; S4; S6), and (S5; S7), Fig. 4.10d confirms that increasing the shell volume for a given core size lowers the maximum gain. For example, whereas sample S1 exhibits a maximum material gain of 2800 cm^{-1} , we only obtain a value of 1900 cm^{-1} for sample S2. On the other hand, comparing the threshold energy within these 3 sets suggests that an increase of the core thickness comes with a higher threshold. Although a detailed comparison with the model predictions require an analysis at wavelengths shorter than

the band-edge transition, this finding is unexpected since the cross section of the core transitions – and thus the threshold to reach a given occupancy N – should be similar for similar cores.

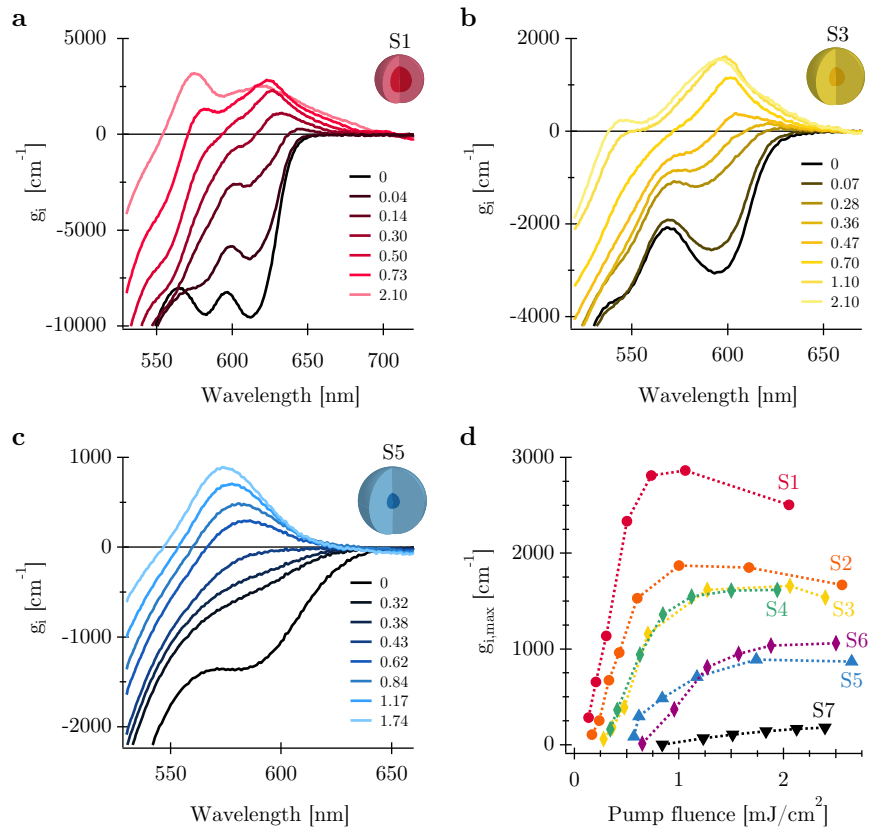


Figure 4.10: (a)-(b)-(c) Spectral slices taken $t = 3$ ps, as a function of the energy fluence (in mJ/cm²) of samples (a) S1, (b) S3 and (c) S5. (d) Maxima of material gain as a function of the pump energy fluence. Note that the samples with the same core diameter have the same point symbols.

Finally, let us elaborate on the observation that the gain band initially develops at the red of the band-edge transition for large-core/thin-shell QDs such as S1 and at the blue of the band-edge transition for small-core/thick-shell samples such as S5. In Figure 4.12, we compare for each sample the linear absorbance spectrum A_0 with the absorbance spectrum A_1 of the same sample under conditions where each QD contains 1 electron-hole pair. We obtained the latter by adding to A_0 the change in absorbance recorded under conditions where at least 95% of the QDs contain a single electron-hole pair. In practice, this is achieved by using optical pulses that create an initial average exciton population of $\langle N \rangle \geq 3$ and a delay of 3 ns, to ensure that all multiexcitons have decayed. Focusing first on the A_1 -spectrum recorded on the large core/thin shell sample S1, one sees that the A_1 -spectrum contains similar, yet slightly shifted features as compared to the A_0 -spectra. The shift of the band-edge absorption is indicative of the energy shift between biexcitons and excitons that is typically attributed to unbalanced Coulomb interactions.^{23;24} A look at the different spectra directly shows that the exciton features in A_1 are redshifted as compared to A_0 in the case of samples S1, whereas they are blueshifted for thick shell samples such as S6 and S7.

These shifts can be quantified by either an explicit deconvolution of the spectra or by analyzing the second derivative of the absorption spectrum, see Figs. 4.11a and 4.11b respectively. The first method allows to reconstruct the whole spectrum, but becomes less straightforward when different peaks strongly overlap (*e.i.* in sample S7). Note that the position of the first optical transition is identical in both methods. The second method, is therefore the method of choice when we are only interested in determining the position of this transition rather than reconstructing the whole spectrum (see Section 4.4). Figure 4.12b displays the resulting energy shifts as a function of f_{sh} , which confirms that samples S1 en S2 exhibit a redshifted biexciton transition ($\delta E < 0$) while the thicker shell samples S4 to S7 exhibit an increasingly blueshifted biexciton ($\delta E > 0$). Such shifts have been attributed before to unbalanced Coulomb interactions between the different charge carriers forming a multi-exciton, which can shift the absorption spectrum either to higher or lower energies depending on the characteristics of the nanostructure.²⁴⁻²⁶ Already before, such shifts have been used to adjust optical gain thresholds,²⁷ and also here, we find that the spectral shift of the initial gain band is correlated to the biexciton Coulomb shift. For one thing, this finding confirms the idea that gain is due to biexciton or multiexciton transitions.

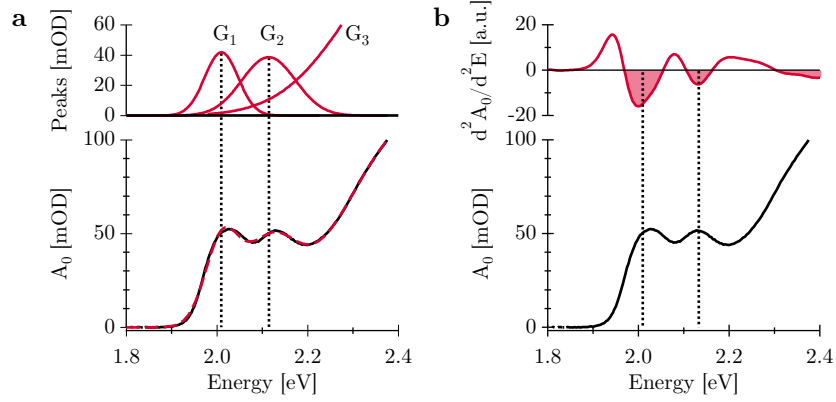


Figure 4.11: Finding the spectral position of the optical transitions in sample S1, using: (a) Multi-peak fitting with Gaussians (G_1 ; G_2 ; G_3) (red). This method allows to reconstruct the whole spectrum (red dashed line). (b) The local maxima of the absorbance spectrum are found at the minima of the second derivative (red).

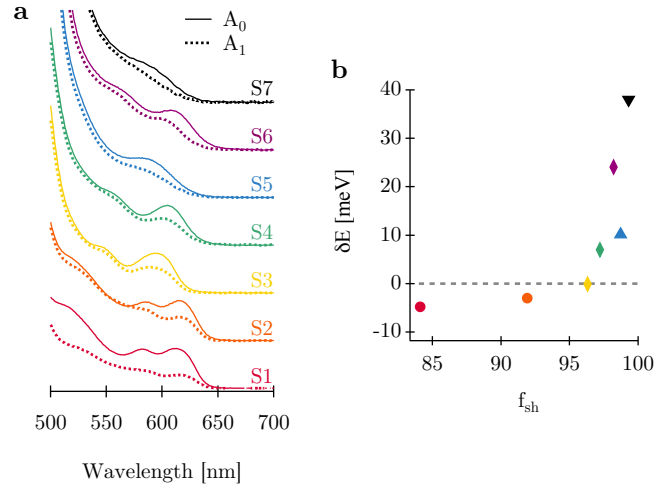


Figure 4.12: (a) Absorbance spectra A_0 (full lines) and A_1 (dotted lines). (b) Fitted energy shift δE of the $1S_e - 1S_h$ -feature in a QD ensemble with $N = 0$ and $N \approx 1$.

4.3.3 Model validation

The model outlined in Section 4.2.2 predicted a reduction of the maximum material gain with increasing shell volume fraction, putting forward a $(1 - f_{\text{sh}})$ -dependence for a fixed core size, and an inverse scaling of the gain threshold with the QD volume. To avoid possible artefacts due to spectral broadening and shifts, we assess the first model prediction by means of a comparison between the integrated material gain and the integrated maximum material gain, as deduced from the intrinsic absorption coefficient spectrum. The integral was taken up to the gain maximum for the saturated material gain spectrum, and up to the maximum of the first exciton transition for the intrinsic absorption coefficient spectra. In this way, we single out optical gain associated with the band gap transition, and we can obtain the total integrated gain by simply doubling the thus obtained number. The results are displayed in Fig. 4.14a, where colored markers represent the experimental data based on gain spectra and grey squares the expected number based on the intrinsic absorption coefficient. In line with the model prediction, we find that the material gain coefficient systematically decreases with increasing shell volume fractions, up to the point where optical gain seems to vanish in the limit $f_{\text{sh}} \rightarrow 0$. At the same time, as shown in the inset of Fig. 4.14a, the ratio between the experimental and the theoretical maximum material gain is close to one, falling within the range 0.8–1.0. The largest deviation, *i.e.*, a ratio of 0.8, we obtained with S7. As can be seen in Fig. 4.10d, full saturation was most likely not reached for sample S7 at the pumping powers we had available, explaining the slightly lower ratio of 0.8 for this sample. Hence, we conclude that as predicted, the integrated intrinsic absorption coefficients provides an almost quantitative estimate of the material gain of a sample of CdSe/CdS QDs.

In the case of femtosecond pulsed excitation, gain thresholds can be either expressed as the energy fluence per pulse $J_{\text{th}}(\lambda_{\text{p}})$ or the average electron-hole pair occupation $\langle N \rangle_{\text{th}}$ per QD needed to reach optical transparency. To find the gain threshold, $\Delta A/A_0$ versus the pump pulse fluence J for different probe wavelengths is plotted, as shown in Fig. 4.13a for sample S1. These points are fitted with a sigmoid function to find the fluence where $\Delta A/A_0 = 1$. It can be seen that for sample S1 gain first occurs at $\lambda = 640$ nm when $J_{\text{th}}(520 \text{ nm}) = 0.64 \text{ mJ/cm}^2$. The average number of electron-hole pairs created by a pump fluence J can be calculated as:

$$\langle N \rangle = \frac{J(\lambda_{\text{p}})}{E_{\text{ph}}(\lambda_{\text{p}})} \times \sigma(\lambda_{\text{p}}) \quad (4.13)$$

Here, $J(\lambda_{\text{p}})/E_{\text{ph}}(\lambda_{\text{p}})$ is the incident photon flux and $\sigma(\lambda_{\text{p}})$ is the absorption

cross section at the pump wavelength. The absorption cross section at any wavelength can be calculated using

$$\sigma(\lambda) = \frac{A(\lambda)}{A(\lambda_{\text{ref}})} \times \mu_i(\lambda_{\text{ref}}) \times V_{\text{qd}} \quad (4.14)$$

where $\mu_i(\lambda_{\text{ref}})$ is calculated using MG-theory. The absorption cross sections at reference wavelength $\lambda_{\text{ref}} = 350$ nm and pump wavelength $\lambda_{\text{p}} = 520$ nm, calculated using Eq. (4.14), for all samples are shown in Table 4.3. The absorption cross section at the pump wavelength can also be obtained from the analysis of the differential absorption at long delay times as a function of pump-power. When all multi-excitons have recombined through Auger recombination, ($t \gg \tau_{XX}$), the population of the remaining single excitons should scale with ΔA according to

$$\Delta A(t = 3 \text{ ns}) = \frac{2A_0}{g} \left(1 - e^{-\langle N \rangle}\right) \quad (4.15)$$

with g the degeneracy of the levels involved in the transition. Figure 4.13a shows $\Delta A/A_0$ versus $\langle N \rangle$ for sample S1, fitted with such a distribution $f(\langle N \rangle) = C(1 - e^{-\alpha \langle N \rangle})$, where α can be seen as a correction factor on $\langle N \rangle$, which accounts for possible errors on the spot size, beam overlap and estimation of the absorption cross section. The fitted α -values are shown in Table 4.3, and result in the correct absorption cross section $\alpha \times \sigma(520 \text{ nm})$. Having $\sigma(\lambda_{\text{p}})$, we can readily recalculate threshold fluences into a threshold electron-hole pair occupation $\langle N \rangle_{\text{th}}$ by means of Eq. (4.13).

Table 4.3: Absorption cross sections at reference wavelength $\lambda_{\text{ref}} = 350$ nm and pump wavelength $\lambda_{\text{p}} = 520$ nm calculated using MG-theory and Eq. (4.14) respectively. Correction factor α .

Sample	$\sigma(350)$ [cm^{-2}]	$\sigma(520)$ [cm^{-2}]	α
S1	$2.55 \cdot 10^{-14}$	$3.96 \cdot 10^{-15}$	1.44
S2	$4.99 \cdot 10^{-14}$	$4.73 \cdot 10^{-15}$	0.93
S3	$4.16 \cdot 10^{-14}$	$1.93 \cdot 10^{-15}$	1.25
S4	$5.50 \cdot 10^{-14}$	$2.56 \cdot 10^{-15}$	0.99
S5	$6.69 \cdot 10^{-14}$	$2.39 \cdot 10^{-15}$	0.89
S6	$8.33 \cdot 10^{-14}$	$2.51 \cdot 10^{-15}$	1.09
S7	$1.04 \cdot 10^{-13}$	$2.17 \cdot 10^{-15}$	1.29

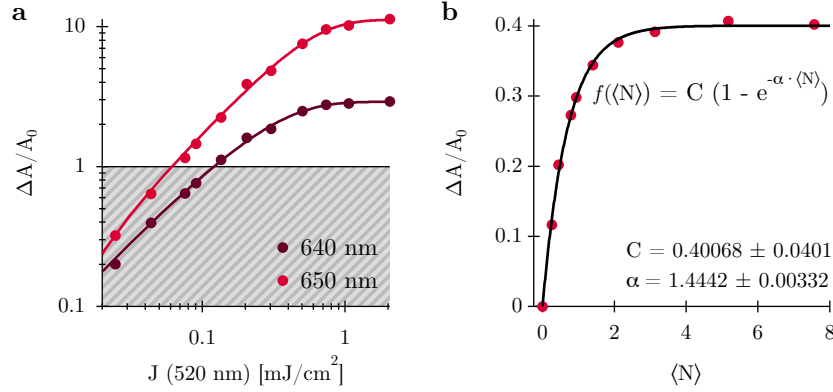


Figure 4.13: For sample S1: (a) $\Delta A/A_0$ versus $J(520 \text{ nm})$ at short delay time $t = 3 \text{ ps}$ at probe wavelengths 640 and 650 nm. (b) $\Delta A/A_0$ versus $\langle N \rangle$ at the bandgap wavelength and delay time $t = 3 \text{ ns}$, fitted with exponential function.

The main assumption leading to the $1/V_{\text{qd}}$ scaling of the gain threshold was that core/shell QDs have the same threshold occupancy $\langle N \rangle_{\text{th}}$, regardless of their morphology. More specifically, we found that $\langle N \rangle_{\text{th}} = 1.54$ for CdSe/CdS core/shell QDs. Hence, a theoretical threshold fluence can be estimated as:

$$J_{\text{th}}(\lambda_p) = 1.54 \times E_{ph}(\lambda_p) \times \frac{1}{\sigma(\lambda_p)} \quad (4.16)$$

Here, the pump fluence is less of an intrinsic property. It depends on the absorption cross section of the QDs, a quantity that varies along with the absorption coefficient. On the other hand, assuming that $\langle N \rangle_{\text{th}}$ is independent of the pump wavelength, a threshold fluence measured at λ_p can be converted to a threshold fluence at any wavelength λ by a straightforward rescaling:

$$J_{\text{th}}(\lambda) = \frac{E_{ph}(\lambda)}{E_{ph}(\lambda_p)} \frac{A_0(\lambda_p)}{A_0(\lambda)} \times J_{\text{th}}(\lambda_p) \quad (4.17)$$

To correctly account for the influence of shell-enhanced absorption on the energy fluence per pulse threshold, we used Eq. (4.17) to obtain equivalent thresholds at 350 nm. Figure 4.14b displays the thus obtained experimental thresholds $J_{\text{th}}(350 \text{ nm})$ together with theoretical estimates. Intriguingly, rather than the predicted $1/V_{\text{qd}}$ scaling, we find that the experimental thresholds constitute a set of scattered numbers, ranging between 12 and 20 $\mu\text{J}/\text{cm}^2$. Hence, the pronounced threshold reduction that was expected

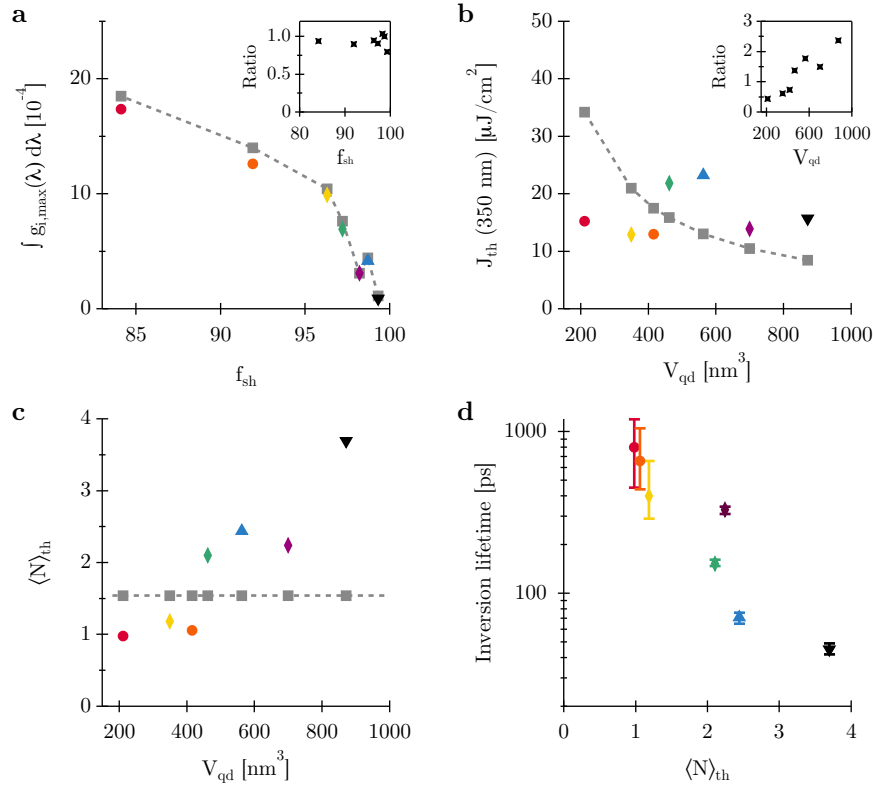


Figure 4.14: (a) Integrated maximum material gain versus shell volume fraction as determined from (colored markers) experimental material gain maps and (grey markers) the intrinsic absorption coefficient spectrum. The inset shows the ratio of both numbers. (b)-(c) Estimated thresholds $J_{th}(350 \text{ nm})$ and $\langle N \rangle_{th}$ as a function of V_{qd} as determined from (colored markers) experimental data and (gray markers) theoretical values. The latter is based on $\langle N \rangle_{th}=1.54$ and Eq. (4.16). (d) The inversion lifetime as a function of V_{qd} .

for more voluminous QDs seems absent for actual CdSe/CdS core/shell QDs, contradicting the idea that more voluminous QDs would yield lower lasing thresholds by default. From the experimentally determined threshold fluence, we obtained $\langle N \rangle_{th}$ using Eq. (4.13). Figure 4.14c shows the resulting threshold occupation as a function of V_{qd} . Opposite from the initial assumption, we find that $\langle N \rangle_{th}$ is markedly different for the various

CdSe/CdS samples studied here. Whereas thin shell samples such as S1, S2 and S3 show gain at a threshold $\langle N \rangle_{\text{th}}$ of around 1, it requires on average 3.7 electron-hole pairs to attain optical gain in the case of the thick shell sample S7.

To further analyse the impact of the differences in threshold occupation on the optical gain characteristics, we looked at the time window during which optical gain persists after optical pumping. Characterizing this window by the time delay τ_g where the regime of optical gain disappears, we find that optical gain can last up to 800 ps in the case of the thin-shell sample S1, whereas optical gain has already disappeared after 45 ps in the case of the thick-shell sample S7 (see Fig. 4.14d). If indeed, as indicated by the gain threshold, optical gain in the latter sample requires higher-order multiexcitons, this dramatic collapse of the gain lifetime is to be expected. Multi-excitons recombine through Auger processes, which speed up significantly with increasing N . Hence, we conclude that thick shell CdSe/CdS core/shell QDs have multiple disadvantages as optical gain material. While they exhibit, as expected, a lower material gain, the higher threshold occupation makes that this drawback is not compensated by a lower threshold energy and brings the additional drawback of a shortened optical gain window.

4.4 Discussion

The comparison between the main experimental results and the model predictions indicates a marked inconsistency at the level of the gain threshold, that may point to shortcomings in the initial modeling of optical gain. Looking at Figure 4.10, a first element that was left out is that gain may result from higher energy transitions different from the band-edge transition. Moreover, referring to Figure 4.12, we discarded possible spectral shifts of the biexciton or multiexciton transitions. As we found, such shifts change from an attractive redshift for the samples featuring the lowest occupation threshold to a repulsive blueshift for the samples with the higher occupation threshold. Here, we will include both elements in Eq. (4.8), and compare this extended description of the non-linear absorption spectrum with the experimental gain spectra. We will include Coulomb shifts in the expression of the non-linear absorbance by assuming that the same shift applies to the entire spectrum and that it scales with the exciton occupation N .²³ Referring to Figure 4.15a, these assumptions enable us to write the absorbance

spectrum $\mathcal{A}^{(1)}(N_e, N_{h,1})(E)$ of the first exciton feature as:

$$\mathcal{A}^{(1)}(N_e, N_{h,1})(E) = \left(1 - \frac{N_e}{g_e} - \frac{N_{h,1}}{g_{h,1}}\right) A_0^{(1)}(E - N \cdot \delta E) \quad (4.18)$$

Here, N_e and $N_{h,1}$ indicate the occupation of the conduction and valence band-edge states, whereas N is the total number of electron-hole pairs in the QD. At the same time, the stimulated emission spectrum $\mathcal{G}^{(1)}(N_e, N_{h,1})(E)$ related to this transition will become (see Fig. 4.15a):

$$\mathcal{G}^{(1)}(N_e, N_{h,1})(E) = \frac{N_e N_{h,1}}{g_e g_{h,1}} A_0^{(1)}(E - (N - 1) \cdot \delta E) \quad (4.19)$$

Using Eq. (4.7), $\mathcal{A}^{(1)}$ and $\mathcal{G}^{(1)}$ can be combined to yield the net absorbance $A^{(1)}(N_e, N_{h,1})(E)$. Moreover, similar expressions will apply to the second absorption feature that involves transitions from the second valence-band level to the first conduction-band level. All together, the non-linear absorbance spectrum of both transitions is thus obtained as:

$$A(\langle N \rangle) = \sum_{N=0}^{\infty} P(N) \left(A^{(1)}(N_e, N_{h,1})(E) + A^{(2)}(N_e, N_{h,2})(E) \right) \quad (4.20)$$

We will evaluate this expression by assuming a Poisson distribution for $P(N)$ and by imposing progressive filling of the electron and hole levels. Hence, $N_e = \min(N; g_e)$ and $N_{h,1} = \min(N; g_{h,1})$, while $N_{h,2}$ is kept at 0 as long as $N \leq g_h$ and taken as $N_{h,2} = \min(N - g_{h,1}; g_{h,2})$ otherwise.

To develop an understanding of the way spectral shifts affect the absorbance of photo-excited QDs, and thus the possible development of a gain band, we took the measured A_0 -spectrum of sample S1 as a starting point and imposed a positive and negative shift $|\delta E| = 10$ meV. As shown in Fig. 4.15b, the spectral features $A_0^{(1)}$ and $A_0^{(2)}$ of the first and the second transition were obtained from a spectral deconvolution (see Section 4.3.2). Furthermore, a fixed background was included to account for higher energy transitions. The additional spectra in Fig. 4.15b represent non-linear absorbance spectra, simulated by means of Eq. (4.20), for different average occupations $\langle N \rangle$. Focusing on the $\langle N \rangle = 1$ case first, we use the filled areas to represent the net absorbance $A^{(1)}(N_e, N_{h,1})(E)$ and $A^{(2)}(N_e, N_{h,1})(E)$. Under these pumping conditions, the non-linear spectra calculated for either attractive or repulsive Coulomb interactions are highly similar, and no region of negative absorbance or gain is observed. Increasing the occupation to $\langle N \rangle = 1.7$, we see that the first exciton absorbance $A^{(1)}$ turns

negative, irrespective of the sign of the Coulomb interactions. In the case of a biexciton redshift ($\delta E = -10$ meV), this results in an effective gainband, since stimulated emission does not overlap with other, absorbing transitions. Stimulated emission by blueshifted biexcitons, however, is counteracted by the second exciton transition $A^{(2)}$, which makes that such QDs will fail to show net gain at these pumping levels. Competition with absorbing transitions can be overcome by further increasing the occupation, as shown by the spectrum simulated for $\langle N \rangle = 2$.

Figures 4.15c-d represents simulated spectra assuming Coulomb shifts $\delta E = -15$ meV and $+15$ meV, where we used the absorbance spectrum of sample S1 and S5 as a reference, respectively. It can be clearly seen that including Coulomb shifts suffices to reproduce the main features of the experimentally determined gain characteristics, most notably the red shift or blue shift of the initial gain band, and the increased threshold to reach net stimulated emission in the case of repulsive Coulomb interactions. In Figure 4.15e, we address the issue of the threshold occupation in more detail, by plotting normalized spectral $-A$ -slices at the wavelength where gain first appears as a function of the occupation $\langle N \rangle$. Here, calculations use the absorbance A_0 of sample S1 as a reference, and the Coulomb shift as taken as an adjustable parameter. One clearly sees how an increasingly repulsive exciton-exciton interaction increases the threshold occupation, a trend we assign to the increasing overlap between stimulated emission by the band-edge transition and counteraction absorption by transitions that are, initially, at a higher photon energy.

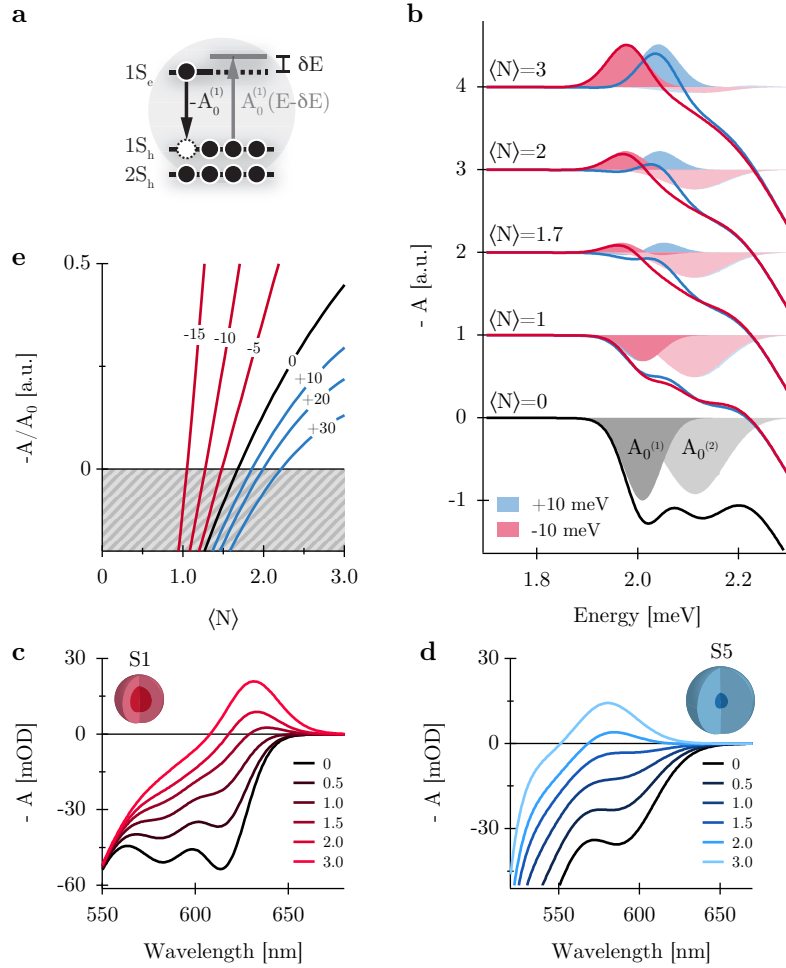


Figure 4.15: (a) Extended model with biexciton shift δE (b) Effect of positive (blue) and negative (red) biexciton shift on the absorbance spectra A with its individual components A_1 and A_2 . (c)-(d) Overview of calculated absorbance spectra starting from A_0 spectrum of S1 and S5 and with δE equal to -15 meV and +15 meV respectively for $\langle N \rangle$ ranging from 0.5–3. (e) Spectral $-A/A_0$ -slices, starting from A_0 spectrum of S1, at the wavelength where gain first appears for varying δE in meV.

4.5 Conclusion

We have presented an experimental study on the relation between the gain characteristics of CdSe/CdS core/shell QDs and the core/shell morphology. In line with the prediction of a simple QD model, we find that the maximum material gain corresponds to the intrinsic absorption coefficient of the band-edge transition. This makes that large core/thin shell samples feature the higher material gain – reaching up to 2800 cm^{-1} for the best sample studied here. According to the same model, threshold fluences should scale with the inverse of the QD volume. This prediction, however, is contradicted by the experimental results, which show little variation of the threshold fluence as a function of core/shell morphology. This largely constant threshold implies that thick shell QDs need more electron-hole pairs on average to reach transparency. At the same time, we find that such thick shell QDs show an increasingly repulsive biexciton interaction. By means of gain spectrum simulations, we show that the resulting blueshift of the multi-exciton transitions accounts for the increasing threshold occupation. As this comes with a pronounced shortening of the gain window, *i.e.*, the time span net optical gain can be maintained after photo-excitation, we conclude that CdSe/CdS QDs featuring a biexciton redshift, such as large core/thin shell CdSe/CdS structures, are preferred for optical gain applications. They combine a larger material gain with a lower threshold electron-hole pair occupation and a longer gain window. We believe such insights will be most valuable to guide future work to improve colloidal QDs for optical gain applications and develop optimized QD-lasers.

References

- [1] V. I. Klimov, A. A. Mikhailovsky, S. Xu, A. Malko, J. A. Hollingsworth, C. A. Leatherdale, H.-J. Eisler, and M. G. Bawendi, “Optical gain and stimulated emission in nanocrystal quantum dots,” *Science*, vol. 290, no. 5490, pp. 314–317, 2000.
- [2] W. Xie, Y. Zhu, S. Bisschop, T. Aubert, Z. Hens, D. van Thourhout, and P. Geiregat, “Colloidal quantum dots enabling coherent light sources for integrated silicon-nitride photonics,” *IEEE Journal of Selected Topics in Quantum Electronics*, vol. 23, pp. 1–13, Sept 2017.
- [3] J. M. Pietryga, Y.-S. Park, J. Lim, A. F. Fidler, W. K. Bae, S. Brovelli, and V. I. Klimov, “Spectroscopic and device aspects of nanocrystal quantum dots,” *Chemical Reviews*, vol. 116, no. 18, pp. 10513–10622, 2016. PMID: 27677521.
- [4] M. Kazes, D. Lewis, Y. Ebenstein, T. Mokari, and U. Banin, “Lasing from semiconductor quantum rods in a cylindrical microcavity,” *Advanced Materials*, vol. 14, no. 4, pp. 317–321, 2002.
- [5] A. V. Malko, A. A. Mikhailovsky, M. A. Petruska, J. A. Hollingsworth, H. Htoon, M. G. Bawendi, and V. I. Klimov, “From amplified spontaneous emission to microring lasing using nanocrystal quantum dot solids,” *Applied Physics Letters*, vol. 81, no. 7, pp. 1303–1305, 2002.
- [6] H.-J. Eisler, V. C. Sundar, M. G. Bawendi, M. Walsh, H. I. Smith, and V. Klimov, “Color-selective semiconductor nanocrystal laser,” *Applied Physics Letters*, vol. 80, no. 24, pp. 4614–4616, 2002.
- [7] F. Fan, O. Voznyy, R. P. Sabatini, K. T. Bicanic, M. M. Adachi, J. R. McBride, K. R. Reid, Y.-S. Park, X. Li, A. Jain, R. Quintero-Bermudez, M. Saravanapavanantham, M. Liu, M. Korkusinski, P. Hawrylak, V. I. Klimov, S. J. Rosenthal, S. Hoogland, and E. H. Sargent, “Continuous-wave lasing in colloidal quantum dot solids enabled by facet-selective epitaxy,” *Nature*, vol. 544, pp. 75 EP –, 03 2017.
- [8] M. M. Adachi, F. Fan, D. P. Sellan, S. Hoogland, O. Voznyy, A. J. Houtepen, K. D. Parrish, P. Kanjanaboos, J. A. Malen, and E. H. Sargent, “Microsecond-sustained lasing from colloidal quantum dot solids,” *Nature Communications*, vol. 6, p. 8694, 2015.
- [9] V. I. Klimov, A. A. Mikhailovsky, D. W. McBranch, C. A. Leatherdale, and M. G. Bawendi, “Quantization of multiparticle auger rates in semi-

- conductor quantum dots,” *Science*, vol. 287, no. 5455, pp. 1011–1013, 2000.
- [10] F. Garcia-Santamaria, Y. Chen, J. Vela, R. D. Schaller, J. A. Hollingsworth, and V. I. Klimov, “Suppressed auger recombination in “giant” nanocrystals boosts optical gain performance,” *Nano Letters*, vol. 9, no. 10, pp. 3482–3488, 2009. PMID: 19505082.
- [11] F. Garcia-Santamaria, S. Brovelli, R. Viswanatha, J. A. Hollingsworth, H. Htoon, S. A. Crooker, and V. I. Klimov, “Breakdown of volume scaling in auger recombination in cdse/cds heteronanocrystals: The role of the core/shell interface,” *Nano Letters*, vol. 11, no. 2, pp. 687–693, 2011. PMID: 21207930.
- [12] W. K. Bae, L. A. Padilha, Y.-S. Park, H. McDaniel, I. Robel, J. M. Pietryga, and V. I. Klimov, “Controlled alloying of the core/shell interface in cdse/cds quantum dots for suppression of auger recombination,” *ACS Nano*, vol. 7, no. 4, pp. 3411–3419, 2013. PMID: 23521208.
- [13] M. Nasilowski, P. Spinicelli, G. Patriarche, and B. Dubertret, “Gradient cdse/cds quantum dots with room temperature biexciton unity quantum yield,” *Nano Letters*, vol. 15, no. 6, pp. 3953–3958, 2015. PMID: 25990468.
- [14] V. Pinchetti, F. Meinardi, A. Camellini, G. Sirigu, S. Christodoulou, W. K. Bae, F. De Donato, L. Manna, M. Zavelani-Rossi, I. Moreels, V. I. Klimov, and S. Brovelli, “Effect of core/shell interface on carrier dynamics and optical gain properties of dual-color emitting cdse/cds nanocrystals,” *ACS Nano*, vol. 10, no. 7, pp. 6877–6887, 2016. PMID: 27276033.
- [15] Y. S. Park, W. K. Bae, T. Baker, J. Lim, and V. I. Klimov, “Effect of Auger Recombination on Lasing in Heterostructured Quantum Dots with Engineered Core/Shell Interfaces,” *Nano Letters*, vol. 15, no. 11, pp. 7319–7328, 2015.
- [16] W. Xie, T. Stöferle, G. Rainò, T. Aubert, S. Bisschop, Y. Zhu, R. F. Mahrt, P. Geiregat, E. Brainis, Z. Hens, and D. Van Thourhout, “On-chip integrated quantum-dot silicon-nitride microdisk lasers,” *Advanced Materials*, vol. 29, no. 16, pp. 1604866–n/a, 2017. 1604866.
- [17] Y. Zhu, W. Xie, S. Bisschop, T. Aubert, E. Brainis, P. Geiregat, Z. Hens, and D. Van Thourhout, “On-chip single-mode distributed feedback colloidal quantum dot laser under nanosecond pumping,” *ACS Photonics*, vol. 4, no. 10, pp. 2446–2452, 2017.

- [18] Z. Hens and I. Moreels, “Light Absorption by Colloidal Semiconductor Quantum Dots,” *J. Mat. Chem.*, vol. 22, no. 21, pp. 10406–10415, 2012.
- [19] M. Cirillo, T. Aubert, R. Gomes, R. Van Deun, P. Emplit, A. Biermann, H. Lange, C. Thomsen, E. Brainis, and Z. Hens, ““flash” synthesis of cdse/cds core-shell quantum dots,” *Chemistry of Materials*, vol. 26, no. 2, pp. 1154–1160, 2014.
- [20] E. Drijvers, J. De Roo, P. Geiregat, K. Feher, Z. Hens, and T. Aubert, “Revisited Wurtzite CdSe Synthesis: A Gateway for the Versatile Flash Synthesis of Multishell Quantum Dots and Rods,” *Chem. Mater.*, vol. 28, pp. 7311–7323, OCT 25 2016.
- [21] G. E. Cragg and A. L. Efros, “Suppression of auger processes in confined structures,” *Nano Letters*, vol. 10, no. 1, pp. 313–317, 2010. PMID: 20017564.
- [22] V. I. Klimov, “Spectral and dynamical properties of multiexcitons in semiconductor nanocrystals,” *Annual review of physical chemistry*, vol. 58, pp. 635–673, 2007.
- [23] P. Geiregat, A. Houtepen, Y. Justo, F. C. Grozema, D. Van Thourhout, and Z. Hens, “Coulomb shifts upon exciton addition to photoexcited pbs colloidal quantum dots,” *The Journal of Physical Chemistry C*, vol. 118, no. 38, pp. 22284–22290, 2014.
- [24] A. F. Cihan, Y. Kelestemur, B. Guzelturk, O. Yerli, U. Kurum, H. G. Yaglioglu, A. Elmali, and H. V. Demir, “Attractive versus repulsive excitonic interactions of colloidal quantum dots control blue- to red-shifting (and non-shifting) amplified spontaneous emission,” *Journal of Physical Chemistry Letters*, vol. 4, no. 23, pp. 4146–4152, 2013.
- [25] J. Nanda, S. A. Ivanov, M. Achermann, I. Bezel, A. Piryatinski, and V. I. Klimov, “Light amplification in the single-exciton regime using exciton-exciton repulsion in type-ii nanocrystal quantum dots,” *The Journal of Physical Chemistry C*, vol. 111, no. 42, pp. 15382–15390, 2007.
- [26] G. Rainò, T. Stöferle, I. Moreels, R. Gomes, J. S. Kamal, Z. Hens, and R. F. Mahrt, “Probing the wave function delocalization in CdSe/CdS dot-in-rod nanocrystals by time-and temperature-resolved spectroscopy,” *ACS Nano*, vol. 5, no. 5, pp. 4031–4036, 2011.
- [27] V. I. Klimov, S. A. Ivanov, J. Nanda, M. Achermann, I. Bezel, J. A. McGuire, and A. Piryatinski, “Single-exciton optical gain in semiconductor nanocrystals,” *Nature*, vol. 447, no. 7143, pp. 441–446, 2007.

5

Colloidal QDs for integrated amplifiers and lasers

Following the gain characterisation of different core/shell CdSe/CdS QDs in Chapter 4, a ‘best’ sample was chosen to be used as the gain material in an integrated distributed feedback (DFB)-laser. Starting from a colloidal dispersion, simple strip waveguide amplifiers were fabricated, and the link between modal gain and material gain is exemplified. Next, a DFB-laser was fabricated and characterised under nano-second laser pumping.

5.1 Introduction

Integrated lasers are an essential building block for the development of functional photonic integrated circuits (PICs). In this context, the combination of colloidal QDs with silicon nitride (SiN) is particularly interesting, as the wide tunability of the QDs is compatible with the broad transparency window of silicon nitride. The QD’s solution processability together with the relatively high refractive index ($n \sim 2$) of silicon nitride, allows for the fabrication of compact and cost effective PICs. In addition, as silicon nitride is a well known material in the electronics industry, the SiN-platform can use es-

established fabrication techniques, which allow upscaling to large volumes and high yield fabrication. Already several laser devices based on colloidal QDs have been demonstrated,¹⁻³ but generally lack compactness and/or are not compatible with waveguide integration. We developed a hybrid integration platform in which a spincoated layer of, most often, CdSe/CdS core/shell QDs is embedded in between two layers of silicon nitride, which can be etched to form a waveguide.⁴ This straightforward integration method considerably facilitates the use of colloidal QDs for integrated light emitters and amplifiers. The embedded QDs show amplified spontaneous emission (ASE) under femtosecond pulsed pumping, which can be efficiently coupled to the waveguide's guided mode.⁵ Also lasing action was demonstrated on this hybrid SiN_x/QD/SiN_x integration platform, using a multimode disk laser coupled to an underlying bus waveguide,⁶ to our best knowledge the first demonstration of a fully integrated QD laser. However, the fabrication process of these devices is rather complex. Moreover, such lasers are inherently multi-modal and lasing was only demonstrated upon pumping with relatively short picosecond pulses, a configuration which is not very practical in the long term. Therefore, we moved to a different design consisting of a waveguide coupled DFB-laser. Such a design is also compatible with the same SiN_x/QD/SiN_x-platform but requires less processing steps and is truly single mode.⁷

A long sought after breakthrough for QD opto-electronics is a continuous-wave (CW) laser, pumped either optically at first but preferably electrically driven in the future.⁸ Optical gain in any medium requires a steady population inversion of the electronic transition involved in order for stimulated emission to dominate over absorption. Due to the large degeneracy ($g > 2$) of the band edge, multiple excitons are required to sustain optical gain. In QDs however, these multi-states vanish on a timescale of few 100s of ps due to ultrafast non-radiative Auger recombination. However, in recent work,⁷ we have shown ns-pulsed operation, which is altogether a remarkable feature since the biexciton lifetime makes the 7 ns pulsed pump almost equivalent to quasi-CW operation. This opens the path towards realizing CW-pumped on-chip integrated lasers.

5.2 Colloidal QDs as gain material

After the first demonstrations of optical gain in colloidal QDs, several efforts have been made to improve their overall lasing performance. Although this optimization has mainly focused on strategies that reduce the gain threshold, the role of the gain coefficient to reach lasing action should not be

overlooked. As we have shown in previous the chapter, solution based measurements allow us to characterize the linear (absorption/emission, QY, radiative lifetime) and non-linear (material gain, threshold, excited state lifetime, ...) properties of QDs. By assessing the relation between the structure of CdSe/CdS core/shell QDs, the material gain they can deliver and the threshold needed to attain net stimulated emission, we found that large-core/thin-shell QDs are the overall champion core/shell configuration in terms of both material gain, gain threshold and gain lifetime. The latter is an important parameter to develop a CW-pumped laser, as it is a measure for the rate at which the population inversion needs to be replenished. Following this material optimisation, *i.e.* choosing the optimal core/shell dimensions, a batch of large-core/thin-shell QDs was synthesised for the fabrication of a CW-pumped waveguide coupled DFB-laser. However, before making the transition to actual integrated devices, it is important to assess whether the linear and non-linear properties are well preserved during the fabrication processes involved (*i.e.* QD deposition, embedding them into a SiN_x matrix and patterning those structures into (nano-)photonic components).

As defined in Section 4.2.1, the material gain represents the gain a QD material with a volume fraction $f = 1$ would have under the same pump conditions. Multiplying it with the actual volume fraction yields the gain coefficient of any specific QD sample, from a close-packed thin film to dilute polymer mixtures. The modal gain in an integrated structure can thus be seen as the product of the material gain, the QD volume fraction in the film f and the overlap between the optical mode and the QD-layer Γ :

$$g_m = g_i \times f \times \Gamma \quad (5.1)$$

The modal overlap Γ can be modeled by simulating the mode profiles of the nanophotonic component through effective index solvers (*e.g.* Fimmwave). Hence, by using these device specific values f and Γ , the material gain can be readily translated into a modal gain. Determination of the material gain, gain lifetime and threshold from a solution measurement thus provides us with input for a lower limit to the acceptable loss and confinement for developing nanophotonic components, before going through the effort of fabricating the actual laser cavity. The material gain is thus a most useful design property.

5.2.1 Spectroscopic characterisation

The optimized CdSe/CdS QD sample has a core diameter of 4.16 nm and total diameter of 7.51 nm, which corresponds to a shell volume fraction of $f_{\text{sh}} = 83\%$ (which is similar to sample S1 in Chapter 4). A TEM image and the absorbance and photo-luminescence (PL) spectra of this sample are shown in Figs. 5.1a and 5.1b respectively. Note that this sample has a similar core size, but thinner shell compared to the QD sample used in reference⁷. These dimensions correspond to a lower shell volume fraction (83% compared to 96%) and therefore a higher material gain and significant longer inversion lifetime is expected for this optimized QD sample. This was verified using transient absorption spectroscopy (TAS).

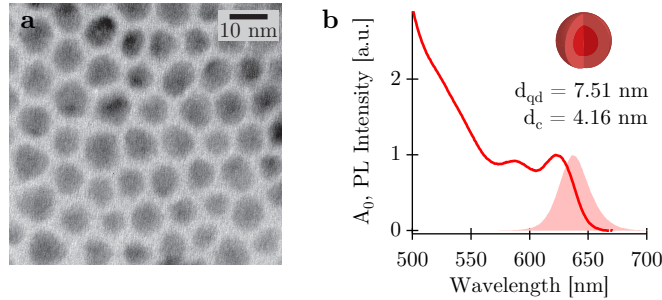


Figure 5.1: Optimized CdSe/CdS QD sample: (a) TEM image and (b) PL- and A_0 -spectrum.

The pump wavelength was set at 520 nm, *i.e.*, slightly below the CdS absorption edge, to ensure a constant excitation profile throughout the sample. The spectral slices of the material gain, taken at maximum gain ($t = 3$ ps), for varying pump fluences (in mJ/cm^2) are shown in Fig. 5.2a. The material gain saturates at 2140 cm^{-1} , which is on the same order of magnitude as the maximum found for sample S1. Again a broad gain band is observed, which first develops on the red side of the band-edge transition and gradually becomes broader, up to 150 nm wide, at the highest pump fluence. The gain threshold is found by plotting $\Delta A/A_0$ versus the pump pulse fluence J for different probe wavelengths, as shown in Fig. 5.2b. It can be seen that gain first occurs at $\lambda = 660$ nm when $J_{\text{th}}(520 \text{ nm}) = 0.06 \text{ mJ}/\text{cm}^2$, or equivalently $J_{\text{th}}(350 \text{ nm}) = 11 \text{ }\mu\text{J}/\text{cm}^2$. The average number of electron-hole pairs created by a pump fluence J can be calculated as:

$$\langle N \rangle = \frac{J(\lambda_p)}{E_{ph}(\lambda_p)} \times \sigma(\lambda_p) \quad (5.2)$$

with $J(\lambda_p)/E_{ph}(\lambda_p)$ the incident photon flux and $\sigma(\lambda_p)$ the absorption cross section at the pump wavelength. As outlined in Section 4.3.3, we obtain the absorption cross section at the pump wavelength from the analysis of the differential absorption at long delay times as a function of pump-power (see Fig. 5.2c). Using Equation (5.2) with $\sigma(520 \text{ nm}) = 3.39 \cdot 10^{-15} \text{ cm}^2 \times 1.56$ we find $\langle N \rangle_{\text{th}} = 0.8$. Finally, a time slice at the probe wavelength where gain first appears and pump fluence corresponding to maximum gain is shown in Fig. 5.2b. The time window during which optical gain persists after optical pumping, *i.e.* the time during which $g_i > 0$, is found to be equal to 800 ps, which is similar to the value found for sample S1.

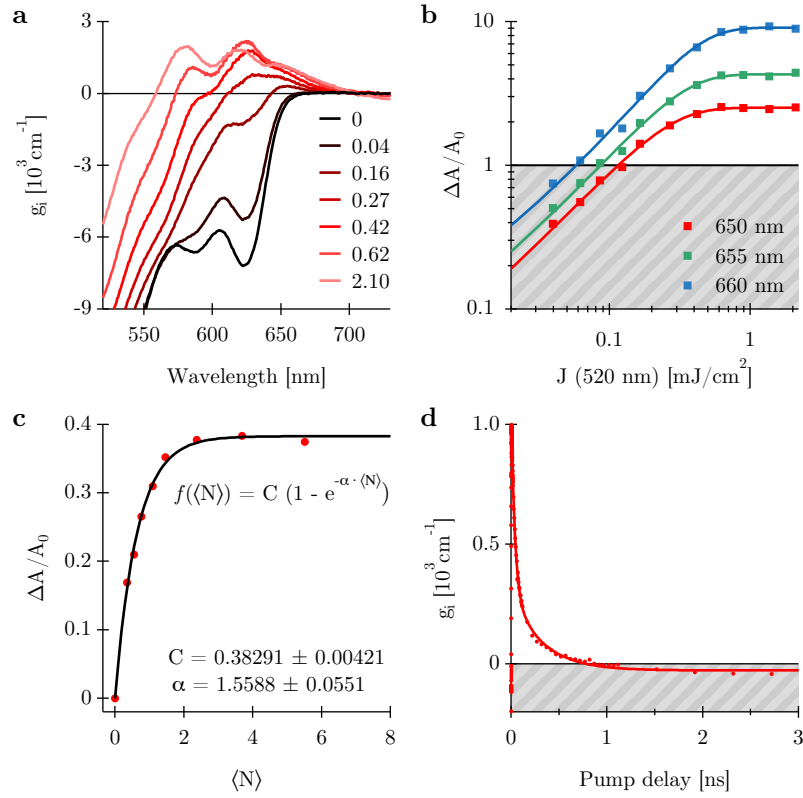


Figure 5.2: (a) Spectral slices taken at $t = 3 \text{ ps}$ and varying pump fluences in mJ/cm^2 . (b) $\Delta A/A_0$ vs. $\langle N \rangle$ at short delay time $t = 3 \text{ ps}$ for probe wavelengths 650, 655 and 660 nm. (c) $\Delta A/A_0$ vs. $\langle N \rangle$ at long delay time $t = 3.1 \text{ ns}$, fitted with an exponential function. (d) Time slice taken at $\lambda = 660 \text{ nm}$ and $J = 0.62 \text{ mJ/cm}^2$.

5.2.2 VSL-measurement: modal gain

We can exemplify the qualities of g_i as a design parameter using the case of QD-doped silicon nitride waveguides, where the material gain g_i , measured using TAS, is compared with the modal gain g_m obtained from a variable stripe length (VSL) experiment. In a classical VSL experiment a 1D amplifier of variable length is created by means of a stripe excitation profile formed by a slit of variable width. This method, although easy to implement, has its pitfalls⁹ especially in terms of collection efficiency of light for large stripe lengths, where light starts to diffuse out of the acceptance cone of the collecting objective. A more robust approach consists of using stripe waveguides of varying lengths dictated by a deterministic etching process, which support well defined optical modes that do not diffuse along the length of the amplifier. Starting from a silicon substrate with a 3 μm thermal oxide grown on top, a 50 nm spincoated layer of CdSe/CdS QDs was integrated in a LF h-SiN_x/QD/MF h-SiN_x stack, following the procedure outlined in Section 1.3. The planar stacks are then etched to form 5 μm wide waveguides with lengths between 50 - 400 μm with a fixed step of 20 μm . The RIE etching process was optimised to ensure smooth sidewalls. As demonstrated in previous work, such waveguides with embedded QDs feature a propagation loss of only a few dB/cm.⁴ Next, the residual resist is stripped away using oxygen plasma. The chip is cleaved, after the lithography step but before the RIE processes, to ensure a uniform facet. A microscopic image of the finished optical chip is shown in Fig. 5.3a.

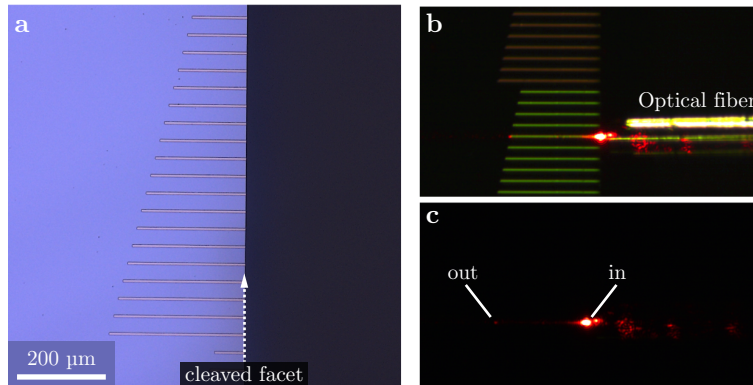


Figure 5.3: (a) Cleaved optical chip with SiN_x/QD/SiN_x waveguides of different lengths. (b)-(c) Light from the waveguide is collected by an optical fiber, which can be connected to a red laser to facilitate the alignment optimization.

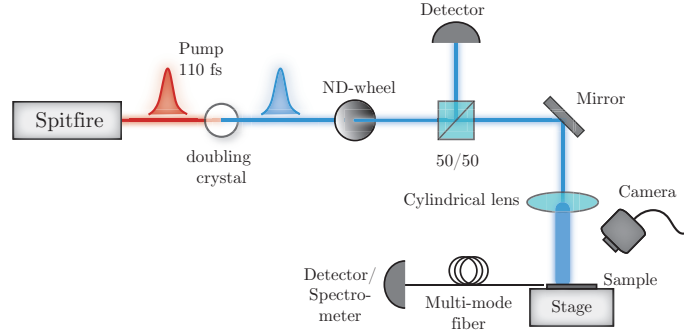


Figure 5.4: Laser setup for VSL-measurement: 110 fs pulses at a 1 kHz repetition rate and $\lambda = 800$ nm are frequency doubled by a BBO crystal. The laser beam is then focused into a stripe by means of a cylindrical lens to pump the waveguides. The emitted light is collected at the waveguide facet by a multimode fiber.

The modal gain is characterised using a femtosecond laser system (see Fig. 5.4). The 110 fs pulses at a 1 kHz repetition rate and a wavelength of 800 nm are frequency doubled in a Beta Barium Borate (BBO) crystal. The intensity of the pump can be tuned using a neutral density (ND) filter and is monitored by splitting 50% of the pump beam towards a detector. The remaining 50 % is sent to a cylindrical lens, which focuses the laser beam into a stripe to pump the waveguides. The focused beam is adjusted to overlap with a single waveguide from which the emitted light is collected by a multimode fiber ($NA = 0.2$). This light is then guided towards either a powermeter or a spectrometer. The measured output spectrum for increasing pump power is plotted in Fig. 5.5. It shows a sharp peak that develops at the high energy side of the spontaneous emission (SE) spectrum, centered around 636 nm. With only a full width at half maximum (FWHM) of 6 nm, this peak is clearly narrowed down compared to the low fluence SE spectrum, which is indicative for ASE.

First, a $P_{\text{out}} - P_{\text{in}}$ measurement is done on the longest waveguide, $L = 400 \mu\text{m}$ (see Fig. 5.6a). At low pump powers there is a linear increase of the output power. As soon as the pump power reached 0.3 mW, a super linear increase of the output power can be noted, which indicates that the emission of the embedded QDs gets amplified, *i.e.* there is optical gain. When the pump power is increased even further, above 0.8 mW, the output power saturates. At this point there is a balance between light absorption and amplified emission.

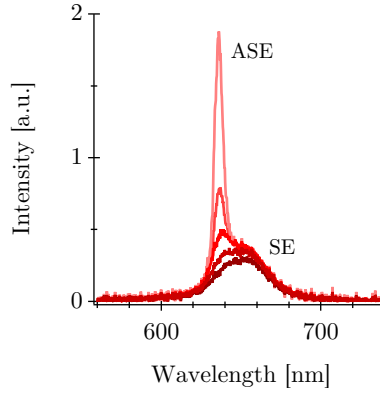


Figure 5.5: Spectrum of the waveguide output for increasing pump fluences (dark \rightarrow light red). A narrow ASE peak develops at the high energy side of the PL-spectrum.

When waveguide stripes of increasing length are pumped with a fixed pump power, the output intensity yields an exponentially increasing light output. Fitting the length-dependent light intensity to:¹⁰

$$I(L) = A_0 \left[\frac{e^{g_m L} - 1}{g_m} \right] \quad (5.3)$$

with L the length of the waveguide, yields the modal gain g_m . However, in our waveguides light can be reflected from the back facet of the waveguide, which in turn can be amplified. Accounting for these reflections R , Equation (5.3) becomes:

$$I(L) = A_0 \left[\frac{e^{g_m L} - 1}{g_m} + \frac{R}{g_m} e^{2g_m L} (1 - e^{-g_m L}) \right] \quad (5.4)$$

Note that this relation is only valid when the collection efficiency from the waveguide facet to the optical fiber is the same for each waveguide. Therefore, it is crucial to optimize the alignment for each waveguide-measurement. This alignment can be facilitated by connecting a red laser-diode to the optical fiber, as shown in Figs. 5.3b-c. When fiber and waveguide are well aligned – and the waveguide quality is good, *i.e.* the light is guided well – a bright red scattering spot appears at the other end of the waveguide. Figure 5.6b shows the measured output power versus waveguide length (red

dots), for a fixed pump intensity of 1 mW, which corresponds to saturation (see Fig. 5.6a). Again, an exponential increase of the output power was observed for waveguide lengths between 200 – 250 μm . By fitting the length dependent output power within the region of exponential increase with Eq. (5.4), the net modal gain g_m can be estimated to be equal to 553 – 303 cm^{-1} for R varying between 0 – 5%. From simulation, the confinement factor of the fundamental TE mode profile was found to be equal to $\Gamma = 0.31$. Considering a filling factor of $f = 0.5$, a material gain equal to 1955 cm^{-1} (for $R = 5\%$) is found, which agrees well with the maximum material gain measured using TAS. For comparison, the waveguide-length dependent output for waveguides embedded with the CdSe/CdS QD sample of reference⁷, with QD dimensions $d_c = 4$ nm and $d_{\text{qd}} = 11.47$ nm, are plotted as blue square markers. Again using Eq. (5.4) with $R = 0$ – 5%, a net modal gain between 398 – 193 cm^{-1} is found. This corresponds to a material gain g_i of 1245 cm^{-1} (for $R = 5\%$), which is lower than the material gain of our new optimized sample. Indeed, as predicted, our new thinner shelled QD sample results in a higher maximum material gain.

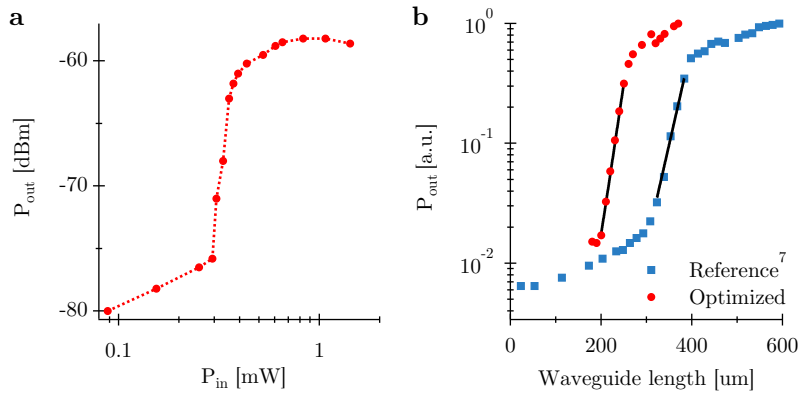


Figure 5.6: (a) $P_{\text{out}} - P_{\text{in}}$ measurement of a 4 μm wide waveguide with $L = 400$ μm . (b) P_{out} for increasing waveguide length L , for waveguides embedded with (red dots) the optimized QD sample and (blue squares) the QD sample used in reference⁷. The region of exponential increase is fitted with Eq. (5.3) (black).

5.3 DFB grating design and fabrication

Like in any laser structure, a DFB laser has an optical cavity which provides optical feedback. However, in this case it is not two discrete mirrors which form the optical cavity, but rather a grating distributed along the entire length of the active region, hence the name *distributed feedback* laser. The grating is designed to reflect only a narrow band of wavelengths and can be easily fabricated on top of a waveguide using electron beam lithography. Such a grating usually exhibits two modes, with wavelengths equally spaced around the Bragg-wavelength. However, for most applications a single-mode laser is preferred. By introducing an additional $\lambda/4$ phase-shifter in the center of the cavity the degeneracy of the two modes is lifted, forcing the laser in a single mode at the Bragg-wavelength. Such devices have a high reproducibility in terms of wavelength and are theoretically all single mode-lasers. This, together with its straightforward fabrication process, makes a DFB design an attractive choice for developing an integrated single mode laser with relatively low lasing thresholds. Its fabrication procedure is very similar to the one of the VSL-sample in previous section, but requires an additional e-beam lithography step to define the grating in the top silicon nitride layer, as illustrated in Fig. 5.7. This step is done before the waveguide patterning and consists of an e-beam lithography step with AR-P 6200.09, after which the pattern is transferred to the top SiN-layer through RIE (CF_4/H_2), followed by an additional RIE (O_2) step to remove the residual resist (see steps b-c). The grating pattern is made several times wider than the final waveguide width to reduce the alignment-restriction between the two lithography steps.

To optimize the grating parameters such as period Λ , number of periods, duty cycle and etch depth, 1D FDTD simulations can be carried out. These kind of simulations can provide information about the stopband, Bragg-wavelength and reflectivity of the grating. Figure 5.8 shows the simulated stopband as a function of Λ , for a 75 nm/50 nm/90 nm $\text{SiN}_x/\text{QD}/\text{SiN}_x$ stack with a 35 nm deep etched grating. The ASE-spectrum collected from a waveguide with an identical stack of $\text{SiN}_x/\text{QD}/\text{SiN}_x$ as in our final DFB-devices, is added for comparison. Ideally, this ASE-peak should fall within the stopband and the period should be chosen accordingly. From Fig. 5.8 it is already clear that the stopband is very sensitive to the grating period, but also the thicknesses of the individual layers and the final etching depth of the grating determines the position of the stopband. *E.g.* a deeper etched grating results in a lower overall effective refractive index and hence shifts the stopband towards shorter wavelengths. Given the uncertainties on the

thicknesses of the individual layers and grating period during fabrication, rather than repeating these simulations for the exact dimensions, we fabricated an array of DFB devices with a sweep over the grating period ranging from $\Lambda = 185 - 195$ nm, and fixed duty cycle of 0.5. Additional simulations showed that 100 periods in combination with a 35 nm etched grating can already provide a high reflection of about 95%. The depth of the grating etch will also determine the reflectivity of the grating, where a deeper etch results in higher reflectivity but also a wider stopband. The $\text{SiN}_x/\text{QD}/\text{SiN}_x$ stack of the final fabricated devices was respectively 69 nm/45 nm/96 nm with a grating etch depth of 32 nm, as found from the cross section of the device shown in Fig. 5.9b. A SEM image of the final device around the phase-shifter area is shown in Fig. 5.9a.

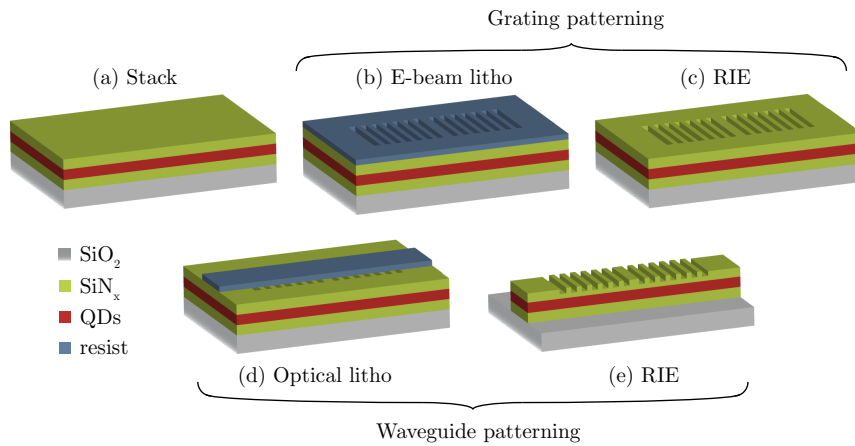


Figure 5.7: Fabrication flow of DFB-laser: (a) Starting from a stack of LF-H-SiN/QD/MF-H-SiN, a grating structure is patterned in the top silicon nitride layer by means of (b) e-beam lithography and (c) RIE. Next, the waveguide is defined using (d) optical lithography and (e) a final RIE step.

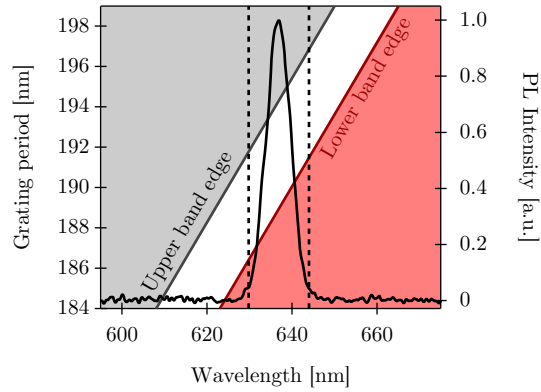


Figure 5.8: The simulated stopband (white region) for a DFB-structure consisting of a $3\ \mu\text{m}$ SiO_2 substrate, $75\ \text{nm}/50\ \text{nm}/90\ \text{nm}$ $\text{SiN}_x/\text{QD}/\text{SiN}_x$ stack and an etched grating of $35\ \text{nm}$ deep and duty cycle 0.5 . The ASE-spectrum of the new QD sample is added in black. Adapted from reference⁷.

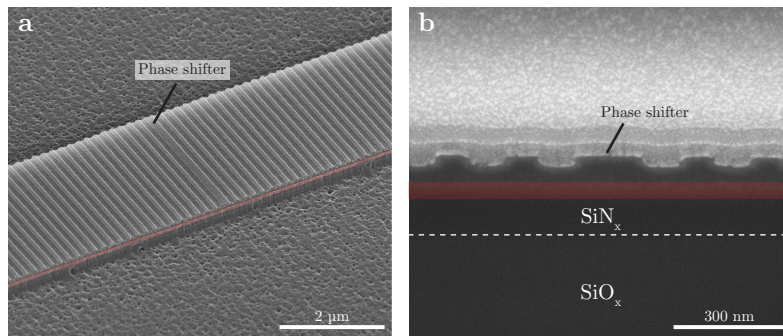


Figure 5.9: SEM images of fabricated device with (a) a tilted view of the region near the phase-shifter and (b) cross section of the same region.

5.4 Measurements and discussion

Since we aim at developing a CW-pumped integrated laser, and fs-pumping was already extensively studied on similar devices (but with different QDs) in reference⁷, we focussed on pumping with longer pulses. The devices were pumped using a nanosecond laser in a setup almost identical to the one used for the VSL-measurements; a pump-laser beam is focussed using a cylindrical lens to pump the DFB-laser from the top and the emission from the waveguide facet is collected by a multimode fiber. A camera image of the devices is shown in Fig. 5.10. Note that when a DFB-waveguide is pumped above threshold, one can see the lasing output as a bright red spot at the waveguide facet.

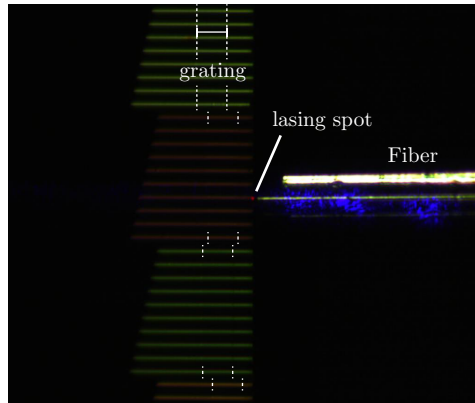


Figure 5.10: Camera image of array of DFB lasers. For clarity, the grating area is indicated by white dashed lines. The bright red spot is the lasing output of the pumped DFB.

To determine the lasing threshold as a function of pump fluence, the pump beam was first characterised. The pump laser is a Q-switched frequency doubled Nd:YAG laser (532 nm) with 7 ns pulses and a repetition rate of 938 Hz. The power distribution of the pump beam, after focusing, can be written as

$$I(x, y) = A_x A_y e^{-\frac{x^2}{w_x^2}} e^{-\frac{y^2}{w_y^2}} \quad (5.5)$$

with w_x and w_y the horizontal and vertical width of the pump beam. These were measured using a Thorlabs BC106N beam profiler (see Fig. 5.11), resulting in an estimate beam width of $w_x = 4551 \mu\text{m}$ and $w_y = 162 \mu\text{m}$ respectively. The maximum power density in the center of the focused beam

can be written as

$$P_{\max} = A_x A_y = \frac{P}{\pi w_x w_y} \quad (5.6)$$

This is the power that actually reaches the DFB-laser in the center of the pump beam. Figure 5.12a plots the collected emission spectra at high pump fluence for the devices with grating period $\Lambda = 184 - 187$ nm. These modes are spectrally shifted by 2.76 nm as a result of the 1 nm Λ -sweep. It can be seen that the lasers indeed operate in the single mode regime. The peaks have a FWHM = 0.8 nm, which is at the limit of the spectrometer's resolution. Figure 5.12b shows the measured output intensity versus the pump fluence for $\Lambda = 186$ nm, showing a clear threshold around 46 $\mu\text{J}/\text{cm}^2$. The biexciton lifetime of the used QDs was found to be equal to ≈ 350 ps, which is much shorter than the 7 ns pump pulses. Therefore, the pump can actually already be considered as quasi-CW. The equivalent CW-pump threshold, found by taking into account the length of the pump pulses, is equal to 6.6 kW/cm^2 , which is a factor of 6 lower compared to the devices fabricated in reference⁷. These estimated CW-thresholds are on the same order of magnitude as the CW-lasing threshold demonstrated by Fan *et al.*¹¹, where they used uniform biaxial strain in CdSe/CdS QDs to lower the band-edge degeneracy. Therefore the prospects of CW operation with these QD-DFB lasers look very promising.

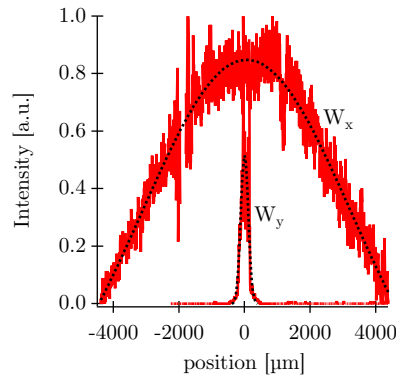


Figure 5.11: Horizontal and vertical crosssection of the pump beam after focussing (red), fitted with gaussian functions (black).

The next step would be to gradually increase the pump pulse duration as to see how close we can get to actual CW-operation with these devices. The best approach is to use a CW-pump laser which can be modulated with an acousto-optic modulator (AOM) from micro-seconds all the way to CW. So

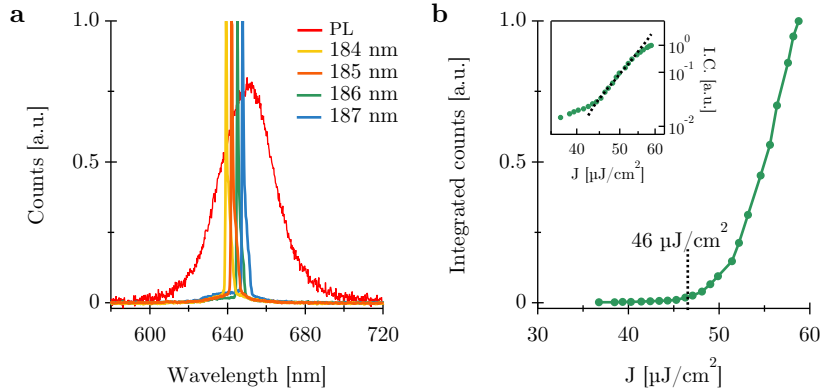


Figure 5.12: (a) Collected emission spectra at high pump fluence for devices with $\Lambda = 184 - 187$ nm. The PL-spectrum measured from a slab waveguide is shown as reference. (b) Measured output intensity as a function of the pump fluence for $\Lambda = 186$ nm, which show a clear threshold around $46 \mu\text{J}/\text{cm}^2$. The inset plots the same data on a double log-scale, showing the typical S-shaped curve.

far, we have unfortunately not been able to demonstrate μs pumping, as the available CW-laser did not allow to be focused well enough to reach the pump fluence necessary for lasing. Although at this moment, we are merely limited by the lack of a proper high power CW-pump laser, one should already think about the possible challenges and ways to improve the lasing threshold even further. One important challenge will be the generated heat associated with these relatively high pumping fluences, as this quenches the emission of the QDs. Therefore it may be relevant to provide on-chip heat sinking structures to avoid local heating.

The CW-lasing threshold can be further improved by either optimizing the DFB structure (*e.g.* designing a cavity with higher optical Q) or by further improving the gain material itself. For the latter, there are several possible approaches. As shown in previous work,^{4;12} using low temperature SiN_x as top layer greatly improves the preservation of the QD's optical properties. However the lower refractive index and lower quality of the silicon nitride associated with this low temperature deposition, could pose a problem. Another, more realistic, approach would be to grow an additional protective ZnS shell around the QDs, which protects the QDs during the fabrication steps. Figure 5.13 compares the PL-intensity of a thin film of CdSe/CdS QDs and CdSe/CdS/ZnS respectively. It can be seen that the

PL-intensity after embedding is up to 3 times higher. One could also think about making denser QD films, *e.g.* by using shorter inorganic ligands as demonstrated by Adachi *et al.*¹³, which results in a higher modal gain and thermal conductivity in the QD-film.

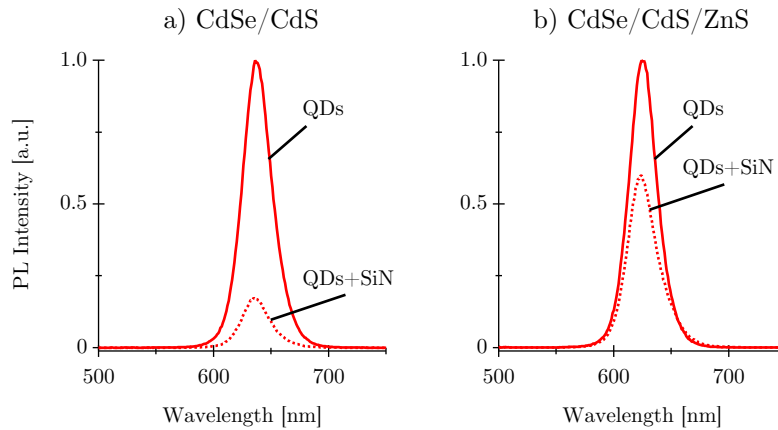


Figure 5.13: Relative PL-intensity measured on a thin film of (a) CdSe/CdS and (b) CdSe/CdS/ZnS QDs before and after embedding them in SiN_x.

5.5 Conclusion

Following the gain characterisation of different core/shell CdSe/CdS QDs in Chapter 4, a ‘best’ sample was chosen. This optimized gain material was integrated in silicon nitride waveguides to form waveguide-amplifiers and DFB-lasers. First we presented a design and fabrication flow for hybrid QD-SiN components where starting from a colloidal dispersion, simple strip waveguide-amplifiers and finally, fully integrated on-chip lasers were demonstrated. Studying gain in SiN_x/QD/SiN_x strip waveguides, we showed that the experimental modal gain can be interpreted as the product of the material gain of the QDs, their volume fraction and the overlap between the optical mode and the QD-layer. This exemplifies the qualities of material gain as a design parameter, which makes it possible to compare different QDs as gain medium, making it a useful tool for the design and simulation of QD based amplifiers and lasers. In previous work⁷, the first truly integrated QD-laser operating under nanosecond pulsed excitation was demonstrated.

Following this work, the new optimized QD sample was integrated in a similar DFB-structure and studied under ns-pulsed pumping. The new devices also showed lasing under ns-pumping with an equivalent CW-lasing threshold of 6.6 kW/cm^2 . This estimated CW-threshold is on the same order of magnitude as the CW-lasing threshold demonstrated by other state-of-the-art QD-lasers.^{11;13} Therefore, although not yet demonstrated in this work, the prospects of CW-operation with these QD-DFB lasers look very promising.

References

- [1] C. Dang, J. Lee, C. Breen, J. S. Steckel, S. Coe-Sullivan, and A. Nurmikko, “Red, green and blue lasing enabled by single-exciton gain in colloidal quantum dot films,” *Nature Nanotechnology*, vol. 7, pp. 335 EP –, 04 2012.
- [2] Y. Chen, J. Herrnsdorf, B. Guilhabert, Y. Zhang, I. M. Watson, E. Gu, N. Laurand, and M. D. Dawson, “Colloidal quantum dot random laser,” *Opt. Express*, vol. 19, pp. 2996–3003, Feb 2011.
- [3] K. Roh, C. Dang, J. Lee, S. Chen, J. S. Steckel, S. Coe-Sullivan, and A. Nurmikko, “Surface-emitting red, green, and blue colloidal quantum dot distributed feedback lasers,” *Opt. Express*, vol. 22, pp. 18800–18806, Jul 2014.
- [4] W. Xie, Y. Zhu, T. Aubert, S. Verstuyft, Z. Hens, and D. V. Thourhout, “Low-loss silicon nitride waveguide hybridly integrated with colloidal quantum dots,” *Opt. Express*, vol. 23, pp. 12152–12160, May 2015.
- [5] Y. Zhu, W. Xie, P. Geiregat, S. Bisschop, T. Aubert, E. Brainis, Z. Hens, and D. van Thourhout, “Hybrid colloidal quantum dot silicon nitride waveguide gain measurement based on variable stripe length method,” in *2016 Conference on Lasers and Electro-Optics (CLEO)*, pp. 1–2, June 2016.
- [6] W. Xie, T. Stöferle, G. Rainò, T. Aubert, S. Bisschop, Y. Zhu, R. F. Mahrt, P. Geiregat, E. Brainis, Z. Hens, and D. Van Thourhout, “On-chip integrated quantum-dot silicon-nitride microdisk lasers,” *Advanced Materials*, vol. 29, no. 16, pp. 1604866–n/a, 2017. 1604866.
- [7] Y. Zhu, W. Xie, S. Bisschop, T. Aubert, E. Brainis, P. Geiregat, Z. Hens, and D. Van Thourhout, “On-chip single-mode distributed feedback colloidal quantum dot laser under nanosecond pumping,” *ACS Photonics*, vol. 4, no. 10, pp. 2446–2452, 2017.
- [8] A. Nurmikko, “What future for quantum dot-based light emitters?,” *Nature Nanotechnology*, vol. 10, pp. 1001 EP –, 12 2015.
- [9] L. Negro, P. Bettotti, M. Cazzanelli, D. Pacifici, and L. Pavesi, “Applicability conditions and experimental analysis of the variable stripe length method for gain measurements,” *Optics Communications*, vol. 229, no. 1, pp. 337 – 348, 2004.
- [10] K. Shaklee, R. Nahory, and R. Leheny, “Optical gain in semiconductors,” *Journal of Luminescence*, vol. 7, pp. 284 – 309, 1973.

-
- [11] F. Fan, O. Voznyy, R. P. Sabatini, K. T. Bicanic, M. M. Adachi, J. R. McBride, K. R. Reid, Y.-S. Park, X. Li, A. Jain, R. Quintero-Bermudez, M. Saravanapavanantham, M. Liu, M. Korkusinski, P. Hawrylak, V. I. Klimov, S. J. Rosenthal, S. Hoogland, and E. H. Sargent, “Continuous-wave lasing in colloidal quantum dot solids enabled by facet-selective epitaxy,” *Nature*, vol. 544, pp. 75 EP –, 03 2017.
- [12] W. Xie, Y. Zhu, S. Bisschop, T. Aubert, Z. Hens, D. van Thourhout, and P. Geiregat, “Colloidal quantum dots enabling coherent light sources for integrated silicon-nitride photonics,” *IEEE Journal of Selected Topics in Quantum Electronics*, vol. 23, pp. 1–13, Sept 2017.
- [13] M. M. Adachi, F. Fan, D. P. Sellan, S. Hoogland, O. Voznyy, A. J. Houtepen, K. D. Parrish, P. Kanjanaboos, J. A. Malen, and E. H. Sargent, “Microsecond-sustained lasing from colloidal quantum dot solids,” *Nature Communications*, vol. 6, p. 8694, 2015.

6

Conclusions and perspectives

In this thesis, the potential of colloidal QDs as active material for integrated light sources was explored. Colloidal QDs, showing both single-photon emission and optical gain under different pumping conditions, can be used to realise single-photon sources as well as integrated lasers. Specifically, we focused on the visible light range by using the silicon nitride platform and CdSe/CdS core/shell QDs. However, several results are generic and independent of the specific QD materials used.

6.1 Single-photon sources with colloidal QDs

Single-photon sources are important for a number of optical quantum information processing applications. We studied the possibility to integrate triggered solid-state SP emitters directly on a photonic chip. A major challenge consists in efficiently extracting their emission into a single guided mode. Our study showed that high efficiency in-plane SP sources can in principal be realized using SiN_x photonic devices as simple as waveguides. Using 3D finite-difference time-domain simulations, we investigated the SP emission from dipole-like nanometer-sized inclusions embedded into different silicon nitride (SiN_x) photonic nanowire waveguide designs. We showed that light

from a SP emitter can be efficiently coupled to the waveguide. High coupling factors β ranging between 40% and 67% were found in the four waveguide geometries under investigation. Furthermore, we showed that under certain geometrical conditions, the emitted photon can be coupled to a single polarized guided (TE or TM) mode. In that case, an effective polarized SP source is built even if the SP emitter itself is unpolarized. In suspended strip waveguides, we showed that one can simultaneously achieve a good coupling factor $\beta = 43\%$ and a high polarization ratio $\beta_y/\beta = 95\%$. While in suspended slot waveguides a higher coupling factor $\beta = 56\%$ is achievable in combination with a similar polarization ratio $\beta_z/\beta = 96\%$. These results demonstrate that high efficiency single-photon sources and complex optical circuits can be combined on a single photonic chip for quantum optic experiments. Finally, these SiN_x sources and optical circuits can be manufactured using well-established CMOS-compatible processing technology. Because the SiN_x transparency range extends from the visible to the infrared, the envisaged platform is compatible with several types of SP emitting inclusions such as colloidal quantum dots, nanoparticles containing a single color centre, and single-ion doped nanoparticles.

The coupling of single-photon emitters to dielectric cavities or plasmonic cavities/antennas has been demonstrated using a variety of physical systems with the goal of making the source brighter and more directive. However most of these approaches are based on the random deposition of emitters, which strongly reduces the fabrication yield. This is one of the challenges that is often overlooked for having a truly scalable single-photon source. We have developed a straightforward fabrication method, based on e-beam lithography that allows a precise control on the positioning of both emitter and cavity. More specifically we demonstrated that a uniform monolayer of colloidal QDs can be precisely positioned in the center of a sub-wavelength SiN_x/Au cavity, which can be further patterned down to a single QD in future experiments. However, to develop such a SP source, it is crucial to study the SP properties of the emitter itself to determine which kind of dots have superior SP properties (eg. InP/ZnSe as shown in¹) and more importantly, which ones preserve these properties after embedding/patterning. As our fabrication method is compatible with any colloidal QD material, the final combination of the best emitter with our nanopatch cavities does not pose any additional challenges. Although there are other approaches that combine deterministic positioning of epitaxial dots with a dielectric cavity,²⁻⁴ these cavities are generally more bulky and still have a lower yield compared to our patterning technique. Our metallic nanopatches combine the benefits of moderate Q-factors (making them

suitable for room-temperature operation) with a small mode volume, while not exhibiting the large optical losses generally found in plasmonic cavities. Finally we have also studied and clarified the non-exponential behaviour of the decay traces when an emitter is placed off-center or in the case of a film of multiple emitters. Although the speed-up of the spontaneous emission of these QD monolayers is modest, the expected radiative efficiency for these single-photon cavities is high compared to plasmonic cavities with stronger Purcell enhancement. The circular shape of our cavities, together with the mode profile of the targeted mode and the possibility to deterministically position both cavity and emitter allows for a robust and reproducible SP source. As the patterning and cavity fabrication can be seen as two independent fabrication steps with respective yields of 40% and 100%, we can estimate that the yield of these scalable single-photon sources can be up to 40%.

6.2 Optical gain with colloidal QDs

We have explored the possibility to achieve on-chip amplifiers and lasers with colloidal QDs as the gain material. After the first demonstrations of optical gain in colloidal QDs, several efforts have been made to improve the overall lasing performance of these materials. Although this optimization mainly focused on strategies that reduce the gain threshold, the role of the gain coefficient to reach lasing action should not be overlooked. To this end we have introduced the concept of material gain which can be used to quantify gain. This material gain can be conveniently obtained from a normalization of the non-linear absorbance, which is measured using TAS. It is a convenient characteristic of colloidal QDs, as it allows to study and compare different QD morphologies on the same footing. At the same time, TAS also allows to directly measure the more classically studied parameters $\langle N \rangle_{\text{th}}$, J_{th} and τ_g . We studied the relation between the structure of CdSe/CdS core/shell QDs, the material gain they can deliver and the threshold needed to attain net stimulated emission by optical pumping. Based on a simplified model, we predicted that reducing the thickness of the CdS shell grown around a given CdSe core will increase the maximal material gain, while increasing the shell thickness will lower the gain threshold. Our results confirmed that thin-shell QDs exhibit the highest gain coefficients, in quantitative agreement with the model, but the significant threshold reduction expected for thick-shell QDs is absent. By simulating the transient absorption spectra, we could relate this increasing gain thresholds for thicker-shell QDs to a transition from an exciton-exciton repulsion (redshift) to attraction (blueshift) with increasing shell thickness.

In addition, we showed that this reduction in $\langle N \rangle_{\text{th}}$ for large core thin shell QDs can result in extremely long-lived gain, up to 800 ps, which is quite fascinating given the short Auger lifetimes of the excited states (200 – 400 ps). The inversion lifetime is an important parameter in the context of CW pumping – a long sought after breakthrough in QD opto-electronics – as this number is a figure of merit for the rate at which the sample needs to be pumped to maintain lasing. This makes large-core/thin-shell QDs the overall champion core/shell configuration in terms of both material gain, gain threshold and gain lifetime. These insights are most valuable to guide future work to improve colloidal QDs for optical gain applications and develop optimized QD-lasers. In addition, the concept of material gain and its measurement technique is generic and can in principle be applied to future solution-processable colloidal materials such as the promising 2D ‘nanoplatelets’.^{5;6}

By qualitatively studying the gain properties of several CdSe/CdS QDs we decided upon a ‘best’ QD sample to be used as gain material for integrated lasers. Starting from a colloidal dispersion, simple $\text{SiN}_x/\text{QD}/\text{SiN}_x$ strip waveguide amplifiers were fabricated using the hybrid integration platform developed in previous work.^{7;8} Studying the light amplification in these strip waveguides, we showed that the experimental modal gain can be interpreted as the product of the material gain of the QDs, their volume fraction and the overlap between the optical mode and the QD layer. This exemplifies the qualities of material gain as a design parameter, as it makes it possible to study and compare different QD morphologies or material systems in terms of gain, even without fabricating the actual device. Next, an integrated QD-DFB-laser was fabricated using this optimized QD sample, based on the design and fabrication procedure developed by Zhu *et al.*⁹ Such waveguide coupled DFB lasers require little processing steps and are truly single mode. These devices showed lasing under ns-pumping with an equivalent CW-lasing threshold of 6.6 kW/cm^2 , which is a factor 6 lower compared to the devices in reference⁹. This estimated CW-threshold is on the same order of magnitude as the CW-lasing threshold demonstrated by other state-of-the-art QD-lasers.^{10;11} The next step would be to gradually increase the pump pulse duration as to see how close we can get to actual CW-operation with these devices. Yet also some other challenges remain, such as the heat generation associated with pumping at such high pump fluences. Therefore it may be relevant to provide on-chip heat sinking structures to avoid local heating. Nevertheless, these devices would benefit from a further reduction of the CW-lasing threshold, as it would result in less harsh pumping conditions. One could possibly try to improve the

cavities, *e.g.* by designing a cavity with higher optical Q. However, there is possibly more room for improvement in the gain material itself. A first and straightforward step would be to grow an additional protective ZnS shell around the QDs, which helps to better preserve the optical properties during device fabrication. Another approach could be exchanging the long organic ligands for shorter inorganic ligands¹⁰, which would result in higher packing densities with better thermal conductivity. Finally, one can also look into other promising solution-processable gain materials, such as nanoplatelets. However, still much effort is needed in better understanding the gain mechanisms in these materials and they are generally less stable during processing. Even though the final goal of achieving a CW pumped integrated QD-laser was not reached in this work, the potential for colloidal QDs to enhance the SiN-platform was demonstrated, clearly pointing towards the potential of QD based gain media to reach low enough threshold densities in the near future.

References

- [1] V. Chandrasekaran, M. D. Tessier, D. Dupont, P. Geiregat, Z. Hens, and E. Brainis, “Nearly blinking-free, high-purity single-photon emission by colloidal inp/znse quantum dots,” *Nano Letters*, vol. 17, no. 10, pp. 6104–6109, 2017.
- [2] J. Claudon, J. Bleuse, N. S. Malik, M. Bazin, N. Gregersen, C. Sauvan, P. Lalanne, and Gerard, “A highly efficient single-photon source based on a quantum dot in a photonic nanowire,” *Nature Photonics*, vol. 4, no. March, pp. 174–177, 2010.
- [3] G. Juska, V. Dimastrodonato, L. O. Mereni, A. Gocalinska, and E. Pelucchi, “Towards quantum-dot arrays of entangled photon emitters,” *Nature Photonics*, vol. 7, pp. 527 EP –, 05 2013.
- [4] C. Schneider, T. Heindel, A. Huggenberger, P. Weinmann, C. Kistner, M. Kamp, S. Reitzenstein, S. Höfling, and A. Forchel, “Single photon emission from a site-controlled quantum dot-micropillar cavity system,” *Applied Physics Letters*, vol. 94, no. 11, p. 111111, 2009.
- [5] J. Q. Grim, S. Christodoulou, F. Di Stasio, R. Krahne, R. Cingolani, L. Manna, and I. Moreels, “Continuous-wave biexciton lasing at room temperature using solution-processed quantum wells,” *Nature Nanotechnology*, vol. 9, pp. 891 EP –, 10 2014.
- [6] Z. Yang, M. Pelton, I. Fedin, D. V. Talapin, and E. Waks, “A room temperature continuous-wave nanolaser using colloidal quantum wells,” *Nature Communications*, vol. 8, no. 1, p. 143, 2017.
- [7] W. Xie, Y. Zhu, T. Aubert, S. Verstuyft, Z. Hens, and D. V. Thourhout, “Low-loss silicon nitride waveguide hybridly integrated with colloidal quantum dots,” *Opt. Express*, vol. 23, pp. 12152–12160, May 2015.
- [8] Y. Zhu, W. Xie, P. Geiregat, S. Bisschop, T. Aubert, E. Brainis, Z. Hens, and D. van Thourhout, “Hybrid colloidal quantum dot silicon nitride waveguide gain measurement based on variable stripe length method,” in *2016 Conference on Lasers and Electro-Optics (CLEO)*, pp. 1–2, June 2016.
- [9] Y. Zhu, W. Xie, S. Bisschop, T. Aubert, E. Brainis, P. Geiregat, Z. Hens, and D. Van Thourhout, “On-chip single-mode distributed feedback colloidal quantum dot laser under nanosecond pumping,” *ACS Photonics*, vol. 4, no. 10, pp. 2446–2452, 2017.

-
- [10] M. M. Adachi, F. Fan, D. P. Sellan, S. Hoogland, O. Voznyy, A. J. Houtepen, K. D. Parrish, P. Kanjanaboos, J. A. Malen, and E. H. Sargent, “Microsecond-sustained lasing from colloidal quantum dot solids,” *Nature Communications*, vol. 6, p. 8694, 2015.
- [11] F. Fan, O. Voznyy, R. P. Sabatini, K. T. Bicanic, M. M. Adachi, J. R. McBride, K. R. Reid, Y.-S. Park, X. Li, A. Jain, R. Quintero-Bermudez, M. Saravanapavanantham, M. Liu, M. Korkusinski, P. Hawrylak, V. I. Klimov, S. J. Rosenthal, S. Hoogland, and E. H. Sargent, “Continuous-wave lasing in colloidal quantum dot solids enabled by facet-selective epitaxy,” *Nature*, vol. 544, pp. 75 EP –, 03 2017.

A

Appendix

A.1 Derivation of Eq. (1.22): QED in vacuum

Combining Eqs. (1.19) and (1.20), the Fermi Golden Rule yields:

$$\Gamma^{(\text{QED})} = \frac{\pi}{\hbar} \frac{\omega_{ab}}{\epsilon_0} \sum_{\lambda} |\mathbf{d}_{ab} \cdot \mathbf{v}_{\lambda}(\mathbf{r}_0)|^2 \delta(\omega_{\lambda} - \omega_{ab}). \quad (\text{A.1})$$

The quantity $|\mathbf{d}_{ab} \cdot \mathbf{v}_{\lambda}(\mathbf{r}_0)|^2$ can be written as

$$|\mathbf{d}_{ab} \cdot \mathbf{v}_{\lambda}(\mathbf{r}_0)|^2 = (\mathbf{d}_{ab}^* \cdot \mathbf{v}_{\lambda}^*(\mathbf{r}_0)) (\mathbf{v}_{\lambda}(\mathbf{r}_0) \cdot \mathbf{d}_{ab}). \quad (\text{A.2})$$

If we represent the dipole moment \mathbf{d}_{ab} by a column matrix and its adjoint by a row matrix,

$$\mathbf{d}_{ab} \mapsto \begin{pmatrix} d_{ab,x} \\ d_{ab,y} \\ d_{ab,z} \end{pmatrix} \quad (\text{A.3})$$

$$\mathbf{d}_{ab}^{\dagger} \mapsto \left(d_{ab,x}^* \quad d_{ab,y}^* \quad d_{ab,z}^* \right), \quad (\text{A.4})$$

and do the same for \mathbf{v}_λ and $\mathbf{v}_\lambda^\dagger$,

$$\mathbf{v}_\lambda \mapsto \begin{pmatrix} v_{\lambda,x} \\ v_{\lambda,y} \\ v_{\lambda,z} \end{pmatrix} \quad (\text{A.5})$$

$$\mathbf{v}_\lambda^\dagger \mapsto \begin{pmatrix} v_{\lambda,x}^* & v_{\lambda,y}^* & v_{\lambda,z}^* \end{pmatrix}, \quad (\text{A.6})$$

we see that

$$|\mathbf{d}_{ab} \cdot \mathbf{v}_\lambda(\mathbf{r}_0)|^2 = \mathbf{d}_{ab}^\dagger \mathbf{v}_\lambda(\mathbf{r}_0) \mathbf{v}_\lambda^\dagger(\mathbf{r}_0) \mathbf{d}_{ab}, \quad (\text{A.7})$$

where the dyadic product $\mathbf{v}_\lambda(\mathbf{r}_0) \mathbf{v}_\lambda^\dagger(\mathbf{r}_0)$ represents a 3×3 matrix. The decay rate can then reads as

$$\Gamma^{(\text{QED})} = \frac{\pi}{\hbar} \frac{\omega_{ab}}{\epsilon_0} \sum_\lambda \mathbf{d}_{ab}^\dagger \mathbf{v}_\lambda(\mathbf{r}_0) \mathbf{v}_\lambda^\dagger(\mathbf{r}_0) \mathbf{d}_{ab} \delta(\omega_\lambda - \omega_{ab}) \quad (\text{A.8})$$

$$= \frac{\pi}{\hbar} \frac{\omega_{ab}}{\epsilon_0} \mathbf{d}_{ab}^\dagger \left[\sum_\lambda \mathbf{v}_\lambda(\mathbf{r}_0) \mathbf{v}_\lambda^\dagger(\mathbf{r}_0) \delta(\omega_\lambda - \omega_{ab}) \right] \mathbf{d}_{ab}. \quad (\text{A.9})$$

At this point, a connection with the electromagnetic Green tensor can be made. Indeed, it can be shown (see Novotny-Hecht¹) that the Green tensor expands on the normal modes in the following way:

$$\mathcal{G}(\mathbf{r}, \mathbf{r}', \omega) = c^2 \sum_\lambda \frac{\mathbf{v}_\lambda(\mathbf{r}) \mathbf{v}_\lambda^\dagger(\mathbf{r}')}{\omega_\lambda^2 - \omega^2}. \quad (\text{A.10})$$

On the other hand

$$\lim_{\eta \rightarrow 0} \Im \left[\frac{1}{\omega_\lambda^2 - (\omega + i\eta)^2} \right] = \frac{\pi}{2\omega_\lambda} [\delta(\omega - \omega_\lambda) + \delta(\omega + \omega_\lambda)], \quad (\text{A.11})$$

$$= \frac{\pi}{2\omega} \delta(\omega - \omega_\lambda). \quad (\text{A.12})$$

Therefore,

$$\Im \mathcal{G}(\mathbf{r}, \mathbf{r}', \omega) = \frac{\pi}{2\omega} \frac{c^2}{\epsilon_0} \sum_\lambda \mathbf{v}_\lambda(\mathbf{r}) \mathbf{v}_\lambda^\dagger(\mathbf{r}') \delta(\omega - \omega_\lambda). \quad (\text{A.13})$$

Injecting this result in the expression (A.9) of the Fermi Golden Rule,

$$\Gamma^{(\text{QED})} = \frac{2}{\hbar} \frac{\omega_{ab}^2}{\epsilon_0 c^2} \left\{ \mathbf{d}_{ab}^\dagger \Im [\mathcal{G}(\mathbf{r}_0, \mathbf{r}_0, \omega_{ab})] \mathbf{d}_{ab} \right\}, \quad (\text{A.14})$$

$$= \frac{2}{\hbar} \frac{\omega_{ab}^2}{\epsilon_0 c^2} |\mathbf{d}_{ab}|^2 \left\{ \mathbf{n}_{ab}^\dagger \Im [\mathcal{G}(\mathbf{r}_0, \mathbf{r}_0, \omega_{ab})] \mathbf{n}_{ab} \right\}, \quad (\text{A.15})$$

where \mathbf{n}_{ab} is the unit vector in the direction of the dipole moment \mathbf{d}_{ab} . The form (A.15) of the Fermi Golden rule is very convenient because it allows a straightforward generalization to complex, structured, and even lossy dielectrics. Also notice that (A.15) applies to metallic cavities (as long as there is no dielectric material), and of course to free vacuum space. In *free space* (see Ref.¹),

$$\mathbf{n}_{ab}^\dagger \Im[\mathcal{G}(\mathbf{r}_0, \mathbf{r}_0, \omega_{ab})] \mathbf{n}_{ab} = \frac{1}{3} \Im[\text{Tr}(\mathcal{G}(\mathbf{r}_0, \mathbf{r}_0, \omega_{ab}))] = \frac{\omega_{ab}}{6\pi c} \quad (\text{A.16})$$

is independent of the dipole direction. Therefore,

$$\Gamma_0^{(\text{QED})} = \frac{\omega_{ab}^3 |\mathbf{d}_{ab}|^2}{3\pi \hbar \epsilon_0 c^3}, \quad (\text{A.17})$$

is the decay rate in free space vacuum, a well know result. The Fermi Golden Rule can thus be written as follows:

$$\frac{\Gamma^{(\text{QED})}}{\Gamma_0^{(\text{QED})}} = \frac{6\pi c}{\omega_{ab}} \left\{ \mathbf{n}_{ab}^\dagger \Im[\mathcal{G}(\mathbf{r}_0, \mathbf{r}_0, \omega_{ab})] \mathbf{n}_{ab} \right\}. \quad (\text{A.18})$$

A.2 Derivation of Eqs. (3.6a) and (3.6b)

Consider a simple non degenerate dipole transition $|b\rangle \rightarrow |a\rangle$ with a dipole moment matrix element \mathbf{d}_{ab} . The rate of spontaneous emission from $|b\rangle$ to $|a\rangle$ is given by the *Fermi Golden Rule*

$$\Gamma = \Gamma_0 \frac{\mathbf{d}_{ab}^\dagger \mathcal{F} \mathbf{d}_{ab}}{|\mathbf{d}_{ab}|^2} \quad (\text{A.19})$$

where \mathcal{F} is the *Purcell tensor*

$$\mathcal{F} = \frac{6\pi c}{\omega_{ab} n^3} \Im \mathcal{G}(\mathbf{r}_0, \mathbf{r}_0, \omega_{ab}) \quad (\text{A.20})$$

defined using the *electromagnetic Green tensor* \mathcal{G} . The point \mathbf{r}_0 is the position of the source and ω_{ab} is the frequency of the transition. The reciprocity principal in electromagnetism imposes that the Green tensor is symmetric : $G_{ij}(\mathbf{r}, \mathbf{r}', \omega) = G_{ji}(\mathbf{r}', \mathbf{r}, \omega)$. Therefore, the Purcell tensor can be represented by a symmetric 3×3 matrix with only *6 independent components*:

$$\mathcal{F} \mapsto F = \begin{pmatrix} F_{xx} & F_{xy} & F_{xz} \\ F_{xy} & F_{yy} & F_{yz} \\ F_{xz} & F_{yz} & F_{zz} \end{pmatrix}. \quad (\text{A.21})$$

The number of independent components can be further reduced due to the *symmetry of the photonic system*. Indeed, if the system is invariant under a symmetry operation represented by the matrix Q , so must be the tensor:

$$F = Q F Q^T. \quad (\text{A.22})$$

A.2.1 Rotation by an angle $\theta = \pi/2$ around the z -axis

Consider a system with a rotation symmetry around the z -axis. For such rotations, the Q matrix is

$$Q_\theta = \begin{pmatrix} \cos \theta & -\sin \theta & 0 \\ \sin \theta & \cos \theta & 0 \\ 0 & 0 & 1 \end{pmatrix}. \quad (\text{A.23})$$

For $\theta = \pi/2$

$$Q_{\frac{\pi}{2}} = \begin{pmatrix} 0 & -1 & 0 \\ 1 & 0 & 0 \\ 0 & 0 & 1 \end{pmatrix}. \quad (\text{A.24})$$

Let's find the constraint on the Purcell tensor imposed by the symmetry condition (A.22):

$$\begin{aligned} F Q_{\frac{\pi}{2}}^T &= \begin{pmatrix} F_{xx} & F_{xy} & F_{xz} \\ F_{xy} & F_{yy} & F_{yz} \\ F_{xz} & F_{yz} & F_{zz} \end{pmatrix} \begin{pmatrix} 0 & 1 & 0 \\ -1 & 0 & 0 \\ 0 & 0 & 1 \end{pmatrix} = \begin{pmatrix} -F_{xy} & F_{xx} & F_{xz} \\ -F_{yy} & F_{xy} & F_{yz} \\ -F_{yz} & F_{xz} & F_{zz} \end{pmatrix} \\ Q_{\frac{\pi}{2}} F Q_{\frac{\pi}{2}}^T &= \begin{pmatrix} 0 & -1 & 0 \\ 1 & 0 & 0 \\ 0 & 0 & 1 \end{pmatrix} \begin{pmatrix} -F_{xy} & F_{xx} & F_{xz} \\ -F_{yy} & F_{xy} & F_{yz} \\ -F_{yz} & F_{xz} & F_{zz} \end{pmatrix} = \begin{pmatrix} F_{yy} & -F_{xy} & -F_{yz} \\ -F_{xy} & F_{xx} & F_{xz} \\ -F_{yz} & F_{xz} & F_{zz} \end{pmatrix} \end{aligned}$$

This implies that

$$F_{xx} = F_{yy}, \quad (\text{A.25})$$

$$F_{xy} = -F_{yx} = 0, \quad (\text{A.26})$$

$$F_{xz} = -F_{zx} = F_{yz} = 0. \quad (\text{A.27})$$

In other words, the Purcell tensor reduces to

$$\mathcal{F} \mapsto F = \begin{pmatrix} F_{\parallel} & 0 & 0 \\ 0 & F_{\parallel} & 0 \\ 0 & 0 & F_{\perp} \end{pmatrix}, \quad (\text{A.28})$$

where $F_{\parallel} = F_{xx} = F_{yy}$ and $F_{\perp} = F_{zz}$. If we represent the dipole moment \mathbf{d}_{ab} by a column matrix and its adjoint by a row matrix,

$$\mathbf{d}_{ab} \mapsto \begin{pmatrix} d_{ab,x} \\ d_{ab,y} \\ d_{ab,z} \end{pmatrix} \quad (\text{A.29})$$

$$\mathbf{d}_{ab}^{\dagger} \mapsto \left(d_{ab,x}^* \quad d_{ab,y}^* \quad d_{ab,z}^* \right), \quad (\text{A.30})$$

we see from Eq. (A.19) that

$$F_P = \frac{\Gamma}{\Gamma_0} = F_{\parallel} \left(\frac{|d_{ab,x}|^2}{|\mathbf{d}_{ab}|^2} + \frac{|d_{ab,y}|^2}{|\mathbf{d}_{ab}|^2} \right) + F_{\perp} \frac{|d_{ab,z}|^2}{|\mathbf{d}_{ab}|^2} \quad (\text{A.31})$$

A.2.2 Mirror symmetry through the plane (y, z)

For such reflection, the Q matrix is

$$Q_{(y,z)} = \begin{pmatrix} -1 & 0 & 0 \\ 0 & 1 & 0 \\ 0 & 0 & 1 \end{pmatrix}. \quad (\text{A.32})$$

Let's find the constrain on the Purcell tensor imposed by the symmetry condition (A.22):

$$\begin{aligned} F Q_{(yz)}^T &= \begin{pmatrix} F_{xx} & F_{xy} & F_{xz} \\ F_{xy} & F_{yy} & F_{yz} \\ F_{xz} & F_{yz} & F_{zz} \end{pmatrix} \begin{pmatrix} -1 & 0 & 0 \\ 0 & 1 & 0 \\ 0 & 0 & 1 \end{pmatrix} = \begin{pmatrix} -F_{xx} & F_{xy} & F_{xz} \\ -F_{xy} & F_{yy} & F_{yz} \\ -F_{xz} & F_{yz} & F_{zz} \end{pmatrix} \\ Q_{\frac{\pi}{2}} F Q_{\frac{\pi}{2}}^T &= \begin{pmatrix} -1 & 0 & 0 \\ 0 & 1 & 0 \\ 0 & 0 & 1 \end{pmatrix} \begin{pmatrix} -F_{xx} & F_{xy} & F_{xz} \\ -F_{xy} & F_{yy} & F_{yz} \\ -F_{xz} & F_{yz} & F_{zz} \end{pmatrix} = \begin{pmatrix} F_{xx} & -F_{xy} & -F_{xz} \\ -F_{xy} & F_{yy} & F_{yz} \\ -F_{xz} & F_{yz} & F_{zz} \end{pmatrix} \end{aligned}$$

This implies that

$$F_{xy} = -F_{xy} = 0, \quad (\text{A.33})$$

$$F_{xz} = -F_{xz} = 0. \quad (\text{A.34})$$

In other words, the Purcell tensor reduces to

$$\mathcal{F} \mapsto F = \begin{pmatrix} F_{xx} & 0 & 0 \\ 0 & F_{yy} & F_{yz} \\ 0 & F_{yz} & F_{zz} \end{pmatrix}, \quad (\text{A.35})$$

If we represent the dipole moment \mathbf{d}_{ab} by a column matrix and its adjoint by a row matrix,

$$\mathbf{d}_{ab} \mapsto \begin{pmatrix} d_{ab,x} \\ d_{ab,y} \\ d_{ab,z} \end{pmatrix} \quad (\text{A.36})$$

$$\mathbf{d}_{ab}^\dagger \mapsto \left(d_{ab,x}^* \quad d_{ab,y}^* \quad d_{ab,z}^* \right), \quad (\text{A.37})$$

we see from Eq. (A.19) that

$$F_P = \frac{\Gamma}{\Gamma_0} = F_{xx} \frac{|d_{ab,x}|^2}{|\mathbf{d}_{ab}|^2} + F_{yy} \frac{|d_{ab,y}|^2}{|\mathbf{d}_{ab}|^2} + F_{zz} \frac{|d_{ab,z}|^2}{|\mathbf{d}_{ab}|^2} + 2 F_{yz} \frac{\Re[d_{ab,y} d_{ab,z}^*]}{|\mathbf{d}_{ab}|^2}. \quad (\text{A.38})$$

A.2.3 Discussion

When the emitting dipole is placed in the center of the cavity, the system is symmetric under rotations around the z -axis, in particular rotations by 90 degrees. The tensor element F_{\parallel} is obtained by numerically computing the Purcell factor F_P for a linear dipole in the (x, y) plane ($d_{ab,z} = 0$). The tensor element F_{\perp} is obtained by numerically computing the Purcell factor F_P for a linear dipole along the z -axis ($d_{ab,x} = d_{ab,y} = 0$). However, when the source is moved away from the center (for instance along the y axis), the rotational symmetry is broken. The only symmetry is the mirror symmetry through the (y, z) -plane. The tensor elements F_{xx} , F_{yy} , and F_{zz} are obtained by numerically computing the Purcell factor F_P for a linear dipole vibrating along the x -axis, y -axis, and z -axis respectively. To determine F_{yz} one can compute the Purcell factors $F_P^{(\pm)}$ corresponding to the dipoles $\mathbf{d}_{ab}^{(\pm)} = \frac{|\mathbf{d}_{ab}|}{\sqrt{2}} (\mathbf{e}_y \pm \mathbf{e}_z)$. F_{yz} is then given by

$$F_{yz} = \frac{1}{2} \left(F_P^{(+)} - F_P^{(-)} \right) \quad (\text{A.39})$$

If not for the infinite lower gold layer, the nanopatch cavities would also be symmetric under reflections through the (x, y) -plane. In that case the off-diagonal tensor element F_{yz} would be equal to zero. Because mirror reflection in the (x, y) -plane is a quasi symmetry $F_{yz} \ll 1$. In the nanopatch cavities, $F_{xx} \approx F_{yy}$ (except very far away from the cavity center). With this approximation and $F_{yz} \approx 0$, one can consider that F_P is given by Eq. (A.31). This is what is done in Chapter 3.

A.2.4 \mathbf{d}_{ab} for a π transition

Consider a QD with a c -axis pointing in a direction specified by the polar and azimuthal angles (θ, φ) . A π transition is a transition such that \mathbf{d}_{ab} is a linear dipole along the c -axis:

$$\mathbf{d}_{ab} = |\mathbf{d}_{ab}| (\sin \theta \cos \varphi \mathbf{e}_x + \sin \theta \sin \varphi \mathbf{e}_y + \cos \theta \mathbf{e}_z). \quad (\text{A.40})$$

If Eq. (A.31) applies, we thus find that

$$F_P^\pi = \sin^2 \theta F_{\parallel} + \cos^2 \theta F_{\perp} \quad (\text{A.41})$$

A.2.5 \mathbf{d}_{ab} for a σ transition

A σ transition corresponds to a circular dipole rotating in the plane orthogonal to the c -axis. The dipole can rotate clockwise or counterclockwise (σ_{\pm}). The dipole moment of a sigma transition can be written as

$$\mathbf{d}_{ab} = \frac{|\mathbf{d}_{ab}|}{\sqrt{2}} (\mathbf{e}_1 \pm i \mathbf{e}_2), \quad (\text{A.42})$$

where \mathbf{e}_1 and \mathbf{e}_2 are two orthogonal unit vectors which are simultaneously orthogonal to the unit vector

$$\mathbf{e}_c = \sin \theta \cos \varphi \mathbf{e}_x + \sin \theta \sin \varphi \mathbf{e}_y + \cos \theta \mathbf{e}_z \quad (\text{A.43})$$

pointing in the direction of the c -axis. For instance, one can choose $\mathbf{e}_1 = \frac{\mathbf{e}_z \times \mathbf{e}_c}{|\mathbf{e}_z \times \mathbf{e}_c|}$ and $\mathbf{e}_2 = \mathbf{e}_c \times \mathbf{e}_1$.

$$\begin{aligned} \mathbf{e}_z \times \mathbf{e}_c &= \begin{vmatrix} \mathbf{e}_x & \mathbf{e}_y & \mathbf{e}_z \\ 0 & 0 & 1 \\ \sin \theta \cos \varphi & \sin \theta \sin \varphi & \cos \theta \end{vmatrix} \\ &= -\sin \theta \sin \varphi \mathbf{e}_x + \sin \theta \cos \varphi \mathbf{e}_y. \end{aligned} \quad (\text{A.44})$$

Thus

$$\mathbf{e}_1 = -\sin \varphi \mathbf{e}_x + \cos \varphi \mathbf{e}_y \quad (\text{A.45})$$

and

$$\begin{aligned} \mathbf{e}_2 &= \begin{vmatrix} \mathbf{e}_x & \mathbf{e}_y & \mathbf{e}_z \\ \sin \theta \cos \varphi & \sin \theta \sin \varphi & \cos \theta \\ -\sin \varphi & \cos \varphi & 0 \end{vmatrix} \\ &= -\cos \theta \cos \varphi \mathbf{e}_x + \cos \theta \sin \varphi \mathbf{e}_y + \sin \theta \mathbf{e}_z \end{aligned} \quad (\text{A.46})$$

Therefore

$$\frac{d_{ab,x}}{|\mathbf{d}_{ab}|} = \frac{1}{\sqrt{2}} (-\sin \varphi \mp i \cos \theta \cos \varphi) \quad (\text{A.47a})$$

$$\frac{d_{ab,y}}{|\mathbf{d}_{ab}|} = \frac{1}{\sqrt{2}} (\cos \varphi \pm i \cos \theta \sin \varphi) \quad (\text{A.47b})$$

$$\frac{d_{ab,z}}{|\mathbf{d}_{ab}|} = \pm \frac{i}{\sqrt{2}} \sin \theta. \quad (\text{A.47c})$$

and

$$\frac{|d_{ab,x}|^2}{|\mathbf{d}_{ab}|^2} = \frac{1}{2} (\sin^2 \varphi + \cos^2 \theta \cos^2 \varphi) \quad (\text{A.48a})$$

$$\frac{|d_{ab,y}|^2}{|\mathbf{d}_{ab}|^2} = \frac{1}{2} (\cos^2 \varphi + \cos^2 \theta \sin^2 \varphi) \quad (\text{A.48b})$$

$$\frac{|d_{ab,z}|^2}{|\mathbf{d}_{ab}|^2} = \frac{1}{2} \sin^2 \theta. \quad (\text{A.48c})$$

If Eq. (A.31) applies, we thus find that

$$F_P^\sigma = \frac{1}{2} [(1 + \cos^2 \theta) F_{\parallel} + \sin^2 \theta F_{\perp}] \quad (\text{A.49})$$

A.3 TEM images of CdSe/CdS QD samples

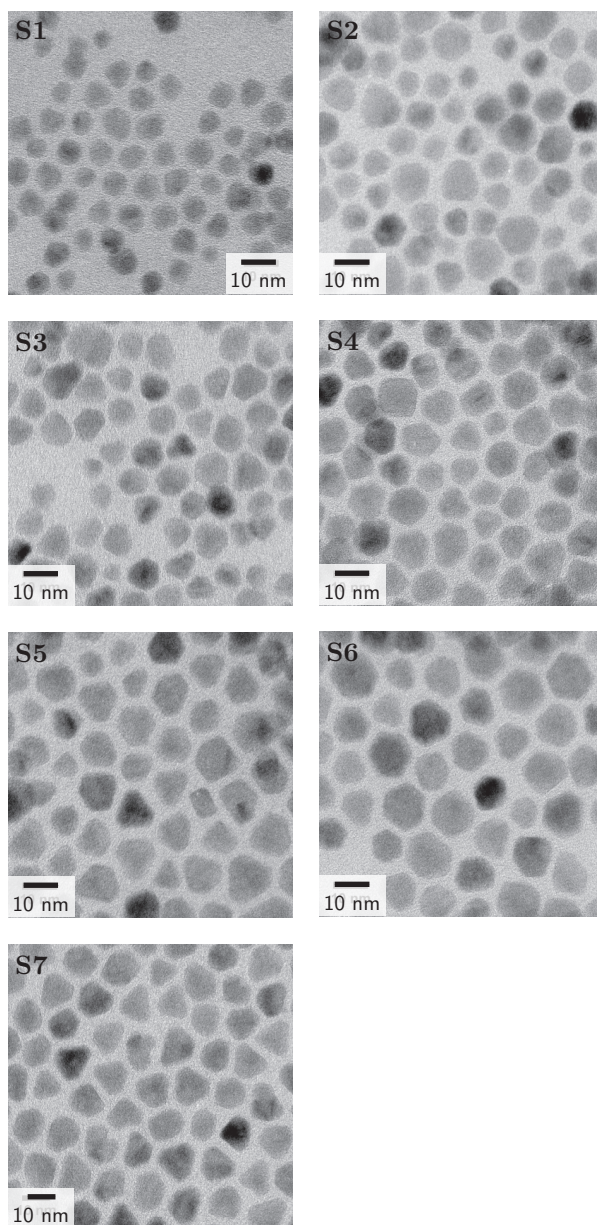


Figure A.1: Transmission electron microscope images of CdSe/CdS core/shell QD samples S1-S7 of Chapter 4.

References

- [1] L. Novotny and B. Hecht, *Principles of Nano-Optics*. Cambridge University Press, 2006.

